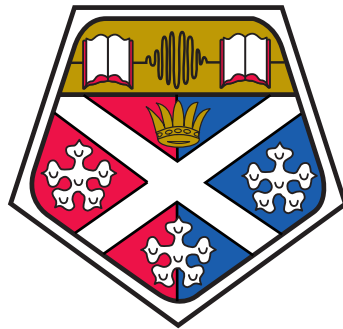


Phase-Sensitive Optical Spectroscopy of a Laser-Cooled, Microwave Atomic Clock



Rachel Elvin

Experimental Quantum Optics and Photonics Group

Department of Physics and SUPA

University of Strathclyde

A thesis presented in the fulfilment of the requirements for the
degree of


Doctor of Philosophy

December 2019

Declaration

This thesis is the result of the author's original research. It has been composed by the author and has not been previously submitted for examination which has led to the award of a degree.

The copyright of this thesis belongs to the author under the terms of the United Kingdom Copyright Acts as qualified by University of Strathclyde Regulation 3.50. Due acknowledgement must always be made of the use of any material contained in, or derived from, this thesis.

Signed: 

Date: 28/05/2019

Phase-Sensitive Optical Spectroscopy of a Laser-Cooled, Microwave Atomic Clock

Rachel Elvin

Abstract

This thesis reports on the experimental characterisation of an optically interrogated microwave frequency reference based on a compact source of cold atoms. The work addresses a method of reducing the complexity of cold-atom systems, plus the phase-sensitive optical interrogation of a microwave transition in rubidium.

Laser-cooling has provided the means for many significant developments in precision metrology, but the optical apparatus required is often large and bulky. The grating magneto-optical trap is a promising candidate for the realisation of a field-grade platform, from which we could build a portable atomic clock. The grating-MOT provided 10^7 rubidium atoms, cooled to sub-Doppler temperatures, as a test-bed for the characterisation of a microwave clock. The microwave interrogation of the ground state frequency splitting was applied optically using Ramsey-like interferometry and coherent population trapping technique in the $\text{Lin}\perp\text{Lin}$ polarisation scheme. The theory and experimental techniques that were applied in the development of this system are described, and the short-term stability of the unlocked CPT apparatus is presented.

Acknowledgements

In finishing this thesis, I can now comfortably look back over the past four years and thank those that have supported me in completing my PhD. First of all, I would like to express enormous gratitude and thanks to my supervisors Paul Griffin and Erling Riis, who have been inspirational mentors throughout. Griff, thank you especially for your unwavering patience and kindness.

In addition, I'd like to thank the rest of our Clock Team over the years. To Aidan Arnold, thank you for your terrible puns as well as your help in 3.04b during the laser uprising of 2017. To James, your ability to listen to John Mayer for hours on end deserves recognition, so here it is. Greg, your hard-working and friendly attitude made the experiment what it is today. To Michael and Ben, it was a joy to work with you both.

As for the rest of the group at EQOP, I have never met a more supportive and friendly bunch of people - I was very lucky to be a part of it. I especially want to express thanks to the 'best office ever!', past and present members, for making me laugh every day and the friendly environment you created.

Outside of work, I have to extend my gratitude to our small group of friends. Without you guys, I would never have made it to the end of this PhD. Thank you to

Abi, James and Kris. Here's to the hilarious DnD campaigns, drunken movie nights and, most importantly, to finding your tribe!

I am also fortunate to have close family, who are responsible for the person I have become and have always encouraged me to pursue the next step. To dad, never stop cracking jokes and making delicious food. My mum, thank you for inspiring me to be a scientist in the first place. To my sister Louise, thank you for always being nearby for the times that were important to me - despite not even living on this island.

Finally, to Neil. Thank you for writing your number across my whole forearm in Strathclyde's library, for your patience and support when I didn't even realise I needed it and above all, your love. Whatever life throws our way, we'll take it on together and I can't wait to see what our future holds.

Contents

Declaration	i
Abstract	ii
Acknowledgements	iv
Contents	viii
List of Figures	xi
1 Introduction	1
1.1 Time-scales	1
1.2 Atomic Time-Keeping	2
1.2.1 Primary Standards	4
1.2.2 The Future of Atomic Clocks	4
1.3 Compact Atomic Clocks	5
1.3.1 Vapour-cell Devices	6
1.3.2 Miniaturising Cold-atom Clocks	6
1.4 Thesis Layout	7

1.5	Research Outputs	8
1.5.1	Papers and Conference Proceedings	8
1.5.2	Presentations	9
1.5.3	Posters	9
2	Utilising Dark States for Atomic Clocks	11
2.1	Introduction	11
2.2	Coherent Population Trapping	12
2.2.1	Λ - Configuration	13
2.2.2	Time Evolution	16
2.3	Rubidium	20
2.4	CPT Configurations	23
2.4.1	$\sigma - \sigma$ CPT	24
2.4.2	High-Contrast CPT	25
2.5	Ramsey-CPT	35
2.5.1	Ramsey Fringes	35
2.5.2	Ramsey in CPT Clocks	38
2.6	Chapter 2 Summary	39
3	Laser Cooling with Diffractive Optics	40
3.1	Introduction	40
3.2	Basic Principles	42
3.2.1	Doppler Cooling	43
3.2.2	Sub-Doppler Cooling	44
3.2.3	Magneto-Optical Trapping	47

3.3	Building a GMOT	50
3.3.1	Experimental Methods	51
3.4	Generation II Apparatus	60
3.4.1	Portable Optics Breadboards	61
3.4.2	Experimental Control	64
3.4.3	Performance	66
3.4.4	Current Status	68
3.5	Chapter 3 Summary	69
4	A Cold-Atom Lin\perpLin CPT Clock	71
4.1	Introduction	71
4.2	Experimental Methods	72
4.2.1	D ₁ Spectroscopy	72
4.2.2	CPT Optics Bench	74
4.2.3	RF Electronics	79
4.2.4	Clock Sequence	81
4.2.5	Detection of CPT Transmission	82
4.3	Results	84
4.3.1	CPT Absorption Imaging	85
4.3.2	Single-Pulse CPT	89
4.3.3	Ramsey-CPT	93
4.4	Chapter 4 Summary	103
5	Frequency Stability	104
5.1	Introduction to Allan Deviation	105

5.2	Measuring Frequency Stability	107
5.2.1	Magnetic Field Stability	111
5.3	Chapter 5 Summary	116
6	Conclusions	117
6.1	Summary	117
6.1.1	Grating-chips for Laser-Cooling	117
6.1.2	Characterising the Clock	119
6.2	Future Work	120
	Bibliography	133

List of Figures

1.1	Accuracy and stability.	3
2.1	Three-level Λ System	14
2.2	Steady state populations for a three-level system.	20
2.3	D ₁ and D ₂ lines for ⁸⁷ Rb.	21
2.4	CPT Transitions driven with circularly polarised light.	24
2.5	High-contrast CPT Transitions for ⁸⁷ Rb	26
2.6	Clebsch-Gordon coefficients for $F' = 1$	28
2.7	Double- Λ System for Lin \perp Lin CPT	30
2.8	Clebsch-Gordon coefficients for $F' = 2$	33
2.9	Ramsey Interferometry	37
3.1	Laser Cooling Timeline	41
3.2	Sisyphus Cooling with Lin \perp Lin	45
3.3	anti-Helmholtz coils	48
3.4	1D MOT schematic	49
3.5	Mirror MOT, GMOT and Micro-fabricated GMOT	51

3.6	GMOT Schematic	52
3.7	ECDL	53
3.8	D ₂ Spectroscopy	54
3.9	Clock I Trapping and Cooling Optics Bench	56
3.10	gMOT ToF Images	58
3.11	Clock I Molasses Temperature	59
3.12	Clock II Optics Breadboards	61
3.13	Clock II gMOT Apparatus	63
3.14	Clock II Imaging Sequence	65
3.15	Fluorescence Image of the Diffracted orders	66
3.16	Clock II Atom Number	68
4.1	D ₁ Saturated Absorption Spectroscopy	73
4.2	Clock I CPT Optics Bench	75
4.3	D ₁ CPT Transitions for ⁸⁷ Rb	77
4.4	Clock I Frequency Map	79
4.5	Clock I Experiment Control Sequence	82
4.6	Detection path	83
4.7	Absorption Imaging Set-up	86
4.8	Absorption imaging with the CPT beam	87
4.9	CPT and Ramsey fringes observed using absorption imaging	88
4.10	Single-pulse CPT	90
4.11	CPT Resonance Magnetic Field Dependence	92
4.12	Ramsey-CPT Fringes for T = 10 ms	94

4.13	Optimising Ramsey fringe ROIs	95
4.14	Double-ratio Ramsey-CPT Fringes	98
4.15	Fringes with Varying Magnetic Field for $F' = 1,2$	100
4.16	Fringe Amplitude vs. Ambient Magnetic Field	102
5.1	Frequency Noise Behaviour with Averaging Time	107
5.2	Model for Ramsey Fringe	108
5.3	Allan Deviation of Cold-Atom CPT Apparatus	110
5.4	Allan deviation of CPT Resonances	113
5.5	Allan deviation with different bias fields	115

Chapter 1

Introduction

1.1 Time-scales

In the modern world, one of the most important underlying aspects of peoples' lives is time-keeping. Setting the world to a common time-scale is not a small task, but in the hundreds of years since humans have been keeping time the technology has been significantly refined. Today, a vast network of atomic clocks across the planet work together to synchronise and produce highly accurate (and stable) 'ticks' that allows international communications, travel and trade to be taken for granted. In addition, the motivation for highly accurate time-scales includes global positioning (GPS) and navigational satellite systems (GNSS) where one can realise geo-locations with an uncertainty of a few centimetres [1]. Thus applications such as prospecting, surveying and mountain rescue also benefit from accurate timing.

Historically, there have been many ways in which we have defined our time and thus there are also many different ways to build a clock. Early clocks involved

monitoring a continuous process, such as the motion of a shadow with respect to the sun or a flowing liquid. Most modern clocks are now based on the concept of a controlled driven oscillation that is measured using a counter. This could be the induced vibrations of a quartz crystal, or a swinging pendulum. However, these man-made mechanical clocks have limitations as to how well the devices will produce the same frequency over time, known as the frequency stability. For example, a device based on a quartz crystal is subject to variations in the intrinsic properties of the crystal, and the long-term stability is ultimately limited by environmental effects such as temperature. Atoms, or more specifically the quantised transitions within atoms, are ideal resonators because every atom of the same isotope is identical regardless of its location [2].

1.2 Atomic Time-Keeping

When discussing timing and frequency, it is important distinguish some of the terminology that is often used to describe the performance of an atomic clock or frequency reference. A device comprised of a frequency reference (often called a local oscillator) that is locked to an atomic transition together with a device to count the cycles of the oscillation of the stabilised output, can be classified as an atomic clock. The term ‘accuracy’ is commonly used to define the degree of conformity between a measured or calculated parameter and its true value. For an atomic clock, this would be how well the measured frequency matches the unperturbed frequency of a clock transition. Stability is defined as how well the local oscillator can keep to a certain frequency over a set amount of time. Therefore, an oscillator can be accurate

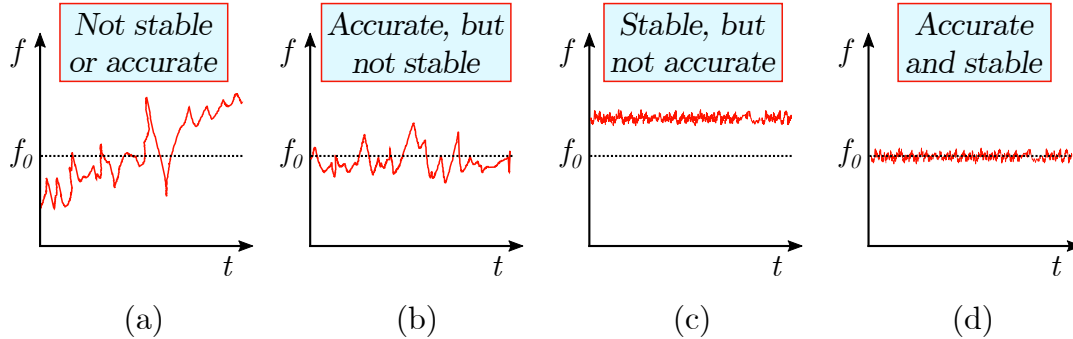


Figure 1.1: An example of the frequency-time behaviour of noise that is: (a) not stable nor accurate, (b) accurate but not stable, (c) stable but not accurate, and (d) accurate and stable.

but not stable and vice-versa, as is demonstrated in Fig. 1.1 [2].

On paper, the requirement for building an atomic frequency standard is relatively simple. A perturbation derived from the local oscillator is applied to the atoms that shows a characteristic oscillation at the atomic resonance frequency. This produces an atomic absorption signal from which we can extract an error signal. The error signal then provides frequency corrections to the local oscillator; thus it is stabilised to the atoms [2]. In an ideal case, the act of probing the atoms does not in itself affect the measured transition frequency; i.e., the influence of the applied radiation is minimal.

The first working device consisted of a quartz crystal oscillator that was stabilised to a transition in an ammonia, and was built at the National Bureau of Standards (NBS, now the National Institute of Standards and Technology) [3, 4]. Work continued on the ammonia clocks until the development of the atomic beam technique that would provide better accuracy. A clock based on a microwave transition in ^{133}Cs that incorporated Rabi's magnetic resonance technique was built in

1952 at NBS. The method of probing was later refined to Ramsey's technique of split interrogating fields [5], overcoming some of the uncertainties induced from the interaction by reducing the probe to two separated microwave pulses. Similarly, at the National Physical Laboratory (NPL) in the United Kingdom, a device that measured the caesium and adopted Ramsey's technique was built in 1955 [6, 7].

1.2.1 Primary Standards

In 1967, it was ultimately agreed that the second would be re-defined to correspond to the duration of 9,192,631,770 periods of radiation within the ground state of the ^{133}Cs atom. The technology involved in building atomic clocks has seen dramatic developments over the past few decades. One of the most significant was the advent of laser-cooling in the 1980s [8] and the subsequent development of atomic fountains [9, 10] that would inspire the new era of precise metrology. The caesium fountain clocks, using ultra-cold atoms, replaced the thermal atomic beam clocks as the primary standard. The fountains are still used as the main frequency standard to this day, with national metrology laboratories across the world utilising a caesium atomic fountain as their primary reference. The development of the fountains has led to the ability to control systematic effects with an uncertainty of a few parts in 10^{-16} [11].

1.2.2 The Future of Atomic Clocks

Of course, the urge to reach better accuracy and stability is still ardently pursued by many researchers. The synchronised global time-scale is managed by the Bureau

of Weights and Measures (BIPM) and relies on national metrology centres, such as NPL (UK) or the National Institute for Standards and Technology (NIST, USA), providing signals from their laboratories that can contribute to International Atomic Time (TAI). Additionally, corrections from variations in the rotation of the Earth are applied (in ‘leap seconds’) and the time-scale is re-distributed as Universal Coordinated Time (UTC) [12].

The pursuit of a new primary standard has been underway for a while, which has led to the establishment of a list of secondary standards, including ^{87}Rb fountains and eight different types of optical frequency standards. The ^{87}Rb frequency standard at SYRTE in France regularly contributes to TAI, and it has been observed that a better time-scale could be realised from optical frequency standards [13–15]. With that in mind, the criteria for ultimately deciding on a new definition are extensive [11, 16], and it is possible that such a decision will be made within the next ten years.

1.3 Compact Atomic Clocks

In parallel with the development of frequency standards with high accuracy and excellent stability, there has also been much consideration towards compact and field-grade devices. A growing number of applications, such as GPS satellites, are accommodating devices that have limited volume and low power consumption, but also do not require the same level of performance. Reducing the volume and footprint of atomic clocks has been an ongoing goal for many years.

1.3.1 Vapour-cell Devices

Microwave atomic clocks based on vapour cell and buffer gas technology have seen many successful advancements in terms of realising a compact device. A significant achievement in this endeavour was the development of the chip-scale atomic clock (CSAC) in the early 2000s [17]. These devices adopted optical interrogation of the microwave transition in rubidium atoms, and were fully integrated into package volumes of $< 20 \text{ cm}^3$. Now made commercially by Microsemi, the CSACs operate with a short-term stability ($< 100 \text{ s}$) on the order of $10^{-10}/\sqrt{\tau}$ [18, 19].

Additionally, laboratory-based frequency standards that utilise high-contrast coherent population trapping (CPT) have achieved short-term stabilities of $\approx 10^{-13}/\sqrt{\tau}$ [20–22], with reasonably compact physics packages and microfabricated vapour cells.

1.3.2 Miniaturising Cold-atom Clocks

Devices based on laser-cooled atoms have shown great promise in terms of low long-term frequency drift. While the apparatus required to perform laser-cooling is often complicated and bulky, there has been much progress in reducing the number of optics and overall size of the apparatus. This progress offers great promise for widespread future adaptation of cold-atom devices. Notably, there are now commercially built atomic clocks based on laser-cooled atoms. These systems, adopting microwave interrogation of the cold atoms, have seen short-term stabilities on the order of $\approx 10^{-13}/\sqrt{\tau}$. [23–28].

In contrast to their vapour-cell based counter-parts, atomic frequency references based on high-contrast CPT and cold atoms have seen less development. Despite

the better short-term stability displayed by thermal CPT clocks, devices based on cold rubidium atoms have already shown improvements to the long-term frequency stability [29] and provided a clean system for testing the optically induced frequency shifts [30].

It is therefore within reason to envisage a compact physics package that combines cold atoms with the CPT technique. The purpose of the research that supports this thesis was to study and develop a compact source of cold atoms into a portable frequency reference with the benefits of cold atoms. The work was based on two concepts: the grating magneto-optical trap and coherent population trapping (CPT). The former provided a sample of laser-cooled rubidium atoms whilst the latter was a relatively simple method of probing the clock transition frequency in the rubidium atoms. The common factor was that both concepts have a lot of potential for miniaturisation.

1.4 Thesis Layout

The main body of this thesis is comprised of five chapters:

- Chapter 2 describes relevant atom-interaction theory for three level systems in order to introduce the coherent population trapping technique. The level structure of rubidium is presented, leading to the more complex CPT techniques and Raman-Ramsey interferometry.
- Chapter 3 provides a basic foundation for laser cooling and grating magneto-optical traps (GMOTs). The cooling apparatus for the main CPT clock ex-

periment is described, and a second generation portable GMOT experiment is presented.

- In Chapter 4, the CPT part of the main clock experiment is presented. This includes a description of the clock apparatus and detection techniques and goes on to discuss detected characteristic CPT and Raman-Ramsey spectra.
- Chapter 5 then discusses frequency stability of oscillators and presents an investigation of the first generation CPT clock frequency stability.
- The conclusions and intended future work for the experiment are presented in Chapter 6.

1.5 Research Outputs

1.5.1 Papers and Conference Proceedings

- **R. Elvin**, G. W. Hoth, M. Wright, B. Lewis, J. P. McGilligan, A. S. Arnold, P. F. Griffin and E. Riis, “A Cold-Atom Clock Based on a Diffractive Optic,” *Opt. Exp.* **27**, 38359-38366 (2019)
- G. W. Hoth, **R. Elvin**, M. Wright, B. Lewis, J. P. McGilligan, A. S. Arnold, P. F. Griffin and E. Riis, “Impact of Laser Frequency Noise in Coherent Population Trapping with Cold Atoms,” *IEEE Proceedings, ICFS-EFTF* (2019)
- G. W. Hoth, **R. Elvin**, M. Wright, B. Lewis, A. S. Arnold, P. F. Griffin and E. Riis, “Towards a Compact Atomic Clock Based on Coherent Population Trap-

ping and the Grating Magneto-Optical Trap,” *SPIE Proc.* **10934**, 109342E (2019).

- **R. Elvin**, G. W. Hoth, M. W. Wright, J. P. McGilligan, Arnold, A. S. Arnold, P. F. Griffin and E. Riis, “Raman-Ramsey CPT with a Grating Magneto-Optical Trap,” *IEEE Proc. EFTF* (2018).
- J. P. McGilligan, P. F. Griffin, **R. Elvin**, S. J. Ingleby, E. Riis, and A. S. Arnold, “Grating Chips for Quantum Technologies.” *Sci. Rep.* **7**, 384 (2017)

1.5.2 Presentations

- Talk Title: “Towards a Cold-Atom Grating Microwave Atomic Clock”
 - Annual Meeting of the APS Division of Atomic, Molecular and Optical Physics (DAMOP), *Milwaukee, WI* (May 2019).
- Talk Title: “Grating Chips for Raman-Ramsey CPT”
 - European Time and Frequency Seminar (EFTF), *Torino, Italy* (April 2018).

1.5.3 Posters

- Poster Title: “Grating Chip based Raman-Ramsey CPT for Compact Atomic Clocks”
 - IOP Topical Research Meeting on Time, *London, UK* (March 2019).

-
- NPL Post-Graduate Institute Annual Conference, *Glasgow, UK* (October 2018).
 - Young Atom Opticians Conference (YAO), *Glasgow, UK* (June 2018).
 - Poster Title: “Towards a Compact Cold-Atom Clock Based on a Grating Magneto-Optical Trap”
 - Engage at Strathclyde, *Glasgow, UK* (May 2018).
 - Poster Title: “Observations of Dark State Interference in Crossed-Polarisation CPT with Cold Atoms”
 - European Time and Frequency Seminar (EFTF), *Torino, Italy* (April 2018).
 - Poster Title: “High-Contrast Coherent Population Trapping with Cold Atoms on a Grating Chip”
 - 2nd PhD Year Poster Presentation, *Glasgow, UK* (August 2017).

Chapter 2

Utilising Dark States for Atomic Clocks

2.1 Introduction

In the development of compact atomic clocks, techniques that are experimentally simple are ideal. For the microwave transitions in alkali metals, the coherent population trapping (CPT) technique falls into this category. This approach utilises a single probe beam for both addressing and detection of the atomic resonance frequency at the same point in space. The probe beam replaces the microwave cavity commonly used for interrogating the clock transitions in neutral alkali atoms, allowing one to realise frequency reference where the size of the apparatus is not constrained by the size of the microwave cavity itself. However, an understanding of how the atomic population behaves after a CPT interaction is essential for optimising such a system.

This chapter aims to describe the theory of atom-light interaction for a three-

level system in order to introduce CPT and the generation of dark states. For the work described in this thesis, the experiment was based on an isotope of the alkali metal rubidium. Therefore, the fine, hyperfine and sub-hyperfine (Zeeman) level structure of the isotope ^{87}Rb is described in Sec. 2.3.

This leads onto a more technical discussion of high-contrast CPT schemes, covered in Sec. 2.4, that can be applied to improve the percentage of atoms driven into the dark state and subsequently the detected ‘clock’ signal. We conclude this chapter in Section 2.5 by giving a brief introduction to Ramsey interferometry and finish by discussing an adaptation for Ramsey-CPT interrogation.

2.2 Coherent Population Trapping

Coherent population trapping (CPT) is a phenomena that occurs in a three-level system where atoms are trapped in superposition states that arise from phase-coherent coupling with two fields [31]. Interference in the interaction pathways prevents the atoms in the superposition from further interaction with the light, and we therefore refer to the superposition as a dark state. The phenomenon was first observed in 1976 as dark spots in the detected fluorescence of a sodium beam [32], and was later deduced to be an optical pumping effect into a non-absorbing superposition between ground states [33]. The technique was responsible for the development of the chip-scale atomic clock (CSAC) in the early 2000s, and the devices are now widely commercially available [17–19, 34, 35].

In this section, we give a basic introduction to the phenomena using the Schrödinger picture before extending this into the density matrix formalism, and finally using

the optical Bloch equations to describe the dynamics of CPT.

2.2.1 Λ - Configuration

The three-level configuration for CPT takes the form of a lambda (Λ) shape depicted in Fig. 2.1. This is due to the shape the transitions make, and is different from other three-level schemes such as the ladder or V-shape. In the CPT technique, coherence is induced between two long lived ground states via two-photon excitation with a common excited level [31]. The description of the Λ -configuration begins with the Hamiltonian for a bare atom:

$$\hat{H}_0 = \sum_i \hbar\omega_i |i\rangle \langle i|. \quad (2.1)$$

We can then state that the total Hamiltonian is $\hat{\mathcal{H}}(t) = \hat{H}_0 + \hat{H}_1(t)$, where $\hat{H}_1(t)$ is the atom-light interaction. As shown in Fig. 2.1, the two optical fields, $\vec{E}_a(t)$ and $\vec{E}_b(t)$, connect two ground states, $|1\rangle$ and $|2\rangle$, via one excited level, $|3\rangle$.

Here, we assume field $\vec{E}_a(t)$ only interacts with levels $|1\rangle \rightarrow |3\rangle$ and field $\vec{E}_b(t)$ only interacts with levels $|2\rangle \rightarrow |3\rangle$. The Λ -scheme is driven using this coherent bi-chromatic field with a relative detuning between the components that equals the frequency difference between $|1\rangle$ and $|2\rangle$. In real atoms, this could be the hyperfine ground state splitting f_{HFS} . The components of the field are described by:

$$\vec{E}_a(t) = E_a \cos(\omega_a t - \phi_a), \quad (2.2a)$$

$$\vec{E}_b(t) = E_b \cos(\omega_b t - \phi_b). \quad (2.2b)$$

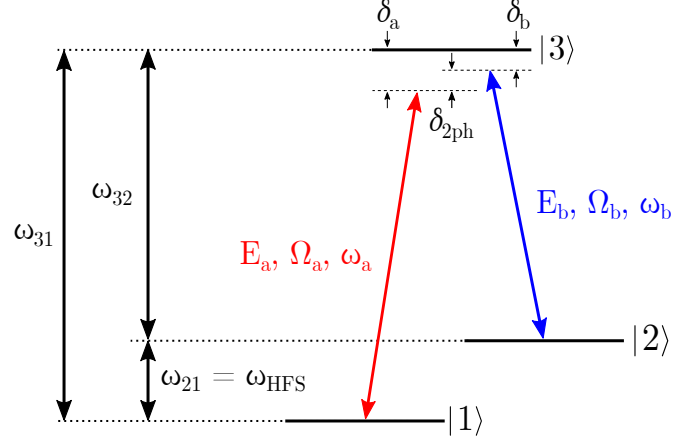


Figure 2.1: A simplified three-level Λ system. Two levels, $|1\rangle$ and $|2\rangle$ are connected with coherent fields $\vec{E}_a(t)$ and $\vec{E}_b(t)$ via the excited state $|3\rangle$.

The fields have a relative phase, $\Delta\phi = \phi_a - \phi_b$, and are detuned from optical resonances (see Fig. 2.1) by:

$$\delta_a = \omega_a - \omega_{31}, \quad (2.3a)$$

$$\delta_b = \omega_b - \omega_{32}, \quad (2.3b)$$

$$\delta_{2ph} = \delta_a - \delta_b, \quad (2.3c)$$

where δ_{2ph} is the two-photon, or Raman, detuning. The atom-light interaction with this three-level Λ -system can be described using the interaction Hamiltonian:

$$\hat{H}_I = \frac{\hbar\Omega_a}{2} e^{-i(\omega_a t + \phi_a)} |3\rangle \langle 1| + \frac{\hbar\Omega_b}{2} e^{-i(\omega_b t + \phi_b)} |3\rangle \langle 2| + H.c. \quad (2.4)$$

$H.c.$ stands for Hermitian conjugate and $\Omega_{a,b}$ are the Rabi frequencies given by $\Omega_{a,b} = -\langle i|e\hat{r}|j\rangle E_{a,b}/2$. To determine the effects of the interaction, the matrix

elements of the electric dipole operator are calculated. Three possible eigenstates arise from this: the excited state and two linear superpositions. The latter are linear combinations of the ground states given by [36–39]:

$$|C\rangle = \frac{1}{\Omega_\Lambda} e^{i\omega_1 t} (\Omega_a |1\rangle + e^{i\omega_{21}} \Omega_b |2\rangle), \quad (2.5a)$$

$$|NC\rangle = \frac{1}{\Omega_\Lambda} e^{i\omega_1 t} (\Omega_b |1\rangle - e^{i\omega_{21}} \Omega_a |2\rangle), \quad (2.5b)$$

where:

$$\Omega_\Lambda = \frac{1}{\sqrt{(\Omega_a)^2 + (\Omega_b)^2}}. \quad (2.6)$$

The superpositions $|C\rangle$ and $|NC\rangle$ are known as coupled and non-coupled states, respectively. Using the interaction operator in Eqn. 2.4 and applying the rotating wave approximation, the matrix elements for the transitions to the excited state ($|3\rangle$) can be calculated:

$$\langle 3 | \hat{H}_I | C \rangle = \frac{\hbar}{2\Omega_\Lambda} e^{-i(\delta_a t + \phi_a)} (\Omega_a^2 + \Omega_b^2 e^{i\delta_{2ph} t - i\Delta\phi}), \quad (2.7a)$$

$$\langle 3 | \hat{H}_I | NC \rangle = \frac{\hbar\Omega_a\Omega_b}{2\Omega_\Lambda} e^{-i(\delta_a t + \phi_a)} (1 - e^{i\delta_{2ph} t - i\Delta\phi}). \quad (2.7b)$$

From this we can infer that when the two optical fields are in phase, $\Delta\phi = 0$, and the frequency difference is equal to the frequency between $|1\rangle$ and $|2\rangle$ ($\delta_{2ph} = 0$) then the transition amplitude for the non-coupled state, $|NC\rangle$, is zero:

$$\langle 3 | \hat{H}_I | NC \rangle = 0 \quad (2.8)$$

Therefore, as the δ_{2ph} approaches zero atoms are optically pumped into a coherent dark state, $|NC\rangle$, that is de-coupled from the interacting field and hence the atoms are then trapped in this state. This can be observed in the detected transmission of the driving laser as a maximum in transmission, assuming all atoms which see the beam are successfully pumped into the dark state. If δ_{2ph} is non-zero, atoms will absorb photons again and the transmission of the optical field decreases. This forms the dark resonance feature observed in CPT spectroscopy; a Lorentzian with a linewidth directly related to the dark state lifetime.

In a later section (Chapter 4, Section 4.3.2), experimentally obtained CPT spectrum from the first generation cold-atom CPT apparatus at Strathclyde is presented.

2.2.2 Time Evolution

CPT is an optical pumping effect, and therefore the time evolution of the system and spontaneous emission must also be considered. The interaction of each transition in the Λ scheme with an electromagnetic field can be derived using the time-dependent Schrödinger equation (TDSE):

$$i\hbar \frac{d|\psi\rangle}{dt} = \mathcal{H}(t) |\psi\rangle. \quad (2.9)$$

The time-dependent perturbation of this three-level interaction can be described by calculating the optical Bloch equations. For this, we use the Linblad variation of

the Master equation in order to include relaxation:

$$\frac{d\rho}{dt} = -\frac{i}{\hbar} [\rho, \mathcal{H}] - \mathcal{L}(\rho). \quad (2.10)$$

Here, ρ is the density matrix of the system and the three-level Linblad operator is given by $\mathcal{L}(\rho)$. The density matrix allows us to statistically study a multiple level system or a mixture of pure states derived from:

$$\hat{\rho} = \sum_{i,j} c_i c_j^* |i\rangle \langle j|, \quad (2.11)$$

where indices i and j refer to the states, and $c_{i,j}$ are state amplitudes. The total Hamiltonian for the system includes the bare atom operator and the interaction operator for the three-level system in Eqn. 2.4. This is reconstructed as a matrix to give:

$$\mathcal{H}(t) = \begin{pmatrix} \hbar\omega_1 & 0 & \hbar\Omega_a/2e^{i\omega_a t} \\ 0 & \hbar\omega_2 & \hbar\Omega_b/2e^{i\omega_b t} \\ \hbar\Omega_a/2e^{-i\omega_a t} & \hbar\Omega_b/2e^{-i\omega_b t} & \hbar\omega_3 \end{pmatrix}, \quad (2.12)$$

where the phase terms from Sec. 2.2.1 have been neglected for simplicity. To derive the time evolution of the system, we apply the Linblad equation from Eq. 2.10 and

use the density matrix for a three-level system:

$$\rho = \begin{pmatrix} \rho_{11} & \rho_{12} & \rho_{13} \\ \rho_{21} & \rho_{22} & \rho_{23} \\ \rho_{31} & \rho_{32} & \rho_{33} \end{pmatrix}. \quad (2.13)$$

By inserting Eqn. 2.12 and 2.13 into Eqn. 2.10 we can define the populations (diagonals) of the three-level system:

$$\dot{\rho}_{11} = \frac{i\Omega_a}{2} (\rho_{13}e^{-i\omega_a t} - \rho_{31}e^{i\omega_a t}) - \rho_{11}\Gamma_1 + \frac{\Gamma_3}{2}\rho_{33}, \quad (2.14a)$$

$$\dot{\rho}_{22} = \frac{i\Omega_b}{2} (\rho_{23}e^{-i\omega_b t} - \rho_{32}e^{i\omega_b t}) - \rho_{22}\Gamma_2 + \frac{\Gamma_3}{2}\rho_{33}, \quad (2.14b)$$

$$\dot{\rho}_{33} = \frac{i\Omega_a}{2} (\rho_{31}e^{i\omega_a t} - \rho_{13}e^{-i\omega_a t}) + \frac{i\Omega_b}{2} (\rho_{32}e^{i\omega_b t} - \rho_{23}e^{-i\omega_b t}) - \Gamma_3\rho_{33}, \quad (2.14c)$$

and the off-diagonal (coherences) as:

$$\dot{\rho}_{12} = (i[\omega_2 - \omega_1] - \gamma_{12})\rho_{12} + \frac{i}{2} (\Omega_b e^{-i\omega_b t} \rho_{13} - \Omega_a e^{-i\omega_a t} \rho_{32}), \quad (2.15a)$$

$$\dot{\rho}_{31} = (i[\omega_1 - \omega_3] - \gamma_{31})\rho_{31} + \frac{i}{2} (\Omega_a e^{-i\omega_a t} [\rho_{33} - \rho_{11}] - \Omega_b e^{-i\omega_b t} \rho_{21}), \quad (2.15b)$$

$$\dot{\rho}_{32} = (i[\omega_2 - \omega_3] - \gamma_{32})\rho_{32} + \frac{i}{2} (\Omega_b e^{-i\omega_b t} [\rho_{33} - \rho_{22}] - \Omega_a e^{-i\omega_a t} \rho_{12}). \quad (2.15c)$$

We can simplify this further by transforming into a rotating frame by using the following set of definitions:

$$\rho_{12} = \tilde{\rho}_{12} e^{-i(\omega_a - \omega_b)t}, \quad (2.16a)$$

$$\rho_{31} = \tilde{\rho}_{31} e^{-i\omega_a t}, \quad (2.16b)$$

$$\rho_{32} = \tilde{\rho}_{32} e^{-i\omega_b t}. \quad (2.16c)$$

By inserting the relationships defined in Eqn. 2.3 and 2.16 into Eqns. 2.14-2.15, we can therefore re-define the populations (diagonals) for the systems as:

$$\dot{\rho}_{11} = \frac{i\Omega_a}{2} (\tilde{\rho}_{13} - \tilde{\rho}_{31}) - \Gamma_1 \rho_{11} + \frac{\Gamma_3}{2} \rho_{33}, \quad (2.17a)$$

$$\dot{\rho}_{22} = \frac{i\Omega_b}{2} (\tilde{\rho}_{23} - \tilde{\rho}_{32}) - \Gamma_2 \rho_{22} + \frac{\Gamma_3}{2} \rho_{33}, \quad (2.17b)$$

$$\dot{\rho}_{33} = \frac{i\Omega_a}{2} (\tilde{\rho}_{31} - \tilde{\rho}_{13}) + \frac{i\Omega_b}{2} (\tilde{\rho}_{32} - \tilde{\rho}_{23}) - \Gamma_3 \rho_{33}, \quad (2.17c)$$

and the coherences (off-diagonals) as:

$$\dot{\tilde{\rho}}_{12} = (i[\delta_b - \delta_a] - \gamma_{12}) \tilde{\rho}_{12} + \frac{i}{2} (\Omega_b \tilde{\rho}_{13} - \Omega_a \tilde{\rho}_{32}), \quad (2.18a)$$

$$\dot{\tilde{\rho}}_{31} = (i\delta_a - \gamma_{31}) \tilde{\rho}_{31} + \frac{i}{2} (\Omega_a [\rho_{33} - \rho_{11}] - \Omega_b \tilde{\rho}_{21}), \quad (2.18b)$$

$$\dot{\tilde{\rho}}_{32} = (i\delta_b - \gamma_{32}) \tilde{\rho}_{32} + \frac{i}{2} (\Omega_b [\rho_{33} - \rho_{22}] - \Omega_a \tilde{\rho}_{12}). \quad (2.18c)$$

The equations in 2.17 and 2.18 describe the optical Bloch equations for a three-level system in the Λ -configuration. The steady state of the system can be derived by setting the time derivative to zero, $\dot{\tilde{\rho}}_{ij} = 0$. The populations of the system are

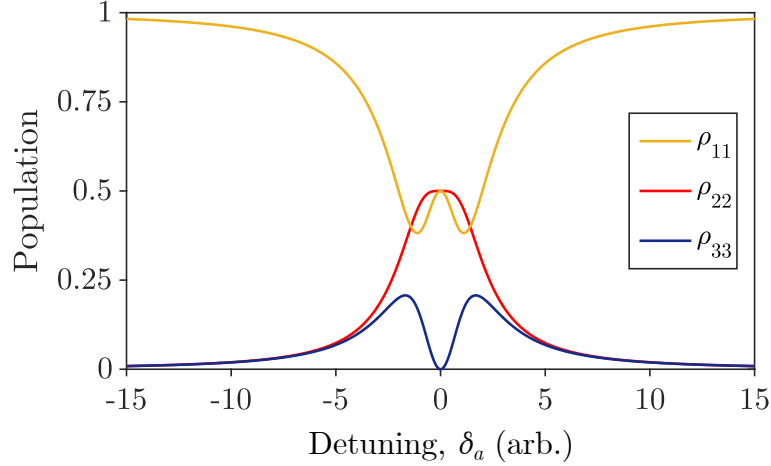


Figure 2.2: Populations of states $|1\rangle$, $|2\rangle$ and $|3\rangle$ with respect to the detuning δ_a of CPT field $E_a(t)$. The second CPT field is kept resonant with its respective transition.

plotted in Fig. 2.2 for the steady state as the detuning, δ_a , of one of the CPT fields is scanned across its resonance frequency. The other field, $E_b(t)$, is kept resonant with its atomic transition and the amplitude for the two fields is set to be equal ($\Omega_a = \Omega_b$).

The plot shows that the population of excited state (ρ_{33}) depletes to zero as the detuning also approaches $\delta_a = 0$. The population is then evenly divided between the two ground states, as is shown by the population curves for ρ_{11} and ρ_{22} .

2.3 Rubidium

When considering CPT with real atoms, the level structure is important. For the experiments discussed in this manuscript, rubidium was used as the atomic species due to the convenient frequencies of the atomic absorption and inexpensive diodes

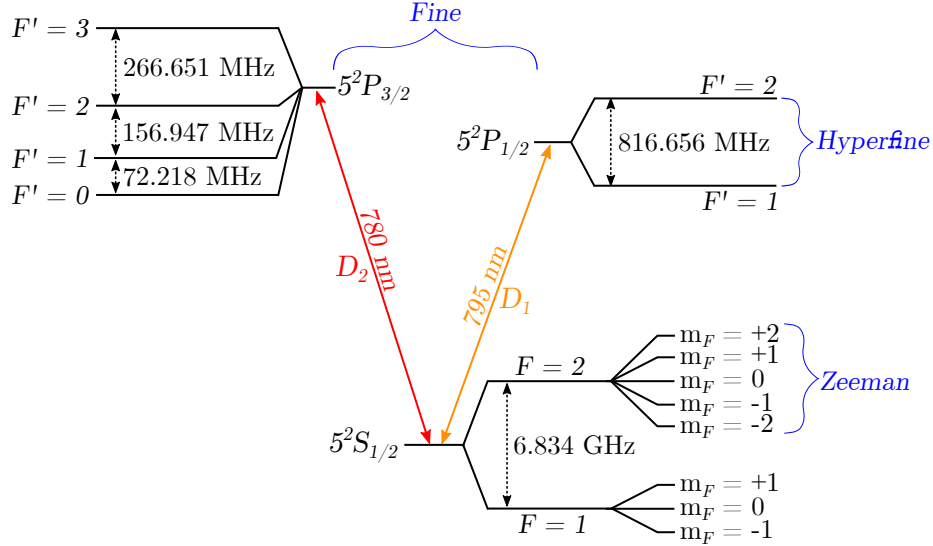


Figure 2.3: Level configuration of ^{87}Rb . Coloured arrows denote the D_1 (795 nm) and D_2 (780 nm) lines. Fine structure is denoted between the $5^2P_{1/2}$ and $5^2P_{3/2}$ manifolds. The excited $5^2P_{1/2}$, $F' = 1, 2$ are used to highlight hyperfine structure, and the $5^2S_{1/2}$ ground state shows Zeeman splitting for the $F = 1, 2$ hyperfine states.

that operate at the relevant wavelengths. Rubidium is a popular choice for laser cooling because of this, and it is also used in the majority of mass-produced frequency standards for GPS and telecommunication applications.

Rubidium is an alkali atom, and thus has a single electron in its outer shell. It occurs naturally as two isotopes; ^{85}Rb and ^{87}Rb , where the latter is less abundant than the former. In this section, we will consider the ^{87}Rb isotope. In ^{87}Rb , there are two excitation lines with different wavelengths that are drawn in Fig. 2.3. Splitting of the excited manifold is called fine structure and the two transitions are the $5^2S_{1/2} \rightarrow 5^2P_{1/2}$ and $5^2S_{1/2} \rightarrow 5^2P_{3/2}$, commonly referred to as the D_1 and D_2 lines respectively [40]. Interaction between total electronic and atomic angular momentum causes

further splitting below fine, called hyperfine, and thus the ground state and excited states split into several more levels with an energy difference between them.

The ground state is split by 6.834 GHz [40], and this frequency is used to provide the frequency reference for atomic clock applications. As is shown in Fig. 2.3, the D₁ line contains two hyperfine energy levels and the D₂ line contains four. In terms of a clock based on CPT resonances, incoherent coupling to additional states affects the resonance contrast. Therefore the D₁ is often chosen for its relative simplicity.

The final splitting that is discussed is Zeeman splitting of the hyperfine structure. The hyperfine states are split into distinct levels when placed under a magnetic field according to their orientation relative to the external field, known as Zeeman sub-levels. As is shown in Fig. 2.3 for ⁸⁷Rb, the hyperfine levels will split into $2F + 1$ states, where m_F is the projection of total angular momentum, F , onto the quantisation axis. The energy shift of the particular Zeeman sub-level with respect to an applied magnetic field, \vec{B} , is obtained from the Breit-Rabi formula [40]:

$$E(F, m_F) = -\frac{\Delta E_{\text{HFS}}}{2(2I + 1)} - g_I \mu_B m_F \vec{B} \pm \frac{\Delta E_{\text{HFS}}}{2} \left(1 + \frac{4m_F}{2I + 1} x + x^2 \right)^{1/2}, \quad (2.19)$$

where μ_B is the Bohr magneton, g_I is the Landé-g factor for the total nuclear angular momentum I , and $\Delta E_{\text{HFS}} (= A_{\text{HFS}}(I + 1/2))$ is the hyperfine splitting with magnetic dipole constant A_{HFS} . The ‘ x ’ term is given by:

$$x = \frac{(g_I + g_J) \mu_B \vec{B}}{\Delta E_{\text{HFS}}}, \quad (2.20)$$

where g_J is the Landé-g factor for the total electronic angular momentum, J .

2.4 CPT Configurations

This section will include a more technical discussion of the CPT technique for atomic clocks and introduce some of the ‘High-Contrast’ techniques. The operation of an atomic clock involves stabilising an external frequency source, often referred to as a local oscillator, to an atomic transition frequency. This means we need some kind of measurable response from the atoms, such that an error signal can be generated to stabilise the local oscillator.

The atom’s response as the two-photon detuning is scanned over zero can be extracted by measuring the transmission of the probe laser through the atoms. We essentially scan the local oscillator frequency and measure how close it is to the atomic resonance frequency using this detected feature, which has a Lorentzian profile. The transmission can also be used to measure the clock stability, and this is covered in Sec. 5.2.1. The relative signal-noise of this feature contributes to the performance of the clock, and is closely tied to how complete the dark state is. This can be quantified by measuring the contrast of the central spike in transmission to the full absorption feature (Sec. 4.3.2).

In CPT clocks, it is the coherence generated between certain Zeeman sub-levels of the hyperfine ground states that is then used to measure the frequency splitting. Careful selection of beam parameters, such as the polarisation of the CPT driving field, can exploit the sub-level structure of the Rb D_1 line to grant control over the dark state pumping and the population distribution among the sub-levels. This allows one to drive atoms into CPT states that are more favourable for atomic clock applications.

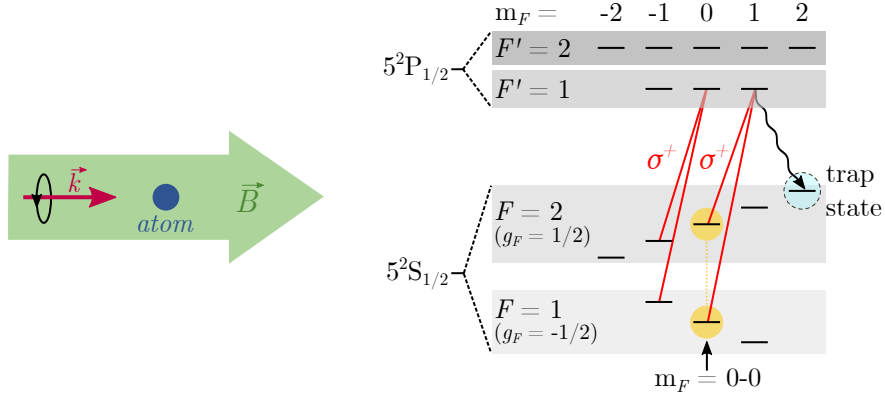


Figure 2.4: A schematic of an atom under interrogation with right-hand circularly polarised light where the quantisation axis is set by a homogeneous magnetic field, \vec{B} , propagating in the same direction as the probe beam. Here, \vec{k} is the wave vector. The level diagram for interaction with the D_1 line in ^{87}Rb shows the σ^+ transitions that lead to atomic population accumulating in the stretched Zeeman sub-level, $m_F = 2$. The CPT state that is favourable for clock applications is highlighted by the yellow joined circles

2.4.1 $\sigma - \sigma$ CPT

Traditionally, CPT transitions are driven using right or left-handed circularly polarised light, and an example of the former is shown in Fig. 2.4. The quantisation axis is set by a homogeneous magnetic field, \vec{B} , parallel to the direction of the laser beam that is addressing the atoms. This lifts the degeneracy on the hyperfine ground states and allows us to access CPT between the Zeeman sub-levels $m_F = 0-0$ using this circularly polarised light. This CPT state, highlighted by the yellow circles in Fig. 2.4, is favourable for clock applications since $m_F = 0$. This scheme is relatively simple compared to the high-contrast techniques that are covered later in this section. However, due to the circular polarisation, atoms are preferentially pumped via σ^\pm transitions into the $\pm m_F$ stretched states and population in the $m_F = 0-0$

CPT state is low. For clock applications, this degrades the performance as the transmission feature on two-photon resonance is weaker.

2.4.2 High-Contrast CPT

To overcome the poor contrast, several techniques were developed that mitigate accumulation in the stretched m_F states [41,42]. The techniques are more complex and utilise different configurations of polarisation for the individual optical CPT fields, such as Lin||Lin [43], Lin⊥Lin [44] and $\sigma^+ - \sigma^-$ [45,46]. In the Lin||Lin and Lin⊥Lin schemes, the two CPT fields are linearly polarised but the relative polarisation angle between them is zero or $\pi/2$, respectively. The CPT fields in the $\sigma^+ - \sigma^-$ scheme are counter-propagating and have orthogonal circular polarisation. In an additional scheme, the high contrast CPT resonances are realised using a pulsed interrogation called push-pull optical pumping (PPOP) [22]. The pumping scheme realised in PPOP is analogous to $\sigma^+ - \sigma^-$ and Lin⊥Lin.

The experiments described in this manuscript adopted CPT in the Lin⊥Lin scheme. For clarity, it is useful to consider the Lin||Lin technique as well. In addition, a description of the dark states that are possible on the D_1 line of ^{87}Rb is also considered. The configurations for two sets of double- Λ structures are shown in Fig. 2.5. The double- Λ systems in (a) and (b) correspond to a total of three dark states that are possible under interrogation with one of the high-contrast schemes, and that are relevant for CPT clocks using rubidium atoms. The level diagrams show the two independent structures that form a double- Λ , drawn in solid and dashed lines, and the relevant ground state sub-levels that are coupled (coloured

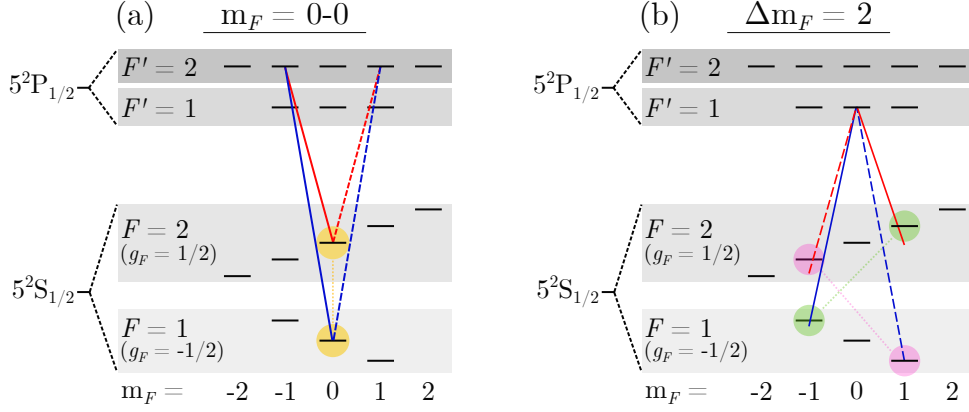


Figure 2.5: Three possible dark states which can be realised in the D_1 line of ^{87}Rb with a high-contrast CPT technique. Landé-g factors for the hyperfine ground states are given by g_F . (a): In this scheme, the $|F = 1, m_F = 0\rangle$ and $|F = 2, m_F = 0\rangle$ are connected via separate σ^\pm transitions to form a dark state between the $m_F = 0$ sub-levels. (b): Here, the $\Delta m_F = 2$, dark states are realised between the $|F = 1, m_F = \pm 1\rangle \rightarrow |F = 2, m_F = \mp 1\rangle$ via two separate Λ structures.

circles). Each dark superposition is separated by the hyperfine ground state splitting frequency, i.e. they are two-photon resonant. In Fig. 2.5 (a), two Λ structures (solid and dashed lines) connect the $|F = 1, m_F = 0\rangle$ and $|F = 2, m_F = 0\rangle$ via separate σ^\pm transitions in a dark state superposition. This double- Λ is referred to as $m_F = 0-0$ because of the ground state Zeeman levels that are connected.

The schematic in Fig. 2.5 (b) shows two independent Λ systems that couple together the $|F = 1, m_F = -1\rangle$ and $|F = 2, m_F = 1\rangle$ in one structure, which we will call Λ_+ . The second, which we will call Λ_- , drives the $|F = 1, m_F = 1\rangle$ and $|F = 2, m_F = -1\rangle$ transitions. This double- Λ is labelled the $\Delta m_F = 2$ because the Zeeman sub-levels $m_F = \pm 1$ are connected to the $m_F = \mp 1$. The CPT configurations drawn in Fig. 2.5 (a) and (b) are driven via different hyperfine excited levels, $F' = 1 \& 2$. This was chosen as each double- Λ , the $m_F = 0-0$ and $\Delta m_F = 2$, also

depend on the coupled excited level. In Chapter 4, an experiment investigating this dependence through measurements of dark state interference will be presented.

Lin||Lin

As the name suggests, in the Lin||Lin CPT technique each component of the driving CPT field has parallel linear polarisation and was first proposed in 2005 by Taichenachev *et al.* [47]. Thermal atomic clocks adopting Lin||Lin CPT were realised between 2009-2010 [48–50]. Since then, the method was successfully demonstrated with cold rubidium atoms [43] and later developed into a test bed for light shifts (AC-Stark) from the atom-light interaction [29, 30]. However, the Lin||Lin technique adopted by this research group has since been replaced by the $\sigma^+ - \sigma^-$ scheme [45, 46].

Under a weak external magnetic field, \vec{B} , linearly polarised light propagating parallel with the direction of this field is broken down into its circularly polarised components. This leaves equally driven σ^+ or σ^- transitions and allows the double- Λ schemes to be realised. For CPT clocks adopting Lin||Lin, the relevant double- Λ transitions are the $\Delta m_F = 2$.

In this scheme, the resonances driven by the transitions in Fig. 2.6 (a) (the $m_F = 0-0$) are naturally destructive because of an opposite sign in one of the four Clebsch-Gordon coefficients, causing a simultaneous ‘bright’ and ‘dark’ state to occur [40, 47]. The double- Λ for the $m_F = 0-0$ and the $\Delta m_F = 2$ are shown in Fig. 2.6 (a) and (b) respectively, with Clebsch-Gordon coefficients for each transition also annotated.

However, the $\Delta m_F = 2$ shown in Fig. 2.6 (b) is also driven at two-photon resonance. The Zeeman sub-levels with an m_F greater than zero experience a linear

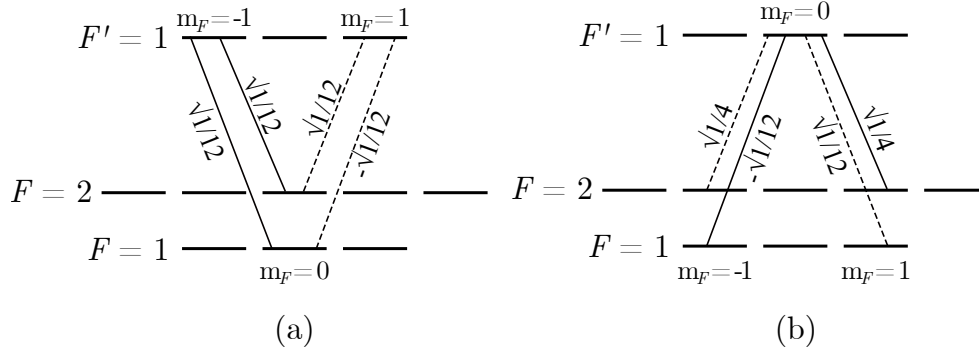


Figure 2.6: Two double- Λ schemes on the D_1 line of ^{87}Rb , with the dipole matrix elements for the relevant σ^\pm transitions [40]. (a) The $m_F = 0-0$ scheme connected via the $F' = 1$ excited state. In this scheme, the negative coefficients on one of the transitions causes the two superpositions to be orthogonal and cancel each other out. (b) The $\Delta m_F = 2$ scheme driven via the $F' = 1$ excited state. This generates two dark states across $\Delta m_F = \pm 2$, that occur (for low magnetic field) at two-photon resonance.

magnetic field dependent frequency shift. The sign of the shift depends on the Landé g factor for the hyperfine ground states, which has equal magnitude but opposite sign for the $F = 1$ and $F = 2$. The individual Λ -systems connect the $F = 1$ and the $F = 2$ and thus the linear Zeeman shift cancels, causing the dark states to occur at two-photon resonance (the un-shifted hyperfine ground state splitting). However, this also means the two-photon detuning required to optically pump atoms into the dark state also exhibits a linear sensitivity to magnetic field [38, 43, 51]. Therefore, each independent system, (Λ_\pm) , experiences a Zeeman shift with opposing sign given by [38, 40, 41]:

$$\Delta\nu = 431 \text{ Hz/G}^2 \pm 2786 \text{ Hz/G}. \quad (2.21)$$

This describes the first and second-order Zeeman shifts for each Λ that are addressed

individually. As a result, the shift introduces an additional interference effect that is highly dependent on magnetic field and can be clearly observed using Raman-Ramsey interferometry [38, 41, 47]. An additional feature of this scheme is that the dark resonances driven by each Λ -system can be spectrally resolved at high magnetic field [47], further proving that the $m_F = 0-0$ Λ -scheme is not driven in Lin||Lin CPT.

In terms of excited state, the contrast of the resonance corresponding to the $\Delta m_F = 2$ is maximised when the ground states are coupled via the $F' = 1$ hyperfine level. When coupled via the $F' = 2$, the $\Delta m_F = 2$ transitions are suppressed because of couplings to the extra Zeeman sub-levels present in $F' = 2$.

Lin \perp Lin

Alternatively, one can realise the $m_F = 0-0$ resonance by introducing a $\pi/2$ rotation between the linear polarisations of each CPT field [52, 53]. This method was first demonstrated experimentally in 2005 for thermal caesium atoms by Zanon *et al.* [44], and then later in 2010 by Xi *et al.* for cold rubidium atoms [54].

In order to describe how a common dark state can be realised on the $m_F = 0-0$, despite the negative Clebsch-Gordan coefficient, we refer back to our initial description of one dark state formed in a single Λ -system in Sec. 2.2.1. Here, we showed that a non-coupled state exists in this configuration, such that $\hat{H}_I |NC\rangle = 0$ and thus $|NC\rangle$ is a dark state. This time we want to re-define the interaction to include the transition coefficients as well as a relative angle of polarisation between the two fields, $\vec{E}_a(t)$ and $\vec{E}_b(t)$. We use the same nomenclature as in Sec. 2.2.1 and an extra level is added to the description. A four-level system that is used to describe double- Λ CPT with a common dark state is shown in Fig. 2.7. The common dark state

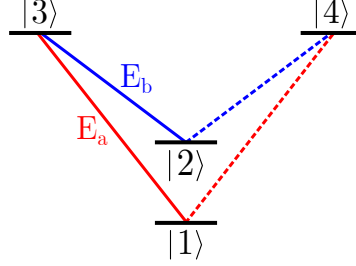


Figure 2.7: A simplified level diagram for describing how a common dark state can be formed between ground states $|1\rangle$ and $|2\rangle$, using two excited states $|3\rangle$ and $|4\rangle$. The driving fields, $\vec{E}_a(t)$ and $\vec{E}_b(t)$, are assumed to be resonant with transitions: $|1\rangle \rightarrow |3, 4\rangle$ and $|2\rangle \rightarrow |3, 4\rangle$, respectively.

is created between two ground states, $|1\rangle$ and $|2\rangle$, via couplings with two excited levels, $|3\rangle$ and $|4\rangle$. The same fields that were defined in Eqn. 2.2 in Sec. 2.2.1 are used, except that we want to introduce relative polarisation. To do this, we will use the electric dipole operator and the Clebsh-Gordon coefficients to account for the circularly polarised components of the interacting light.

We assume the fields are co-propagating along an axis, z , and that $\vec{E}_b(t)$ forms an angle θ with $\vec{E}_a(t)$. The fields are now defined as [52]:

$$\vec{E}_a(t) = \frac{E_a}{2\sqrt{2}} (e^{-i(\omega_a t + \phi_a)} + e^{i(\omega_a t + \phi_a)}) \hat{e}_x \quad (2.22a)$$

$$= \frac{E_a}{2\sqrt{2}} (e^{-i(\omega_a t + \phi_a)} + e^{i(\omega_a t + \phi_a)}) (\hat{e}_- - \hat{e}_+), \quad (2.22b)$$

$$\vec{E}_b(t) = \frac{E_b}{2\sqrt{2}} (e^{-i(\omega_b t + \phi_b)} + e^{i(\omega_b t + \phi_b)}) (\cos(\theta)\hat{e}_x + \sin(\theta)\hat{e}_y) \quad (2.22c)$$

$$= \frac{E_b}{2\sqrt{2}} (e^{-i(\omega_b t + \phi_b)} + e^{i(\omega_b t + \phi_b)}) (e^{i\theta}\hat{e}_- - e^{-i\theta}\hat{e}_+), \quad (2.22d)$$

where $\hat{e}_\pm = \mp \frac{(\hat{e}_x \pm i\hat{e}_y)}{\sqrt{2}}$. The total Hamiltonian for the interaction is now defined as:

$$\hat{H}_I = \hat{H}_a + \hat{H}_b = -\vec{d} \cdot \left(\vec{E}_a(t) + \vec{E}_b(t) \right). \quad (2.23)$$

Here, d_\pm is the electric dipole operator that accounts for the circular components of the linearly polarised light, $d_\pm = \mp \frac{(d_x \pm id_y)}{\sqrt{2}}$. The circularly polarised components (σ^\pm transitions) that make up the Λ -systems shown in Fig. 2.7 are described by the Clebsh-Gordon coefficients (c_{ij}) such that $\langle i | d | j \rangle = d_{ij} = c_{ij}d$. Inserting the electric fields from Eqn. 2.22 into 2.23 gives:

$$\hat{H}_a = \frac{E_a}{2\sqrt{2}} \left(e^{-i(\omega_a t + \phi_a)} + e^{i(\omega_a t + \phi_a)} \right) (d_+ - d_-), \quad (2.24a)$$

$$\hat{H}_b = \frac{E_b}{2\sqrt{2}} \left(e^{-i(\omega_b t + \phi_b)} + e^{i(\omega_b t + \phi_b)} \right) (e^{i\theta} d_+ - e^{-i\theta} d_-). \quad (2.24b)$$

With reference to Fig. 2.8; field $E_a(t)$ interacts with $|1\rangle \rightarrow |3\rangle$ and $|1\rangle \rightarrow |4\rangle$ and field $E_b(t)$ interacts with $|2\rangle \rightarrow |3\rangle$ and $|2\rangle \rightarrow |4\rangle$. Thus the \hat{H}_a and \hat{H}_b terms must include interaction with the additional excited state. It has been proven in [52] that when the interaction is transformed into the rotating frame, \hat{H}_a and \hat{H}_b become \tilde{H}_a and \tilde{H}_b . The rotating wave approximation can be applied to derive \tilde{H}_a [52]:

$$\tilde{H}_a = \frac{dE_a}{2\sqrt{2}} \left[e^{i\phi_a} (c_{41} |4\rangle \langle 1| - c_{31} |3\rangle \langle 1|) + e^{-i\phi_a} (c_{41} |1\rangle \langle 4| - c_{31} |1\rangle \langle 3|) \right], \quad (2.25)$$

and for \hat{H}_b :

$$\begin{aligned} \tilde{H}_b = \frac{dE_a}{2\sqrt{2}} & (e^{i(\phi_b-\theta)} c_{42} |4\rangle \langle 2| - e^{i(\phi_b+\theta)} c_{32} |3\rangle \langle 2| \\ & - e^{-i(\phi_b+\theta)} c_{32} |2\rangle \langle 3| + e^{-i(\phi_b-\theta)} c_{42} |2\rangle \langle 4|). \end{aligned} \quad (2.26)$$

Similar to Sec. 2.2.1, the dark states that form can be described using linear superpositions defined as $|\text{Dark}\rangle = \alpha |1\rangle + \beta |2\rangle$ that must satisfy:

$$\left(\hat{H}_a + \hat{H}_b \right) |\text{Dark}\rangle = 0. \quad (2.27)$$

Substituting Eqns. 2.25 and 2.26 into Eqn. 2.27 gives the expressions:

$$\frac{\beta}{\alpha} = -\frac{E_a c_{31}}{E_b c_{32}} e^{i(\Delta\phi-\theta)} = -\frac{E_a c_{41}}{E_b c_{42}} e^{-i(\Delta\phi-\theta)}, \quad (2.28)$$

where we can see that a dark state common to both Λ -systems occurs when:

$$e^{i2\theta} = \frac{c_{42} c_{31}}{c_{41} c_{32}}. \quad (2.29)$$

Considering c_{ij} are the Clebsh-Gordon coefficients for the D_1 line of ^{87}Rb , then states $|1\rangle$ and $|2\rangle$ correspond to the $|F = 1, m_F = 0\rangle$ and $|F = 2, m_F = 0\rangle$ sub-levels. The state $|3\rangle$ is the $|F' = 2, m_F = -1\rangle$ and state $|4\rangle$ is the $|F' = 2, m_F = 1\rangle$. In Fig. 2.8 (a), the double- Λ for the $m_F = 0-0$ CPT state is drawn on the D_1 line via the excited state $F' = 2$. The Clebsh-Gordon coefficients are also annotated beside

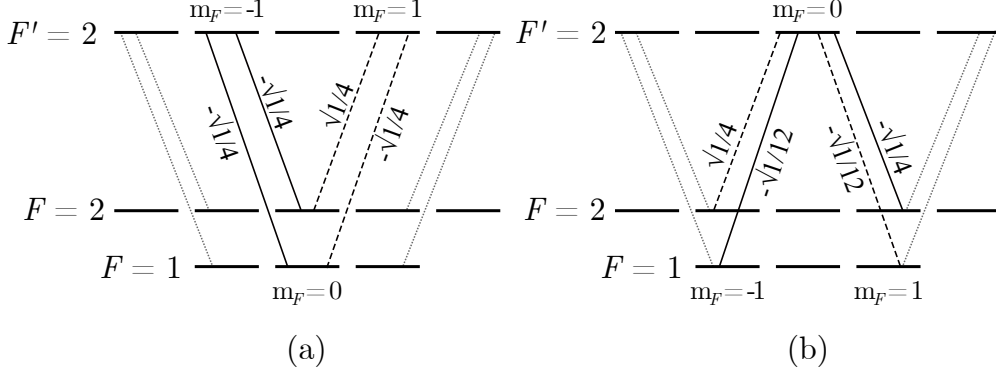


Figure 2.8: Two double- Λ schemes on the D_1 line of ^{87}Rb , with the dipole matrix elements for the relevant σ^\pm transitions [40]. (a) The $m_F = 0-0$ scheme connected via the $F' = 2$ excited state. In this scheme, the negative coefficients on one of the transitions causes the two superpositions to be orthogonal and cancel each other out. (b) The $\Delta m_F = 2$ scheme driven via the $F' = 2$ excited state. The resonances driven in this scheme are suppressed by the extra couplings from $|F = 1 \& 2, m_F = \pm 1\rangle$ to the $|F' = 2, m_F = \pm 2\rangle$ highlighted by the dotted lines.

their respective transition. The other double- Λ system, the $\Delta m_F = 2$, is shown in Fig. 2.8 (b). From Fig. 2.8 (a), we see that the coefficients $c_{31} = c_{32} = c_{41} = -c_{42}$ for the $m_F = 0-0$. Thus the relative dark states corresponding to excited states $|3\rangle$ and $|4\rangle$ are:

$$|\text{Dark}_3\rangle = \frac{1}{E_\Lambda} (E_b |1\rangle - E_a e^{-i(\Delta\phi+\theta)} |2\rangle) \quad (2.30a)$$

$$|\text{Dark}_4\rangle = \frac{1}{E_\Lambda} (E_b |1\rangle + E_a e^{-i(\Delta\phi-\theta)} |2\rangle), \quad (2.30b)$$

where $|\text{Dark}_3\rangle$ corresponds to transitions connected via excited state $|3\rangle$, $|\text{Dark}_4\rangle$ to excited state $|4\rangle$ and $E_\Lambda = \sqrt{E_a^2 + E_b^2}$. Assuming both fields are in phase ($\Delta\phi = 0$), when $E_a = E_b$ and the relative angle, θ , is zero then the dark state created via transitions with $|3\rangle$ ($|\text{Dark}_3\rangle$) will be a bright state for the dark state created via

$|4\rangle$. Equation 2.29 states that a common dark state exists when $e^{i2\theta} = -1$, therefore introducing an angle of $\theta = \pi/2$ will allow states $|\text{Dark}_3\rangle$ and $|\text{Dark}_4\rangle$ to exist simultaneously.

The rotation of $\pi/2$ between the relative linear polarisations allows constructive interference of the dark states at $m_F = 0$, and gives rise to the high-contrast scheme $\text{Lin}\perp\text{Lin}$. Therefore, we infer that it is possible to drive all three dark states described previously in Sec. 2.4.2 (see Fig. 2.5). However, this does not necessarily benefit atomic clock operation as the Zeeman shift still induces a linear sensitivity to magnetic fields for the $\Delta m_F = 2$.

Referring back to Fig. 2.8 (b), the $\Delta m_F = 2$ is shown for the D_1 line and connected to the excited hyperfine level $F' = 2$. The extra sub-levels within the $F' = 2$ cause four extra couplings to arise that suppresses the $\Delta m_F = 2$, leaving only the $m_F = 0-0$. In Fig. 2.8 (b), these extra couplings are from the $|F = 1 \ \& \ 2, m_F = \pm 1\rangle \rightarrow |F' = 2, m_F = \pm 2\rangle$ states.

It was previously shown that the individual Λ structures in the $\Delta m_F = 2$ experienced a Zeeman shift shown in Eqn. 2.21. For the $m_F = 0-0$, the Zeeman shift for each Λ is quadratic:

$$\Delta\nu = 575 \text{ Hz/G}^2. \quad (2.31)$$

In summary, an atomic clock utilising the $\text{Lin}||\text{Lin}$ CPT scheme benefits more from using the $F' = 1$ excited state due to the higher achievable resonance contrast [29]. However, this system will also experience an inherent linear sensitivity to magnetic fields. Adopting $\text{Lin}\perp\text{Lin}$ CPT instead will overcome this sensitivity when the $F' = 2$ is used as the common excited state [55], but the achievable CPT contrast is

lower due to incoherent couplings to additional states.

2.5 Ramsey-CPT

Ramsey interferometry was first demonstrated using a molecular beam as a means of obtaining atomic spectroscopy from a ‘split interrogating field’ [5]. The discovery showed that spectroscopy of the molecular beam could be obtained despite the interrogation field not being continuous, and would later win Norman F. Ramsey part of the Nobel Prize in physics in 1989 [56].

The technique is widely used in atomic clocks and frequency references as it significantly reduces AC-stark shifts of the atomic energy levels. This occurs during the interaction of atoms with light that is near-resonant with an atomic transition, and cause systematic shifts of the resonance frequency one is trying to measure. In Ramsey interferometry, the spectroscopy is obtained by splitting the interaction into two zones in space or two pulses in time. The probing field is only on at the beginning and the end of the interaction, therefore the perturbation on the energy levels is minimised.

2.5.1 Ramsey Fringes

A simple way to describe the Ramsey interaction is to consider a two-level system. An oscillating field, $\vec{E}(t) = E \cos(\omega t)$, interacts with the two-level system that is comprised of levels $|1\rangle$ and $|2\rangle$. For this system, the atomic wavefunction of the system can be expressed as:

$$\psi(t) = c_1 e^{-i\omega_1 t} |1\rangle + c_2 e^{-i\omega_2 t} |2\rangle, \quad (2.32)$$

where c_1 and c_2 are the complex amplitudes of the two states, such that the population in each state is given by $|c_k|^2$. Substituting the wavefunction in the time-dependent Schrödinger equation (TDSE) from Sec. 2.2.2 leads to the coupled differential equations:

$$i\dot{c}_1 = \Omega \cos(\omega t) e^{-i\omega_{21}t} c_2, \quad (2.33a)$$

$$i\dot{c}_2 = \Omega \cos(\omega t) e^{i\omega_{21}t} c_1. \quad (2.33b)$$

For this system, we can find a solution by making the assumption that all the population begins in the lower level $|1\rangle$, $c_1(0) = 1$ and $c_2(0) = 0$, and by neglecting fast oscillating terms in the rotating wave approximation (RWA). When the oscillating field is on resonance with the atoms, such that $\omega - \omega_{21} = 0$, then we can reach an approximation for the probability of finding the the atom in the upper state:

$$|c_2(t)|^2 = \sin^2\left(\frac{\Omega}{2}t\right). \quad (2.34)$$

This relation provides a basic description of ‘Rabi flopping’, or when the interaction causes the population to oscillate between two levels. Therefore, if $\Omega t = \pi$, all the population in $|1\rangle$ has been pumped into $|2\rangle$, thus introducing the concept of a π -pulse. Similarly, a $\pi/2$ -pulse, where the interaction time is half that of a π -pulse, pumps atoms into a superposition of levels $|1\rangle$ and $|2\rangle$.

The $\pi/2$ -pulse is the first step in performing a Ramsey sequence, which is shown in Fig. 2.9. The initial $\pi/2$ pulse pumps atoms into a superposition, and then the oscillating field is turned off allowing the atoms to freely evolve for a time T .

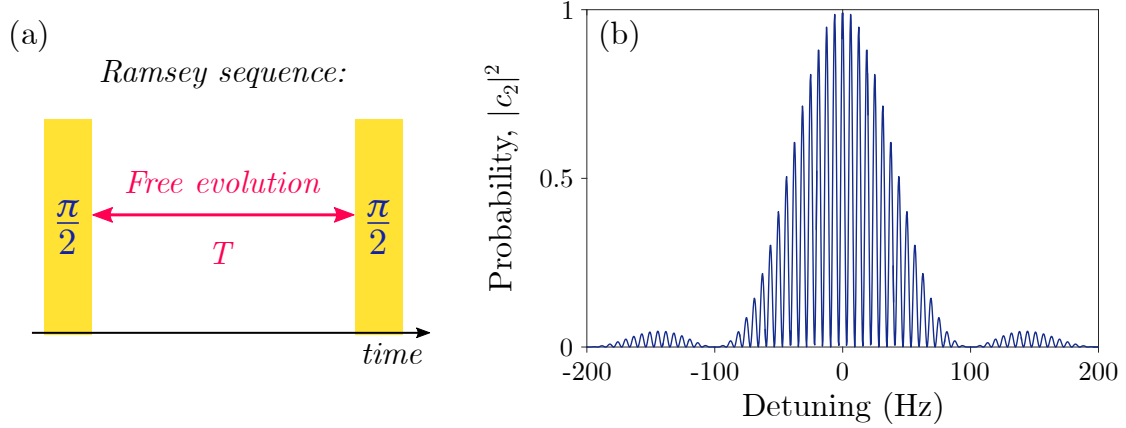


Figure 2.9: (a) A schematic of a basic Ramsey sequence. The atoms are pumped into a superposition following the first $\pi/2$ -pulse. Then the interaction is switched off and the atoms will freely evolve for a time T . A second $\pi/2$ -pulse is applied to probe the phase difference between the frequency of the oscillating field and the atomic resonance frequency. (b) Ramsey fringes as a modulation of the Rabi excitation profile. By measuring the probability of the atom being in the excited state after the sequence, fringes are observed with a frequency of $f = 1/T$.

During free evolution the phase of the applied field and the atomic phase precess without external perturbations. A second $\pi/2$ pulse is then applied after T . The interaction can be described using the probability of finding the atom in $|2\rangle$ after the sequence [5, 57]:

$$|c_2|^2 = \left| \frac{\Omega\tau}{2} \right|^2 \left(\frac{\sin^2(\delta\tau/2)}{(\delta\tau/2)^2} \right) \cos^2 \left(\frac{\delta T}{2} \right), \quad (2.35)$$

where $\delta = \omega - \omega_{21}$ is detuning of the field from the resonance frequency and τ is the pulse length. From this relation, we can see the overall sinc function that describes the Rabi excitation profile, and the fringes that are generated during the free-evolution time. When the population is probed after the sequence, the result is

a modulated Rabi excitation profile with interference fringes that depend on T as $f = 1/T$. If the oscillating field was completely out of phase with the atoms, then the atoms will be pumped back into $|1\rangle$. If the atoms were in phase with the field, then they will be in $|2\rangle$, the excited state.

2.5.2 Ramsey in CPT Clocks

For Ramsey-CPT clocks such as the experiment covered in this thesis, the technique is altered slightly but follows a similar sequence of events. The technique is often referred to as Raman-Ramsey due to the nature of the two-photon transitions and was experimentally realised in the 1980s for atoms at room temperature [58–61].

In the Ramsey-CPT case, the interaction is not exactly a $\pi/2$ pulse. It is an optical pumping effect. The interaction with the CPT driving field is split into two pulses that are separated in time by T . The first pulse pumps atoms into the dark state with a set detuning, and phase associated to the CPT laser fields, as was described in Sec. 2.2. The first pulse defines the superposition, similar to the $\pi/2$ -pulses in the previous section. However, the pulses of the CPT field are not a set length. As long as the atoms are in the dark state when the first interaction is finished, the superposition is set.

During free evolution or dark period, phase between the splitting frequency of the atomic transitions (f_{HFS}) and the variable frequency difference between the CPT fields is accumulated. A second pulse of the CPT light maps the accrued phase into an obtainable absorption signal, realising a CPT resonance that is modulated with interference fringes corresponding to $1/T$ [61]. This means that interaction and

probing of the atomic state is achieved using one laser beam within the same region in space. Examples of Ramsey-CPT fringe data obtained using the first generation CPT clock apparatus are discussed in detail in Chapter 4.

2.6 Chapter 2 Summary

The aim of this chapter was to provide introductory theory for coherent population trapping (CPT) and the additional techniques that were applied in the experiments undertaken for this thesis. The first section, Sec. 2.2, introduced the CPT phenomena, using a simple three-level picture that described the interaction of a bi-chromatic field, including relative phase and frequency detuning, with a three-level system. This describes the formation of a non-coupled or dark state between the two ‘ground’ states of the three-level picture. The optical pumping dynamics were discussed in Sec. 2.2.2 using density matrix formalism to show the dependence of atomic population on the relative detuning between the interacting fields. Following this, the fine, hyperfine and sub-hyperfine (Zeeman) level structure of the atomic species Rubidium were described in Sec. 2.3. This was to provide a foundation for further technical discussion of ‘high-contrast’ CPT schemes that were described in Sec. 2.4.2. For the experiments presented later in this thesis, the $\text{Lin}\perp\text{Lin}$ polarisation scheme was applied and therefore a brief theoretical description was provided. Finally, the last section (Sec. 2.5) introduced Ramsey interferometry as an experimental technique widely applied in atomic clocks, and then concludes with by describing an adaptation of Ramsey interferometry for CPT clocks.

Chapter 3

Laser Cooling with Diffractive Optics

3.1 Introduction

Between the 1970s and 80s interest in manipulating particles with laser light inspired the first experiments for the trapping, and cooling of neutral atoms [8, 62]. There are a multitude of resources from this era regarding the theory [63–65]. Starting with the invention of the laser in 1960 [66], several key points in the history of laser cooling are highlighted by the table in Fig. 3.1. The timeline in the table concludes where the theory of sub-Doppler cooling was realised in 1989 [63]. Lectures from the winners of the 1997 Nobel prize for physics by Claude Cohen-Tannoudji [67], Steven Chu [68] and William D. Phillips [69] encompass the story of this era and are an excellent place to begin reading.

In recent years a large drive for utilising cold atoms for field-grade atomic sen-

Maiman 1960	First Laser
Ashkin 1970	Manipulation of micron-sized particles with laser light
Hänsch and Schawlow 1975	Proposal for cooling atoms with laser light
Wineland and Dehmelt 1975	Proposal for cooling ions with laser light
Ashkin 1978	A method for optically trapping and cooling atoms
Wineland <i>et al.</i> 1978	First demonstration of slowing ions in a trap
Phillips and Metcalf 1982	First demonstration of decelerating an atomic beam with laser light
Prodan <i>et al.</i> 1985	Cooling atoms with counter-propagating laser beams
Chu <i>et al.</i> 1985	First demonstration of 3D optical molasses
Raab <i>et al.</i> 1987	First demonstration of a magneto-optical trap (MOT)
Lett <i>et al.</i> 1988	Sodium atoms cooled below the Doppler limit
Dalibard <i>et al.</i> 1989	Theory of sub-Doppler cooling

Figure 3.1: References are: Maiman [66], Ashkin [70], Hänsch and Schawlow [71], Wineland and Dehmelt [72], Ashkin [73], Wineland *et al.* [74], Phillips and Metcalf [75], Prodan *et al.* [76], Chu *et al.* [8], Raab *et al.* [77], Lett *et al.* [78] and Dalibard *et al.* [63]

sors lead to the development of simpler and less power consuming approaches to laser cooling. The work done for this thesis was completed using two experimental apparatuses based on micro-fabricated grating chips for laser cooling. The main motivation behind using the grating chips was to reduce the size of the large apparatus required for laser cooling, and this was achieved by replacing most of the cooling beams with a single input beam to a reflector or diffraction grating. This chapter begins with a general introduction to laser cooling and trapping of neutral atoms, including Doppler, sub-Doppler and magneto-optical trapping (MOT). This leads onto the grating-MOT concept and how it was characterised for the two clock experiments.

3.2 Basic Principles

The concept of laser cooling originates in a few early publications in the 1970s. The manipulation of micron-sized particles was demonstrated by Ashkin in 1970 [70], and later a theoretical proposal for cooling neutral atoms with light was introduced by Hansch and Schawlow in 1975 [71], and similarly for ions by Wineland and Dehmelt in the same year [72]. The first real method for optically trapping atoms was also proposed by Ashkin in 1978 [73], before the first experimental demonstration of decelerating ions in a trap by Wineland *et al.* [74].

Decreasing an atom's velocity reduces the motional effects seen in fast-moving free atoms, such as Doppler-broadening, and allows for narrower linewidths to be obtained and thus a higher precision in spectroscopy. The interaction of incident laser light on the atoms results in a velocity-dependent force, which ultimately causes

a damping of the atom's movement. The concept is akin to a viscous drag-like friction force experienced by a particle in fluid, and as such was named optical molasses [69].

3.2.1 Doppler Cooling

The force exerted from the laser light onto the atoms is often described as a scattering or radiative force and originates from a net momentum change in the incoherent scattering process. Consider two counter-propagating laser beams incident on a two-level atom moving in one dimension. The laser beams are slightly detuned below the atomic resonance frequency. If the atomic motion opposes the direction of the beams, then the resulting Doppler shift can be exploited to give a velocity-dependent momentum exchange. The atom absorbs a photon from the beam and receives a 'kick' along the direction of the incoming photon. Once the atom spontaneously decays, it will then recoil again while emitting a photon in a random direction. After many scattering events, the net force opposes the atoms movement and can be described by:

$$\vec{F}_{\text{scatt}} = \hbar \vec{k} \gamma_{\text{scatt}}, \quad (3.1)$$

where $h(= \pi \hbar)$ is Planck's constant, \vec{k} is the wavevector ($= 1/\lambda$), and γ_{scatt} is the scattering rate, or photon absorption rate:

$$\gamma_{\text{scatt}} = \frac{\Gamma}{2} \frac{S}{1 + S + 4(\Delta/\Gamma)^2}. \quad (3.2)$$

Here, $S (= I/I_{\text{sat}})$ is the ratio of the incident light intensity to the saturation intensity. In this picture, the damping of the atomic velocity balances with the heating that is induced by the random direction of the second emitted photon to predict a limit to the atomic temperature:

$$T_D = \frac{\hbar\Gamma}{2k_B}. \quad (3.3)$$

The Doppler limit was proposed from a two-level approach and does not include the magnetically sensitive sub-levels within the hyperfine states [40, 63]. For rubidium, this temperature is $T_D \sim 146 \mu\text{K}$. Optical molasses has the capability to cool the atomic temperature, but it does not trap the atoms and merely inhibits their escape from the laser beams for a finite time.

3.2.2 Sub-Doppler Cooling

As mentioned above, the Doppler limit to the temperature of a cloud of atoms was theoretically derived using a model two-level system. The mechanisms that result in laser cooling below the Doppler limit are attributed to optical pumping among the sub-levels and polarisation gradients in the standing waves formed where the counter-propagating beams intersect. In this case, the multi-level nature of alkali atoms must be included to better describe the dynamics of sub-Doppler cooling process. Here, we have included a description of two types of sub-Doppler dynamics that contribute to the cooling.

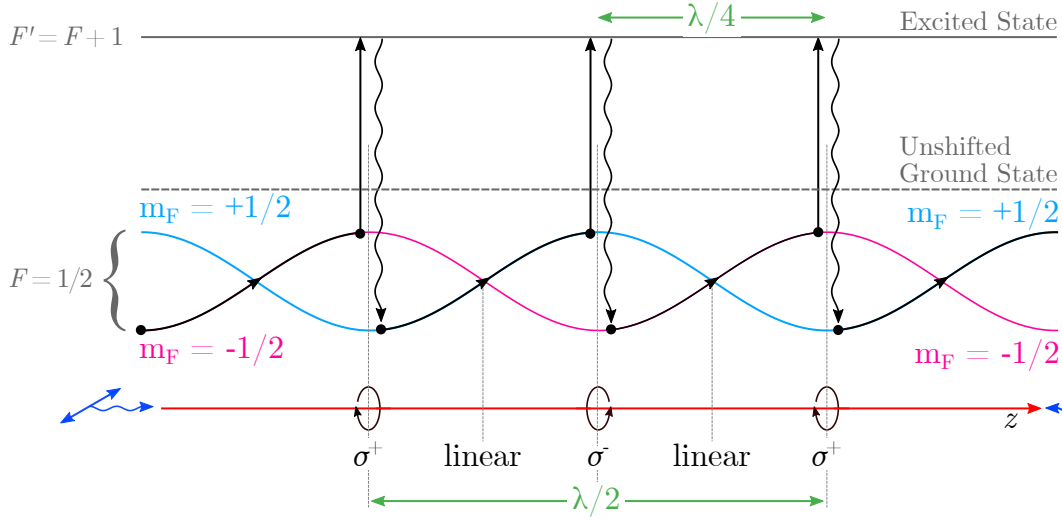


Figure 3.2: Polarisation gradient cooling in one dimension with counter-propagating laser beams and orthogonal linear polarisations. The light shift experienced by the ground state sub-levels is shown for the $m_F = +1/2$ (blue) and $m_F = -1/2$ (pink). Optical pumping occurs at the top of the potential ‘hills’, and varies from σ^+ to σ^- .

Sisyphus Cooling ($\text{Lin} \perp \text{Lin}$)

In the first description, shown in Fig. 3.2, two counter-propagating beams along direction z have orthogonal linear polarisations. Interference between the two beams creates a standing wave in which the polarisation is spatially modulated such that the light shift of the ground state sub-levels is also modulated along z . As a result the atoms experience optical pumping which varies from σ^+ to σ^- every $z = \lambda/4$.

We consider an atomic configuration with a $F = 1/2$ ground state and corresponding Zeeman sub-levels, $m_F = \pm 1/2$, with an excited state of $F' = F + 1$. The sub-levels experience different AC-Stark shifts and optical pumping rates due to the different transition strengths between ground and excited sub-levels. The change in light shift and pumping rate is correlated with polarisation and consequently with

position on the wavelength scale along the direction of the beams (z). The atom's position in Fig. 3.2 is shown by the black circles, and it is moving from left to right along z . At the top of the first 'hill', the light pumps the atom into the level with lower energy ($m_F = +1/2$) via σ^+ transitions. As the atom moves through the next $\lambda/4$ into the next region it climbs a potential hill caused by the sub-level light shift. When it reaches the top the optical field drives a σ^- transition into $m_F = -1/2$, and the atom ends up in the lowest energy state again. The potential gained from climbing the polarisation gradient is radiated away by an emitted photon after each ascent and the total effect is a loss of kinetic energy, or further damping of atomic motion along the direction of the laser beams [63]. This scheme was named Sisyphus cooling because of the similarities to a character in the Greek mythology, who was forever doomed to roll a boulder up a hill [65, 68, 69].

Induced Orientation Cooling ($\sigma^+ - \sigma^-$)

In the second configuration, the two counter-propagating beams have opposing circular polarisation. Unlike the linear configuration described above, this is not a form of Sisyphus cooling as the light-shift experienced by the ground state sub-levels remains constant along z . The total polarisation is linear everywhere, but the direction rotates around the beam propagation axis, z , forming a helix with a pitch equal to the laser wavelength, λ .

In this example we have an atom with ground state $F = 1$ and excited level $F' = F + 1$, which is positioned between the counter-propagating beams. If the atom is stationary, the linearly polarised field optically pumps atoms symmetrically among the m_F sub-levels with atoms preferentially being pumped into $m_F = 0$. If

the atom is now moving, the helical direction of the polarisation induces a change in atomic orientation as it traverses the field. This means there is a difference in the probability of absorption (or transition strength) from each beam and the optical pumping symmetry is broken. The imbalanced scattering as the atoms try to keep up with the local field results in a damping of the atomic motion which is stronger than that induced by Doppler cooling [63, 65].

3.2.3 Magneto-Optical Trapping

The optical cooling that was described above provides a velocity-dependent force that is excellent at slowing the atoms within the cooling region at the intersection of the laser beams. However, the atoms are free to eventually diffuse from the intersection of the cooling beams. We want to tailor the atom-light interaction such that a restoring force is induced that pushes the atoms towards a common region in space, consequently trapping them. Applying a spatially-varying magnetic field allows the construction of a trap that causes the force due to light scattering to acquire a position dependence. This means a magneto-optical trap (MOT) allows the atoms to both be cooled by the light and spatially trapped by the magnetic field, significantly increasing the number of atoms within the trapping region.

A typical MOT is comprised of a set of anti-Helmholtz coils positioned around the intersection of the molasses beams. In this configuration, the two coils of wire carry current in opposite directions to generate a magnetic field which has a local minimum at the centre of the coils. This is drawn in Fig. 3.3 for three axes: x and y which are the radial axes and z (through the coils) which is called the axial

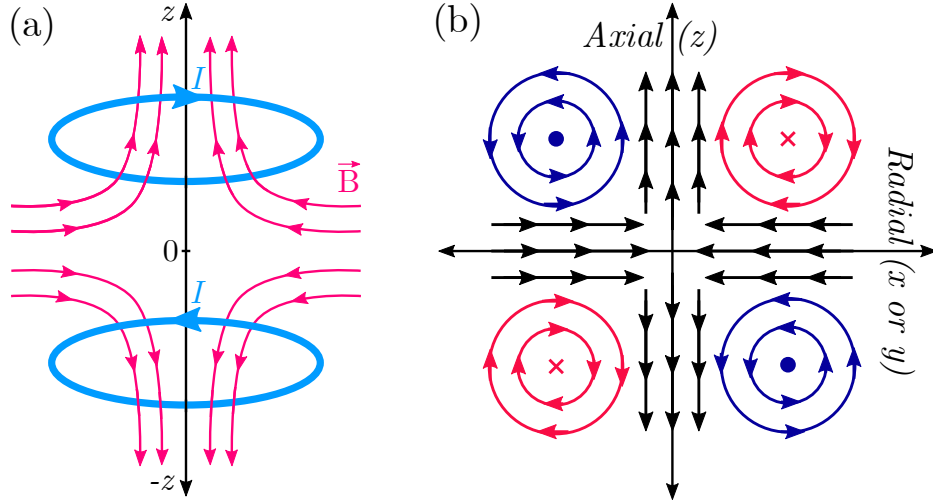


Figure 3.3: (a) Schematic of anti-Helmholtz coils for trapping atoms. (b) Magnetic field lines to show the direction of \vec{B} .

direction in Fig. 3.3. The quadrupole field is approximately linear near the centre of the trap, and we can see that the direction of the magnetic field \vec{B} changes direction as it moves through $z = 0$ in Fig. 3.3. This is also true for the x and y radial axes, although the direction is flipped in comparison to z .

The simplest way to describe MOT dynamics is to start in one dimension, and we will use the z (axial) direction as is shown in Fig. 3.4 for an atom with ground state $F = 0$ and excited state $F' = 1$. In this case, our quantisation axis will be set by the direction of \vec{B} and we introduce two counter-propagating beams, red-detuned from the atomic transition by δ , and with circular polarisation of the same handedness. The beams are labelled ‘*laser 1*’ and ‘*laser 2*’ in Fig. 3.4 by the wide red and blue arrows. The magnitude and direction of \vec{B} is illustrated by the solid green arrows as z increases away from the centre of the trap. Under the magnetic field, \vec{B} , the degeneracy on the Zeeman sub-level structure is lifted. Considering the transition

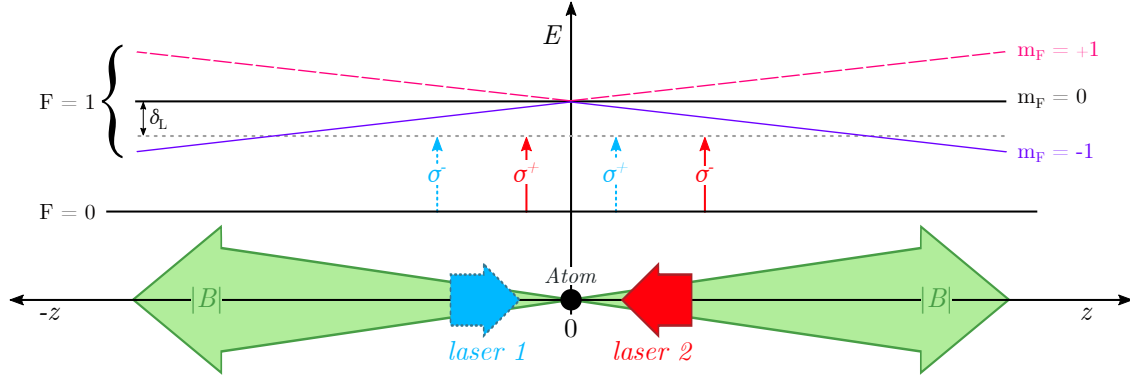


Figure 3.4: Schematic of the 1D atom-light interactions for the transition $F = 0 \rightarrow F' = 1$. On the left of the diagram, *laser 1* will drive σ^- transitions (blue dashed arrow) due to the handedness of its polarisation relative to the quantisation axis, set by \vec{B} .

shown in Fig. 3.4, we can use the Zeeman architecture of the excited state (F') to describe the trapping mechanics. The energy shift increases linearly with $|\vec{B}|$ (and position) for the $m_F = +1$ (pink dashed line) and decreases linearly for the $m_F = -1$ (solid purple line).

On the left-hand side of the diagram, '*laser 1*' drives σ^- transitions because of its direction relative to \vec{B} (the quantisation axis) and '*laser 2*' drives σ^+ transitions. The direction of \vec{B} flips as we move through $z = 0$, and therefore the transitions driven by '*laser 1*' and '*laser 2*' on the right-hand side of the diagram also flip. This means that if the atom moves to the left or right of the trap centre it will always encounter an opposing beam which will preferentially drive σ^- transitions because the gradient of the $m_F = -1$ is being tuned closer to the laser frequency (grey dotted line) by \vec{B} . This creates an imbalanced radiative force that depends on position, z . The resulting net force pushes atoms towards the region at the centre of the

trap where the magnetic field minimises. This one-dimensional scheme can also be expanded to include the x and y radial directions and realise a three-dimensional trap.

3.3 Building a GMOT

The MOT, after it was first demonstrated in 1987 [77], quickly became the foundation of many experiments that ranged from basic spectroscopy and fundamental atomic physics, to building the primary standards for time-keeping and further still to the discovery of new quantum states of matter.

A large step towards downsizing experimental apparatus required for laser cooling is to reduce the number of optics required. This was first successfully done with a single beam of circularly polarised cooling light coupled to a pyramidal or conical mirror to create a pyramid-MOT [79]. However, in this arrangement the atoms were trapped below the edges of the mirror and were hard to access. Later, in 2009 [80], a similar optic with angled mirrors as shown in Fig. 3.5 (a) was used to demonstrate a tetrahedral-MOT where the trapping region was extended to the area above the mirrors [81]. The angled mirror approach was developed from the mirror-based optic to a planar diffraction grating arrangement shown in Fig. 3.5 (b). Finally, the diffraction grating patterns were etched onto silicon wafer [see Fig. 3.5 (c)] to allow for freedom of customisation and a scalable method of fabrication from which a commercial product was developed [82].

The single-beam MOT configurations described above relied on the reflected or refracted beams balancing the intensity from the input beam and providing the

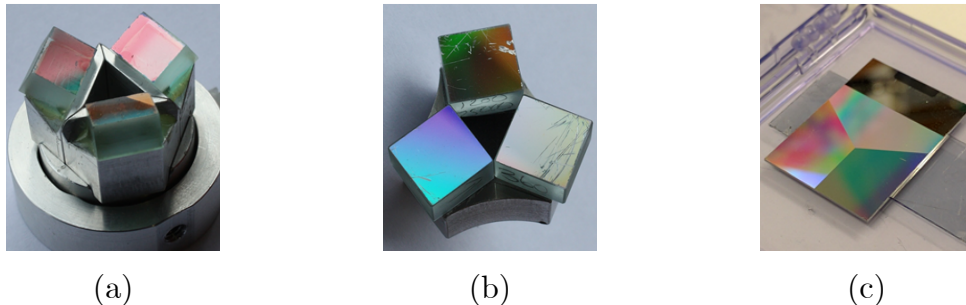


Figure 3.5: (a) Homebuilt mirror-MOT apparatus. (b) Mirrors replaced with commercial gratings. (c) Micro-fabricated grating chip, etched into silicon wafer.

correct polarisation when arranged correctly with the MOT quadrupole magnetic field. The micro-fabricated diffraction gratings have been very successful in terms of simplicity of alignment and are now commercially available after extensive characterisation [83, 84]. Grating chips like the one in Fig. 3.5 (c) have shown the capability of preparing 10^7 rubidium atoms from vapour and 10^8 when loaded from a 2D MOT [85]. Previous publications have reported sub-Doppler molasses temperatures as low as $3 \mu\text{K}$ [86].

3.3.1 Experimental Methods

This section outlines two rubidium grating magneto-optical trap (GMOT) experiments. The former was used as the first generation of CPT clock based at Strathclyde, and describes the cooling apparatus where most of the work for this thesis was carried out. The second was a simplified and portable version of this GMOT apparatus, and was intended to eventually become a prototype portable cold atom clock. The second generation was successful in terms of demonstrating a portable apparatus for cold rubidium atoms that could be safely operated for public outreach

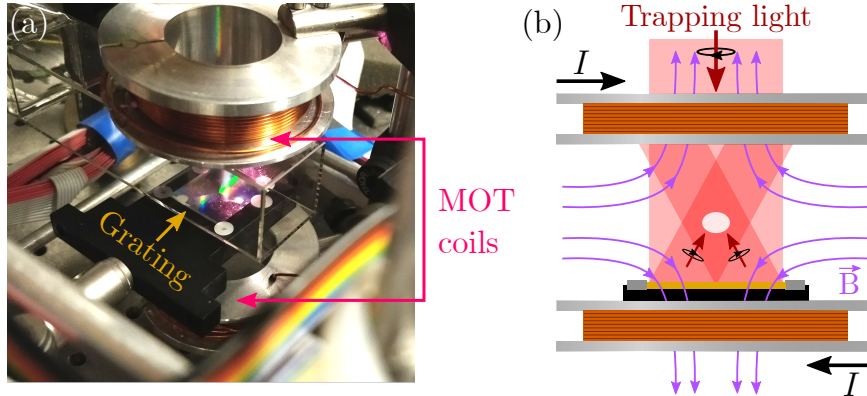


Figure 3.6: (a) Photograph showing the GMOT apparatus used for the clock experiment. (b) Schematic of a GMOT showing the single input beam, quadrupole MOT coils and grating position.

events. In both cases, a grating chip such as the one shown in Fig. 3.5 (c) was used. The type of micro-fabricated chip used in the experiment was often referred to as ‘TRI’, as it was an arrangement of three linear gratings etched to make up a triangle. A photograph of the apparatus is shown in Fig. 3.6 (a), which includes the MOT coils, glass cell and TRI grating. The MOT coils are arranged co-axial with the input beam of cooling light, as is shown in the schematic in Fig. 3.6 (b).

Laser Stabilisation

A requirement for cooling is a laser linewidth that is much smaller than the size of the splitting frequencies between the hyperfine levels. This means we can introduce a small red-detuning from resonance. The laser frequency should also be stabilised to a relevant transition. A useful feature of cooling rubidium atoms is that cheap laser diodes are available which operate at the wavelength of the D₂ line in ⁸⁷Rb; 780 nm. However, the typical linewidth of these diodes is around 100 MHz. By integrating an

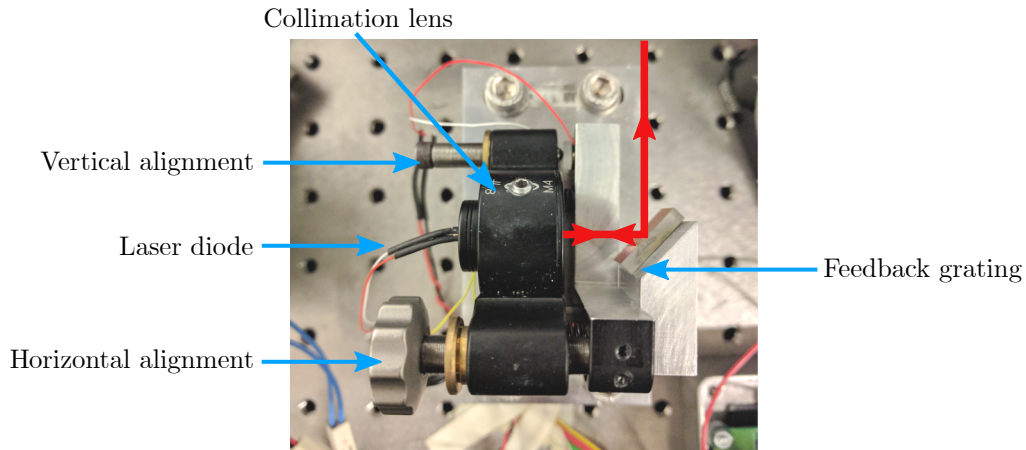


Figure 3.7: Photograph of the repump ECDL unit. The output beam from the collimation lens is shown by the red arrow.

external cavity around the diode, the operating linewidth can be reduced to a few hundred kHz [87]. In an external cavity diode laser (ECDL), a holographic grating is used to provide frequency dependent feedback to the laser diode in what is commonly referred to as the Littrow configuration. Figure 3.7 provides a photograph of the repump ECDL used in the experiment. Each ECDL unit contains a collimation lens for shaping the output beam from the diode and a holographic grating to feedback and create the external cavity. A Peltier element and thermistor provides passive stabilisation to the laser unit temperature, and as such, the cavity length. The grating angle is positioned either manually or with a piezoelectric actuator, adjusting the external cavity length. By hand, the ‘vertical’ orientation of the grating is used to align the external cavity feedback, until the cavity created between the grating and the front facet of the laser diode dominates the internal diode cavity. The ‘horizontal’ orientation can be used to tune the external cavity wavelength, in combination with laser diode current and temperature. The frequencies required for the cooling and

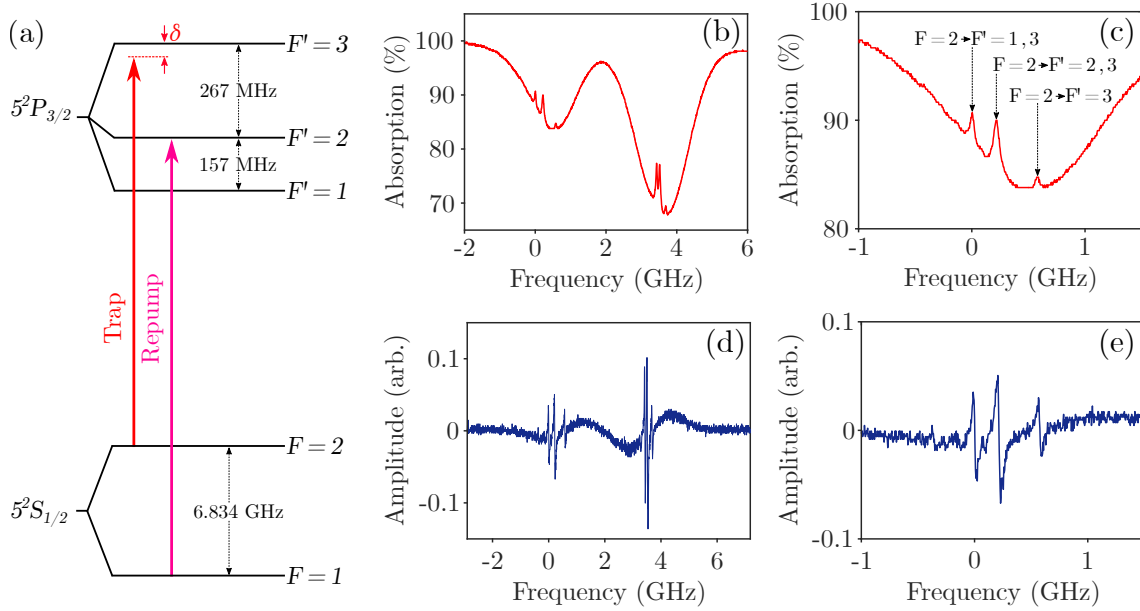


Figure 3.8: (a) The D_2 line for ^{87}Rb . (b) Saturated absorption spectroscopy for the trapping transitions only, for ^{87}Rb and ^{85}Rb . (c) The Doppler-free features for the trapping transitions in ^{87}Rb . (d) and (e) show the de-modulated error signals for (b) and (c).

trapping of ^{87}Rb are shown in Fig. 3.8 (a) for the D_2 line. Two transitions are highlighted in this diagram; labelled trap and repump. The trap excites from $F = 2 \rightarrow F' = 3$, red-detuned by approximately one linewidth ($2\pi \times 6$ MHz). The repump then closes the cycle of transitions by resonantly exciting from the $F = 1 \rightarrow F' = 2$.

To lock the ECDLs, active feedback is provided to the laser diode current and the piezo stack using in-house built electronics. For accurately addressing the correct transitions, the Doppler-free spectroscopy of the rubidium atoms was used by applying the saturated absorption spectroscopy technique. The D_2 saturated absorption spectra for the trapping transitions in both ^{85}Rb and ^{87}Rb are plotted in Fig. 3.8 (b), with the ^{87}Rb line plotted in (c). Modulation of the diode current and

piezo stack (fast for current, slow for piezo) is applied by the locking electronics. The Doppler-free absorption signals are detected using photodiodes and then fed back into the locking electronics for de-modulation. The de-modulated error signal [shown in Fig. 3.8 (d) and (e)] then passes through an integrator circuit to supply feedback to the piezo and current, and thus the ECDL is locked to an atomic signal.

Optical Bench

The optical bench for the trapping part of the experiment is shown in Fig. 3.9. Two separate ECDLs were used for generating trap and repump light, each with their own saturated absorption spectroscopy set-up for locking. For the trap laser, a weak probe was picked off using a glass slide and for the repump laser a polarising beam splitter was used. In both, the probe was double-passed through a glass Rb vapour cell in order to see the Doppler-free absorption features on the photodiodes. The optical power of the trap laser was amplified using a tapered amplifier (TPA780P20 butterfly package with LDC2500 current and temperature controller), which was seeded with approximately 20 mW of trap light. The trap ECDL was locked to the crossover resonance corresponding to the $F = 2 \rightarrow F' = 2, 3$ transition within the $5^2P_{3/2}$ manifold of the ^{87}Rb D₂ line. An acousto-optical modulator (AOM) operating at frequency $f_{\text{AOM}} = 133 \text{ MHz} - \delta$ was used to bring the frequency of the cooling light onto resonance with the $F = 2 \rightarrow F' = 3$ transition, minus a small detuning. An RF switch was also used for fast extinction of the cooling light and an RF mixer was used to drop the optical power in stages during optical molasses. During molasses both the detuning, δ , and the optical power of the trap light were varied to improve the cooling. The trap frequency was detuned in two stages to $\sim 60 \text{ MHz}$, and the

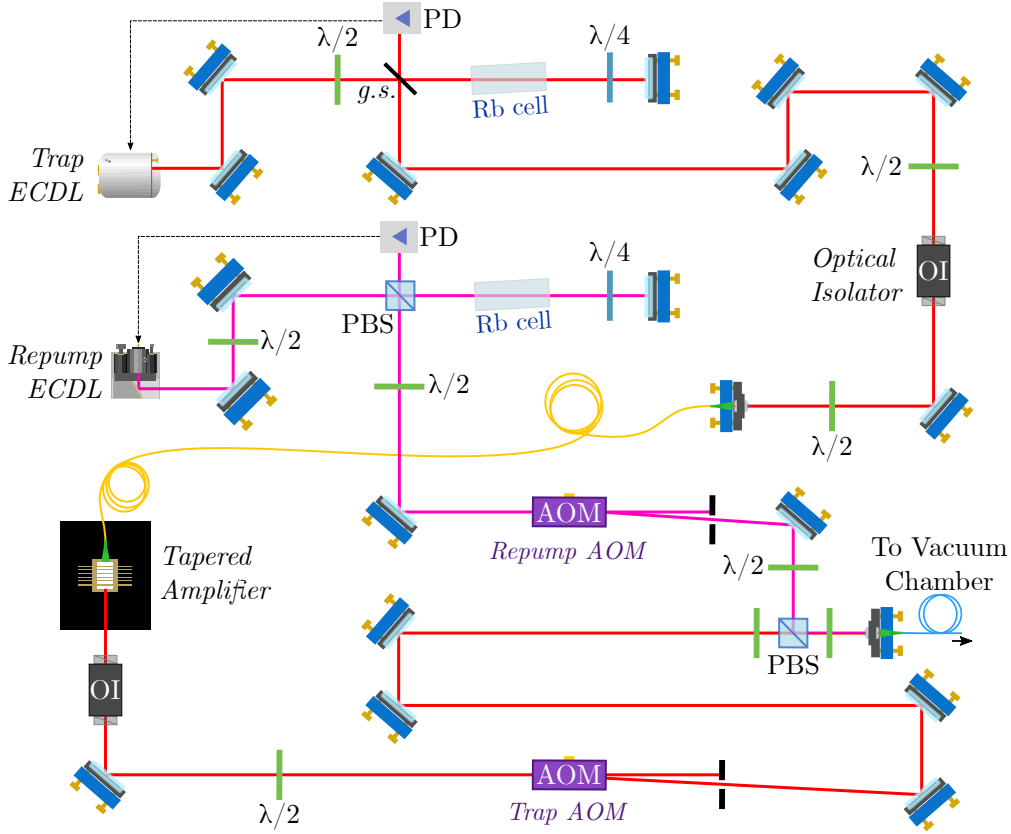


Figure 3.9: Optical path for the trap and repump lasers in the Clock I apparatus, up to where both beams were fibre-coupled and transported to the vacuum chamber. ECDL: external cavity diode laser, AOM: acousto-optical modulator, PBS: polarising beam splitter. PD: photodiode, g.s.: glass slide.

intensity was stepped to approximately 10% of the MOT intensity. This due to the experimental sequence control being limited to digital signals. The full experiment sequence, including the clock interrogation, is covered in Chapter 4.

The repump ECDL was also locked to a crossover resonance in the saturated absorption spectroscopy, the $F = 1 \rightarrow F' = 1, 2$. A second AOM operating at 77 MHz was used to bring the repump laser frequency onto resonance with the

$F = 1 \rightarrow F' = 2$ transition and allow for fast intensity switching of the repump light. Both beams were combined using a PBS and then coupled into a common single-mode polarisation-maintaining optical fibre. The fibre carried the light over to the vacuum cell, magnetic coils and grating chip ensemble which was shown in Fig. 3.6.

Grating Chip Apparatus

A schematic and photograph of the GMOT apparatus used in the first generation CPT clock is provided by Fig. 3.6. The fibre carrying the trap and repump light was secured and passively temperature stabilised using foam padding and table covers. The output light from the fibre was expanded and collimated to a diameter comparable with the size of the grating chip. The expanded beam was circularly polarised by a quarter waveplate before it reached the vacuum cell. The grating chip was held securely in a custom-made plastic mount just underneath the glass vacuum cell, which was not anti-reflection coated. In addition to the glass cell, the vacuum chamber is also comprised of two SAES Getters rubidium dispensers and a relatively small Gamma Vacuums 3S-DI ion pump (2 L/s) with its own μ -metal shielding.

Time of Flight Imaging

In the time of flight technique, the temperature of a cloud of atoms can be measured using the images of the atoms after they have been released from the trap. The atoms are captured in the MOT first, then the magnetic gradient is switched off to allow the atoms to be cooled in optical molasses. The cloud is then released from

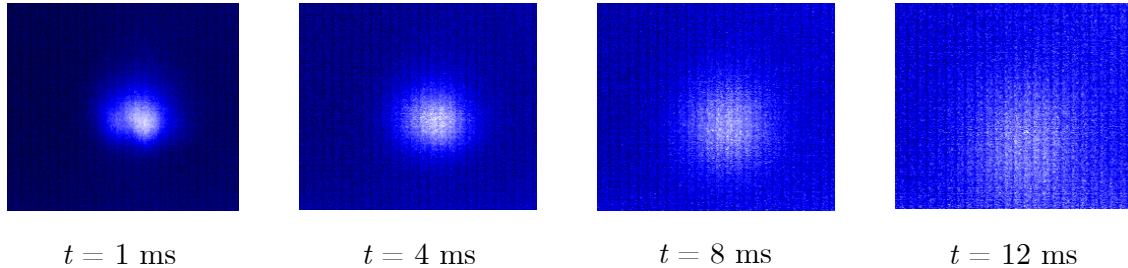


Figure 3.10: Fluorescence images of Clock I's ^{87}Rb GMOT with different drop times. Each image is a single run of the time-of light imaging sequence, since the fluorescence imaging technique is destructive.

the optical molasses and allowed to ballistically expand and fall under gravity for a set time t , which we call the flight time. After t , an image of the cloud is taken either using the absorption of a probe beam or by measuring the fluorescence of the atoms after excitation with resonant light. In our case, we used the fluorescence of the trap light to excite and image the atoms after an optical molasses stage. In each sequence, a new MOT was loaded, the gradient coils were switched off for optical molasses and then trap light was switched off for t before being switched back on to image the cloud. For the fluorescence images, a camera was triggered to measure the light emitted from the cloud after the trapping light was pulsed on. A second image is typically taken after all of the atoms have left the cooling region and subtracted order to cancel some of the background noise on the image. As an example, a series of images are shown in Fig. 3.10 with different expansion time in the GMOT apparatus. The images allow one to build up a picture of the expansion of the cloud over time. Ideally, we observe a homogeneous expansion and see the atoms smoothly fall under gravity. Movement which is not in the direction of gravity is a sign that the atoms are experiencing an additional force from an imbalance in

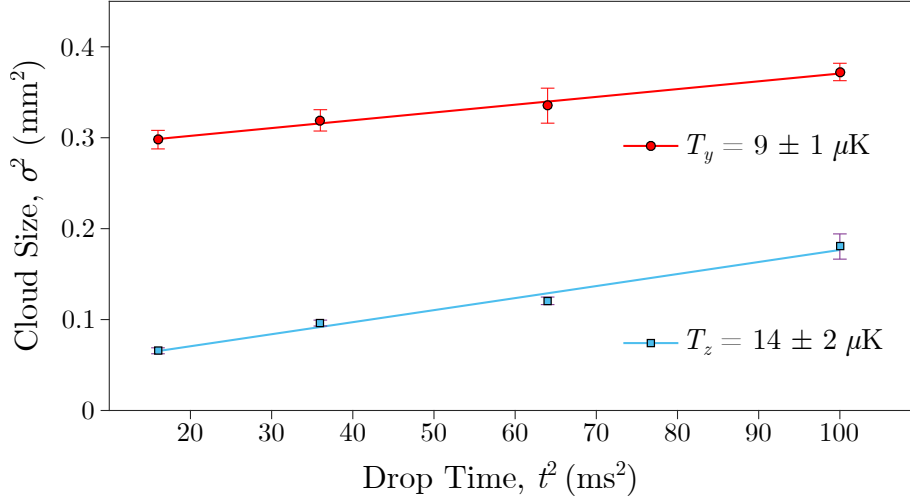


Figure 3.11: The width of the atomic cloud squared, σ^2 (mm²) versus drop time or time-of-flight squared, t^2 (ms²). For each axis of the cloud, z or y , a Gaussian model was fit to the integrated profiles to obtain the width for different drop time. The parameters from the linear fits to the data in the above figure were used to calculate the temperatures labelled beside the data.

the trapping and cooling region. The temperature of the atoms can be estimated by calculating the expansion rate of the cloud. We assume a Gaussian distribution on both axes of the cloud, and measure the difference in the width, σ , after time of flight t :

$$\sigma(t) = \left(\sigma(0) + \frac{k_B T}{M_{Rb}} t^2 \right)^{1/2}. \quad (3.4)$$

Here, k_B is Boltzmann's constant ($= 1.38 \times 10^{-23} \text{ m}^2 \text{ kg s}^{-2} \text{ K}^{-1}$) and M_{Rb} ($= 87 \times 1.67 \times 10^{-27} \text{ kg}$) is the mass of the rubidium atoms. We can then calculate a temperature T from the gradient, m , of a linear fit of $\sigma^2(t)$ against flight time t^2 :

$$m = \frac{k_B}{M_{Rb}} T. \quad (3.5)$$

A typical measurement of the molasses temperature is plotted in Fig. 3.11 for both axes of the cloud. The y - and z -axes correspond to two orthogonal axes of the measurement. Here, z is co-axial with the MOT coils and input trapping beam and also corresponds to the direction of gravity. The data in this plot was not taken at the same time as the ToF images from Fig. 3.10. In general, the GMOTs exhibit an elongated shape due to the shape of the trapping volume, which is caused by angle of the refracted trapping beams. This is also observed in the temperature measurement from Fig. 3.11, as a larger width is observed along the y -axis of GMOT.

3.4 Generation II Apparatus

The intention of the second generation CPT clock was to build and characterise the apparatus with portability in mind, whilst still learning from the first system. The apparatus was based on another grating magneto-optical trap (gMOT) for ^{87}Rb , wherein the trapping optics, coils and vacuum cell were designed to be compact and modular. The system was comprised of three breadboards which were connected using optical fibres, allowing for each section to be individually upgraded without affecting the whole apparatus. This also meant the apparatus could be taken out of the laboratory environment, which proved useful for public outreach events and demonstrations. This section will describe some of the technical details of the second generation apparatus.

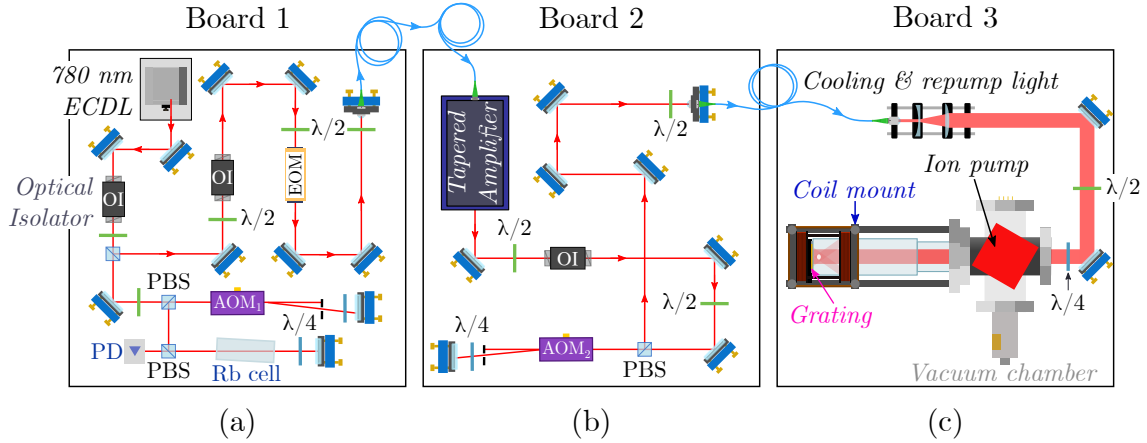


Figure 3.12: Clock II optics breadboards. (a) The ECDL, saturated-absorption spectroscopy and free-space EOM to generate sidebands for the repump. (b) Tapered amplifier (TA) and second AOM. (c) Vacuum cell and grating chip assembly.

3.4.1 Portable Optics Breadboards

The optical bench for this experiment was split into three portable 45 by 45 inch breadboards. A diagram of the optics layout for each breadboard is shown in Fig. 3.12. The first board, in Fig. 3.12 (a), contained a homebuilt ECDL operating at 780 nm with saturated absorption spectroscopy to lock the laser. This ECDL provided light for trapping and also for repumping atoms. A MOGLabs laser (DLC202) diode driver was used to control and provide feedback to the diode current and piezo voltage, as well as passive stabilisation of ECDL housing temperature. The ECDL was locked onto the hyperfine $F = 2$ to $F' = 1,3$ crossover transition, with an AOM in a double-passed configuration before the spectroscopy in order to have the ability to vary the trap detuning. This was different from the first generation, where the piezo voltage was used to control the frequency of the laser. In this case, the ECDL remained locked while the trap detuning was varied. A New Focus

4851 free-space electro-optical modulator (EOM) was used to generate sidebands on the primary beam from the laser, such that one of the sidebands addressed the repump transition. The EOM was driven at $f_{EOM} = f_{hfs} - f_{exc} + \delta = (6834.682\ 610 - 266.65 + 7)$ MHz, where f_{exc} is the separation of the trap and repump excited hyperfine levels. The frequency source for the EOM was a MiniCircuits ZX95-6640C voltage-controlled oscillator (VCO) which was driven using an analog voltage from the DAQ card in the laboratory computer. The RF voltage was then amplified and sent to the EOM such that $\sim 5\%$ of the total optical power was resonant with the repump transition.

The beam was then fibre-coupled into a tapered amplifier (New Focus TA-7613) on board 2 in Fig. 3.12 (b). This allowed for more control over the trapping laser intensity in the initial characterisation stage, via the tapered amplifier (TA) current. The beam was double-passed through a second AOM on this board, in order to bring the light from the first board onto resonance with the trap (minus a small detuning) and repump transitions for ^{87}Rb , see Fig. 3.8. This second AOM was also used for fast switching or to ramp the intensity down during optical molasses. The beam was then fibre-coupled again and transferred over to the last breadboard.

This board, drawn in Fig. 3.12 (c), contained expansion and collimation optics, as well as polarisation optics to deliver circularly polarised light through the chamber and onto the grating. The vacuum chamber itself is also drawn in Fig. 3.12 (c). The system was designed to have a glass window at the opposite end of the chamber to the main glass cell, such that the trapping beam could be sent through the entire length to the end facet of the glass cell, as is shown in Fig. 3.12 (c). The grating was held in a custom built plastic mount that could be attached to the chamber such

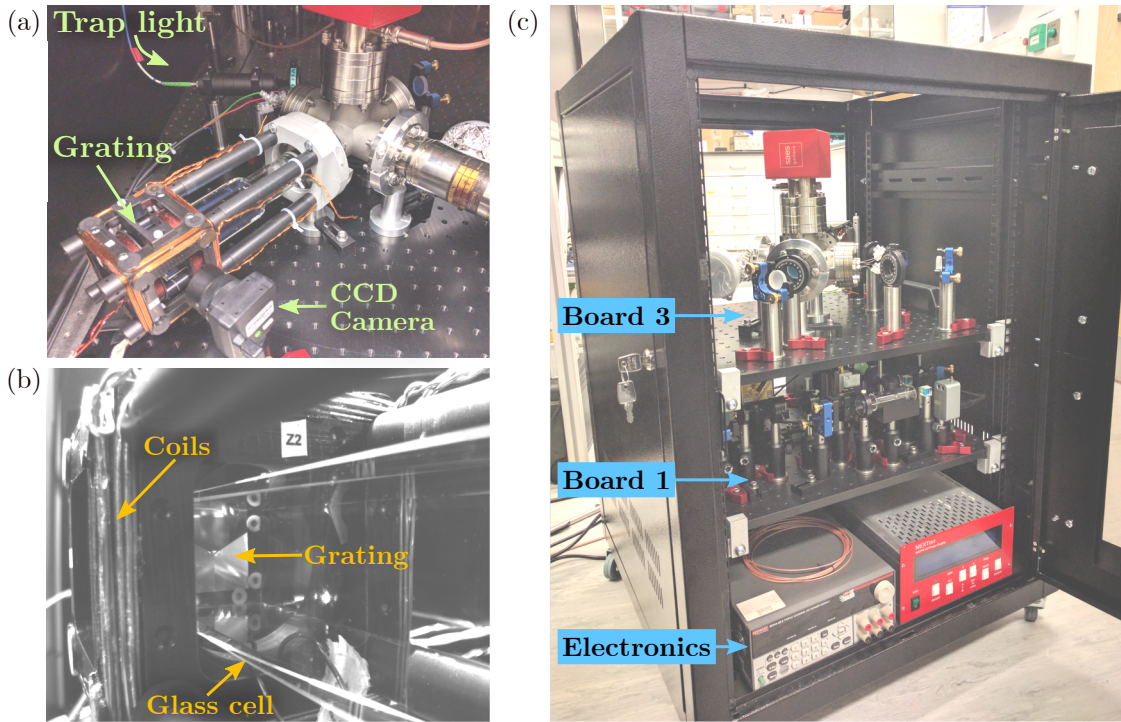


Figure 3.13: (a) The vacuum cell with the grating mount, quadrupole coils and shim coils attached. (b) The grating mounted inside the coil apparatus. (c) Breadboards 1 and 3 inside the portable demonstrator box. The second board, containing the TA, was not used for the demonstrator to save space.

that the grating chip was securely held to the end facet of the glass cell. This mount also contained the quadrupole coils for the MOT and extra shim coils for cancelling the ambient magnetic field at the position of the atom trap. Securing the grating and coil mount to the chamber facilitated the ability to move the apparatus out of the laboratory, and also meant that magnetic shielding could be easily adapted to fit around the chamber.

Figure 3.13 (a) shows a photograph of the vacuum cell on the portable bread-

board with the grating and coil mount attached. The photograph in Fig. 3.13 (b) shows a view of the mounted grating chip from outside of the glass cell. Figure 3.13 (c) shows a photograph of most of the apparatus when it was mounted inside a portable rack mount for outreach demonstrations at local conferences and science festivals. In this case, the second board with the TA [Fig. 3.12 (b)] was not included in the portable demonstrator to save space inside the rack mount. The demonstrator was used to show that cold atoms could be prepared outside of the laboratory, and was still able to trap atoms in the gMOT despite missing the extra optical power from the tapered amplifier. The electronics that can be seen on the bottom shelf are the pressure monitor for the ion pump, which regulated the vacuum inside the glass cell, and a current source that was used to drive the rubidium dispensers and control the MOT coils.

3.4.2 Experimental Control

This second generation experiment used a combination of digital and analog voltage control using a National Instruments PCIe card. LabVIEW code from the first generation GMOT experiment was used to generate the timed digital array. This array was used for controlling the magnetic quadrupole and the CCD camera. Additional analog outputs on the same card were synced with the digital array to output voltage ramps to control the laser detuning and intensity. The timing and control for a typical time of flight (ToF) imaging sequence is shown in Fig. 3.14. The AOMs were controlled using a homebuilt AOM driver that could drive up to four separate modulators. The AOM driver included voltage-controlled oscillators (VCOs), RF

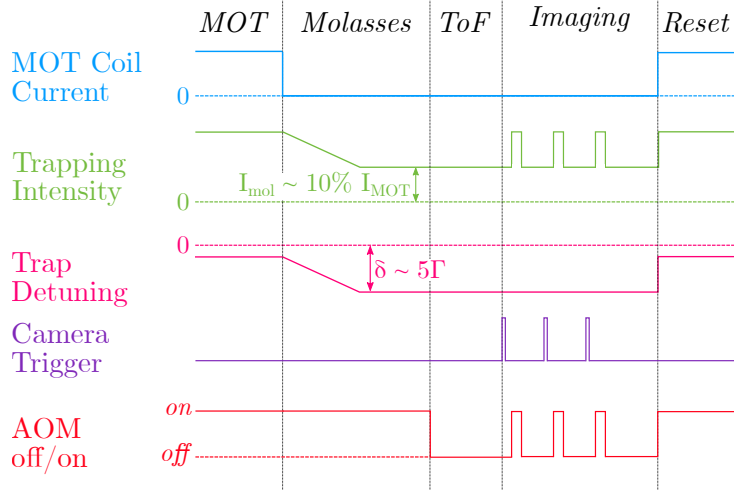


Figure 3.14: MOT and molasses timing sequence for clock II.

mixers, RF switches (if required) and RF amplifiers. The frequency and output RF power could be varied manually via trimpots on the drivers, or through two separate input analog voltages. The RF switches were controlled using a TTL voltage input.

Two linear voltage ramps were used to vary the trap detuning (AOM₁) and the intensity (AOM₂) during the molasses phase of the sequence. The ramps were analog voltage outputs that were configured in LabVIEW. We varied the trap detuning by ramping the VCO control voltage sent to AOM₁ (saturated absorption spectroscopy), such that the detuning reached $\sim 5\Gamma$ during molasses. Unlike the first generation described in Sec. 3.3.1, the ECDL remained locked and the total optical intensity was also ramped to approximately half of its initial value during the molasses stage, as opposed to applying the changes in steps.

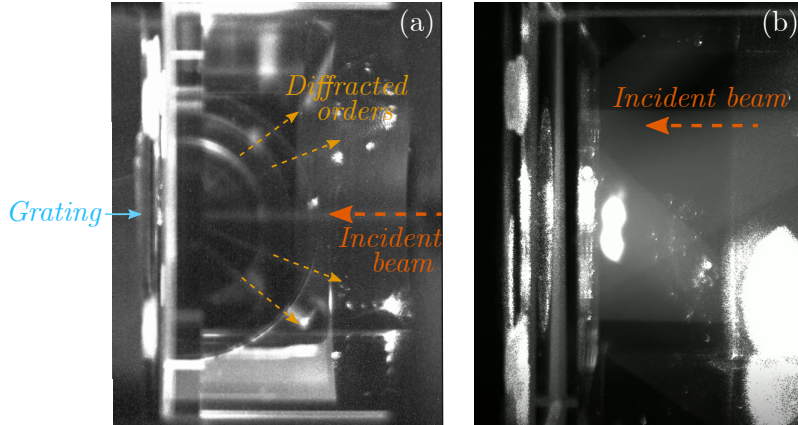


Figure 3.15: (a) Fluorescence image of the diffracted orders of the trapping beam through a pinhole. (b) Fluorescence image of the gMOT.

3.4.3 Performance

In order to measure the performance of the new system, we needed to be able to image the atoms. To do this, we used two different CCD cameras to measure the fluorescence of the atoms inside the chamber. A relatively small FLIR (previously PointGrey) Chameleon CCD camera was used to display the live images using FLIR's FlyCap software. This was mostly used in the initial alignment of the trapping beam on the grating chip, to monitor the gMOT's position over time, or for outreach events.

The second camera was a PCO Pixelfly CCD, and was used to obtain fluorescence images of the gMOT. These images were then used to measure the atom number and temperature of the cloud. This camera was triggered using a TTL from the laboratory computer with the timing sequence from the previous section shown in Fig. 3.14. We used one lens ($f = 50$ mm) in a $2f:2f$ configuration between the camera CCD and the position of the atoms. The LabView sequence acquired two

images; one with the cloud of rubidium atoms and one background image with no atoms present. The difference between the images was taken, and the subtracted image was used to measure the atom number by summing over the total pixel counts. The temperature of the cloud could also be calculated using the same technique described in Section 3.3.1.

For calculating atom number, the subtracted images were cropped in order to reduce background counts from reflections. In order to convert the detected fluorescence into a real atom number, we equate the power absorbed by the CCD and the power emitted by the MOT:

$$N = \frac{\sum(\text{pixel counts})}{\gamma_{\text{scatt}} \tau_{\text{exp}} Q_E \eta}. \quad (3.6)$$

Here, γ_{scatt} is the scattering rate described in Section 3.2.1, τ_{exp} is the exposure time of the CCD, η the solid angle and Q_E the quantum efficiency of the camera at the operating wavelength. On the ^{87}Rb D₂ wavelength (780 nm), the Q_E was approximately 20% for the Pixelfly. The solid angle was calculated using the lens radius, focal length and total working distance between object and image. This calculation was used to obtain the results shown in Fig. 3.16, which show how the atom number, N , varied with trap detuning and EOM frequency. For the trap detuning [Fig. 3.16 (a)], the data points were fitted using a Gaussian model in order to obtain the peak position. From this we can infer a maximum atom number when the trap frequency was 12 ± 1 MHz detuned from resonance. The driving frequency of the EOM set the resonance of the first order sideband with the repump transition. Data from a separate experiment where this frequency was varied and

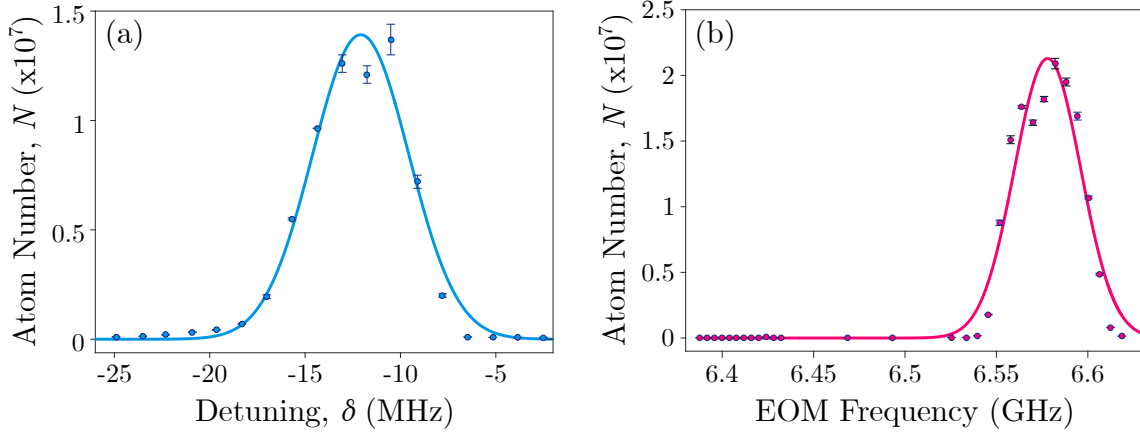


Figure 3.16: Results from two separate experiments that investigated the behaviour of the measured atom number for the second generation apparatus. In (a), the detuning of the trap laser, δ , was varied by changing the operating frequency of AOM₁. The atom number was then measured against the frequency of the EOM in (b).

the atom number was measured is shown in Fig. 3.16 (b), where the strong peak corresponds to the optimal driving frequency. The frequency output to the EOM was measured using an RF spectrum analyser as the VCO voltage was varied.

3.4.4 Current Status

The second generation was intended to be built as a portable version of the first experiment. As a portable laser cooling system, it was operated successfully outside of the laboratory for the purpose of public outreach events. However, the optical alignment had to be adjusted frequently due to poor temperature stabilisation inside the portable rack mount (see Fig. 3.13). The atom number we obtained with the system was comparable with previous gMOT apparatus, when the experiment was based in the laboratory. In terms of molasses temperature, the lowest measurement

we obtained was $\sim 100 \mu\text{K}$. This was much higher than expected, since much lower sub-Doppler molasses temperatures have previously been measured with grating-based systems. At this stage, the magnetic shield was not part of the experimental apparatus.

Currently, the vacuum chamber, along with its magnetic shield, have replaced the chamber used in the first generation. This was mainly to help progress the system as an atomic clock and rule out magnetic field noise as a limit to the frequency stability. The measured limit to the molasses temperature has been overcome using different trap and repump lasers, so it was not clear what the cause of the limitation was. There have been no issues with this part of the apparatus since it has been integrated into the main experiment.

3.5 Chapter 3 Summary

The purpose of this chapter was to describe two rubidium grating magneto-optical trap (GMOT) experiments. The cold-atom CPT experiment was based on the first, and the second laser-cooling apparatus was intended to be compact and portable. The first section of this chapter, Sec. 3.2, provides general introduction for laser-cooling and trapping of atoms, including Doppler cooling, sub-Doppler cooling and magneto-optical trapping. The second section of this chapter, Sec. 3.3, gives a technical discussion about the GMOT system used for the clock experiment. This includes a technical description of the optical bench, stabilisation of the lasers and grating chip apparatus followed by an experimental measurement of the temperature of the atoms. The final section of this chapter, Sec. 3.4, presents the second

generation GMOT apparatus. Here, the optical breadboards, control sequence for laser cooling and construction of a portable demonstrator are described. The performance, in terms of the trapped atom number, is then presented. This apparatus was successfully used in several public outreach events as a demonstration of portable laser cooling.

Chapter 4

A Cold-Atom Lin \perp Lin CPT Clock

4.1 Introduction

The first-generation CPT clock was designed to demonstrate Lin \perp Lin CPT with laser-cooled rubidium atoms in the grating magneto-optical trap apparatus previously discussed in Sec. 3.3. The experiment was used as a test-bed for gaining a better understanding of the Lin \perp Lin CPT phenomena, as well as characterising the detection of the clock signal. In our case, the clock signal was Ramsey-CPT fringes obtained in the probe laser transmission. The detected signal, and therefore the performance of the clock, is directly related to the population of atoms that are trapped in the dark state. An essential component for achieving high CPT contrast is good phase coherence between the individual CPT driving fields [29]. In this experiment, the driving field that was used to perform Lin \perp Lin CPT originated from the same laser, giving us this phase coherence inherently [55, 88, 89].

This chapter aims to describe the methods used for the first-generation cold-atom

CPT clock, and is based on work from past PhD theses [37, 53]. In the first half of this chapter, we describe the experimental methods, probing sequence, optical bench, RF electronics and detection strategy for obtaining the CPT transmission spectrum and the Ramsey fringes. The second half of this chapter describes results obtained from the experiment during characterisation. In Sec. 4.3 these results are summarised, including data from absorption imaging with the CPT beam, the detected CPT spectrum from the first pulse and finally the obtained Ramsey fringe data.

4.2 Experimental Methods

In this section, the optical bench that was used to generate the two orthogonally linearly polarised CPT fields from one laser is described. The components that contributed to the apparatus such as the rubidium spectroscopy, RF electronics chain and timing sequence for Ramsey operation are detailed.

4.2.1 D_1 Spectroscopy

The CPT experiment as a whole utilised both the D_1 and the D_2 line of ^{87}Rb . Spectroscopy on the D_2 line was used for the cooling and trapping part of the experiment (Sec. 3.3.1), and the D_1 line was used for performing the CPT spectroscopy and Ramsey interferometry. The level diagram for both the D_2 and D_1 lines of ^{87}Rb is shown in Fig. 4.1 (a) where all the transitions that were used (detunings omitted for clarity) are highlighted using coloured arrows. Two resonant CPT components are annotated with labels ‘CPT₁’ and ‘CPT₂’ which correspond to

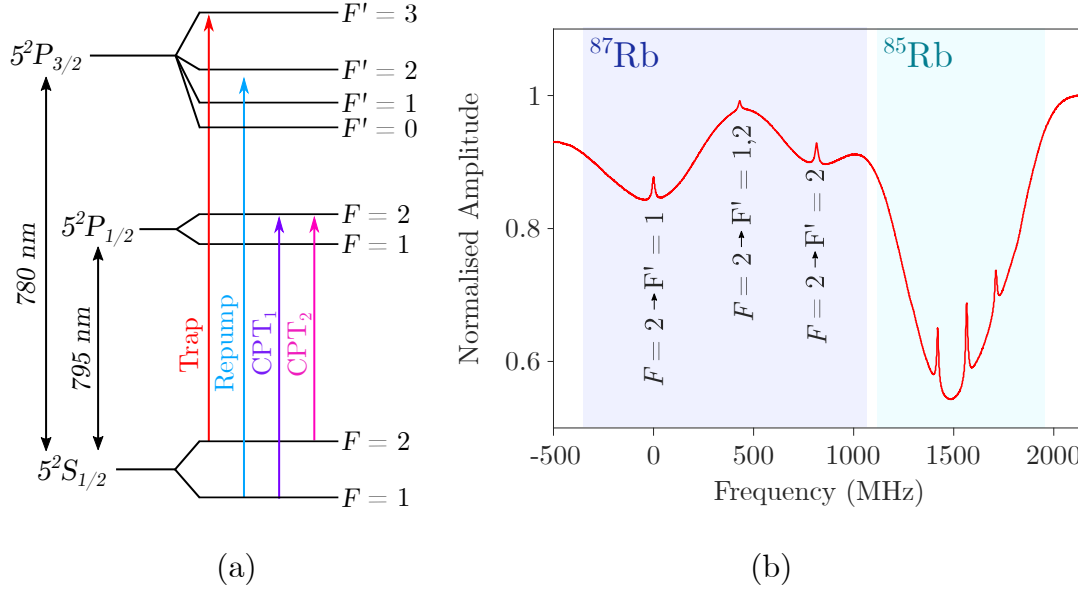


Figure 4.1: (a) Level diagram for the $5^2S_{1/2}$ to the $5^2P_{1/2}$ (D₁) and the $5^2P_{3/2}$ (D₂) manifolds in ^{87}Rb . (b) Doppler-free peaks in spectroscopy of the $F = 2 \rightarrow F'$ transitions on the D₁ line of ^{87}Rb and ^{85}Rb . The transitions for the ^{87}Rb Doppler-free peaks are labelled. This is experimentally obtained from the D₁ saturated absorption spectroscopy that was used to lock the CPT laser, and is the result of 12 averages.

the $F = 1, 2 \rightarrow F' = 2$ transitions, respectively. There are two frequency detunings that are referred to throughout this chapter and that are relevant to the CPT part of the experiment. The first is the one-photon detuning and this refers to a variable detuning from the $F' = 2$ excited state, on one of the CPT fields. The second is the two-photon detuning, often abbreviated to δ_{2ph} , and refers to a relative detuning between the fields ‘CPT₁’ and ‘CPT₂’ (see Sec. 2.2.1).

In Fig. 4.1 (b), experimentally obtained saturated absorption spectrum is plotted for the D₁ line, where the Doppler-free peaks are labelled with their corresponding transitions. For rubidium atoms, high-contrast CPT favours using the D₁ line due to

the simplicity of the hyperfine excited manifold, despite the lower absorption signal obtained in saturated spectroscopy [47]. As covered in Sec. 2.4.2, an atomic clock adopting the Lin \perp Lin CPT scheme benefits most from using the $F' = 2$ hyperfine excited state [41], therefore this was used as our excited state for CPT.

4.2.2 CPT Optics Bench

This section covers the part of the optical bench dedicated to generating the Lin \perp Lin CPT fields, and is summarised by the diagram in Fig. 4.2.

Laser Locking

The optics path begins with a commercial cat-eye ECDL (MOGLabs CEL002) operating at 795 nm. This is resonant with the D_1 line and also contains a built-in optical isolator. The ECDL current and piezo voltage were actively stabilised using saturated absorption spectroscopy and an electronic controller (MOGLabs DLC202) in the same manner as the trap and repump lasers in Sec. 3.3.1. The first AOM in the path (AOM₁ in Fig. 4.2) used a double-pass configuration and was driven by a Keysight (E4433B) frequency source. The frequency sources and driving frequencies used in this part of the experiment are also summarised in Sec. 4.2.3. The beam from the second pass through AOM₁ was used for the saturated absorption spectroscopy set-up such that the light from the ECDL was offset in frequency from its lock-point to the $F = 1 \rightarrow F' = 2$ transition. The offset caused by AOM₁ could be varied by changing the output RF frequency from the frequency synthesiser and was used to set the one-photon (or optical) detuning in the CPT transitions.

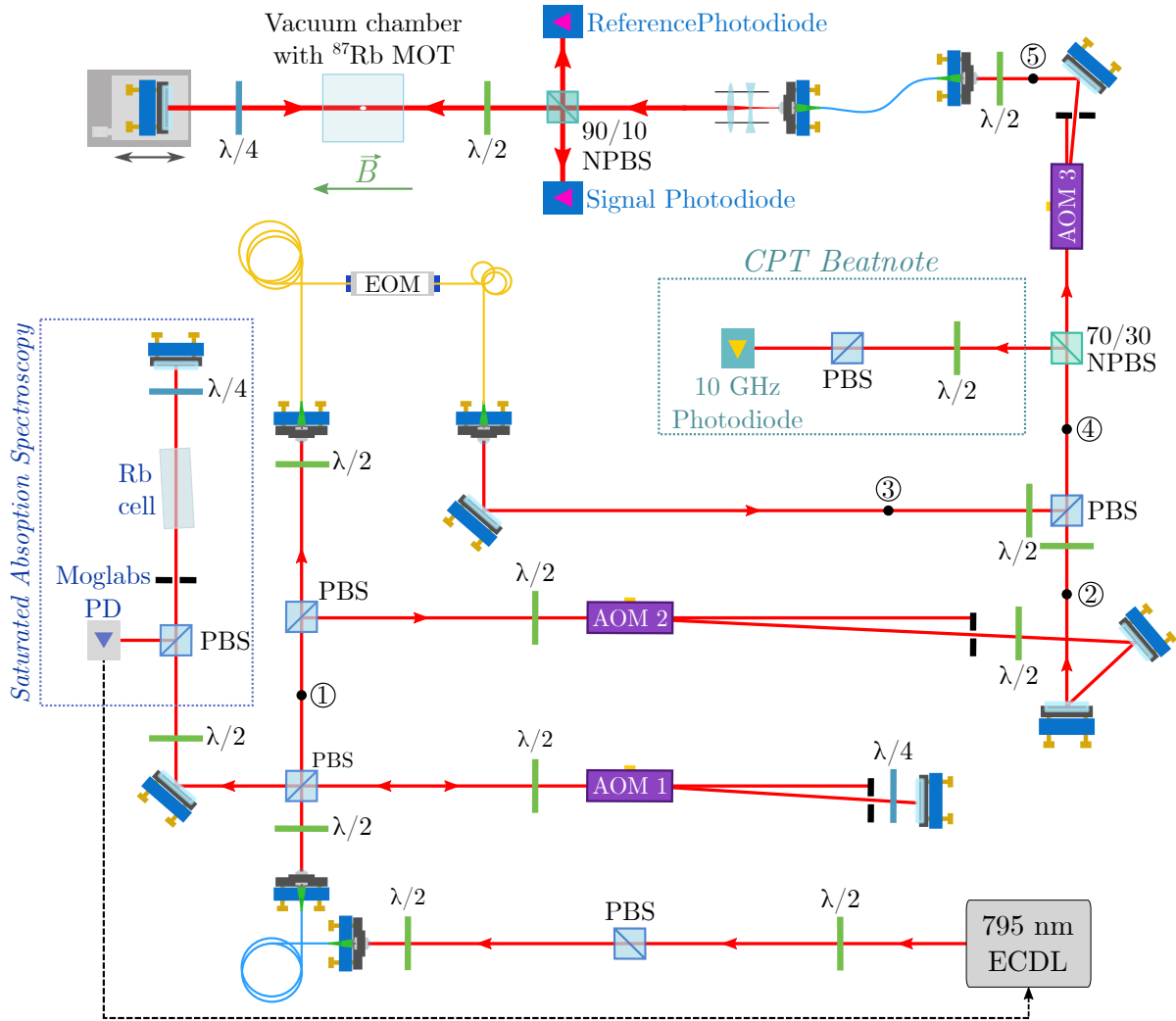


Figure 4.2: Optical layout for the part of the optical bench that was dedicated to generating the optical fields for CPT. For each of the three AOMs (AA-OptoElectronics MT200), the positive diffracted order was taken. Two non-polarising beam splitting cubes are used, that are labelled as ‘70/30’ and ‘90/10’. This refers to the output ports on the cube as reflected/transmitted. The total frequency of the laser is highlighted at certain points along the optical path (circled numbers), and this corresponds to the level diagrams in Fig. 4.3.

Generating the Lin \perp Lin Fields

A PBS was used to divide the primary beam into two paths that would eventually become the fields CPT₁ and CPT₂, orthogonally linearly polarised and resonant with the $F = 1 \rightarrow F' = 2$ and $F = 2 \rightarrow F' = 2$ transitions respectively. In one path, the beam passed through a second AOM (AOM₂ in Fig. 4.3) that was driven by a MOGLabs RF frequency synthesiser (Agile RF-421). The other output of the PBS was sent through a fibre-coupled EOM (iXBlue NIR-MPX800) to generate sidebands on the coupled light. The EOM was driven at $f_{\text{EOM}} = f_{\text{HFS}} + f_{\text{AOM3}}$, where f_{HFS} is the hyperfine splitting frequency of the ground states in ⁸⁷Rb (~ 6.8 GHz). The RF power was set such that each first-order sideband had approximately 30% of the total power. The RF amplitude and frequency of the synthesiser (Keysight E8257D) for the EOM were controlled using the laboratory computer with a timing sequence written in LabVIEW.

The diffracted beam from AOM₂ and the output light from the EOM were then re-combined on a PBS to generate a single beam that was comprised of two fields with orthogonal linear polarisation. After re-combination, 70% of the optical power was picked off using a non-polarising beam splitter (reflected/transmitted = 70/30) and was used to generate a ‘CPT’ beat-note between the field components that were separated in frequency by f_{HFS} . This frequency is ~ 6.8 GHz and is often referred to as the microwave frequency. The beat-note was produced by setting the polarisation of each component to be parallel and detecting the optical signal on a photodiode, as is shown in the schematic in Fig. 4.2. The beatnote frequency was compared to an additional frequency source (Keysight N5183B) operating around f_{HFS} , and was

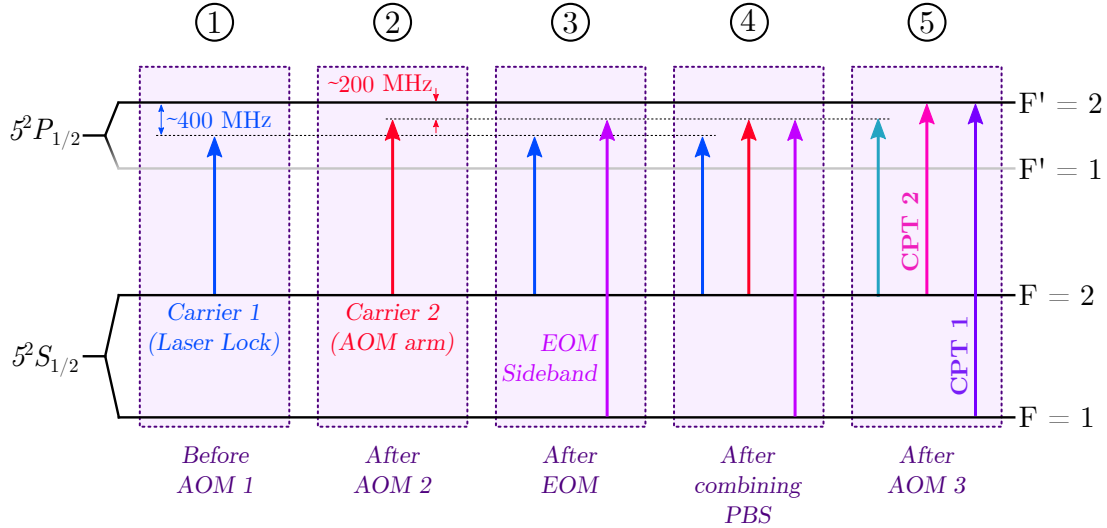


Figure 4.3: The frequency of the CPT light as we make our way downstream of the optical path, and onto resonance with optical CPT transitions labelled ‘CPT 1’ and ‘CPT 2’. The numbers inside the circles correspond to the annotated numbers along the optical path in Fig. 4.2.

used in a phase-locked loop (PLL) to suppress extra phase noise at the microwave frequency picked up from the split path [90]. The PLL is described in more detail in Sec. 4.2.3.

The remaining 30% of the optical power was coupled through a third AOM (AOM₃ in Fig. 4.2) driven by a commercial frequency synthesiser (Keysight N5171B). This shifted the frequencies of the AOM₂ beam and a single first order sideband of the EOM light onto resonance with CPT₁ and CPT₂ respectively. An RF switch was used for fast extinction of the probe beam during the clock sequence. The frequency shifts are summarised in Fig. 4.3 using numbers that correspond to position along the optical path in Fig. 4.2.

Probing the Atoms

The output beam from AOM_3 was fibre-coupled into a single-mode polarisation-maintaining fibre to ensure good spatial overlap of the two CPT fields and to produce a clean Gaussian mode for probing the atoms. A 90/10 non-polarising beam splitter reflected 90% of the probe power onto a reference photodiode for initial common-mode noise cancellation, later described in more detail in Sec. 4.2.5. The remaining 10% was used to probe the atoms in a double-pass configuration using a mirror on a translation stage. Using a 90/10 splitter was preferential when the probe beam was in a retro-reflected configuration as this meant 90% of the returning beam was reflected onto the signal photodiode, and only 10% of the signal was lost. In the double-pass configuration, the atoms are probed for CPT with counter-propagating beams such that the ground state coherence forms a standing wave that varies, with respect to the changing mirror position, with a wavelength of $\lambda_{\text{HFS}}/2 \approx 2$ cm. The translation stage provided fine control of the standing wave and allowed us to maximise interference at the position of the cold ^{87}Rb atoms [43, 51].

The split path and the variable frequencies on the modulators allowed us to realise two CPT fields with orthogonal linear polarisation and inherent phase coherence granted by using a single laser. Whilst we were successful in testing $\text{Lin}\perp\text{Lin}$ CPT with the ^{87}Rb gMOT, the system had some disadvantages which are to be investigated in the future. Using an EOM in only one path meant that there were always extra light components present in the probe beam which were not two-photon resonant. These frequency components consisted of the other sideband, minus f_{HFS} away from resonance, and the EOM carrier component, which was f_3 away from res-

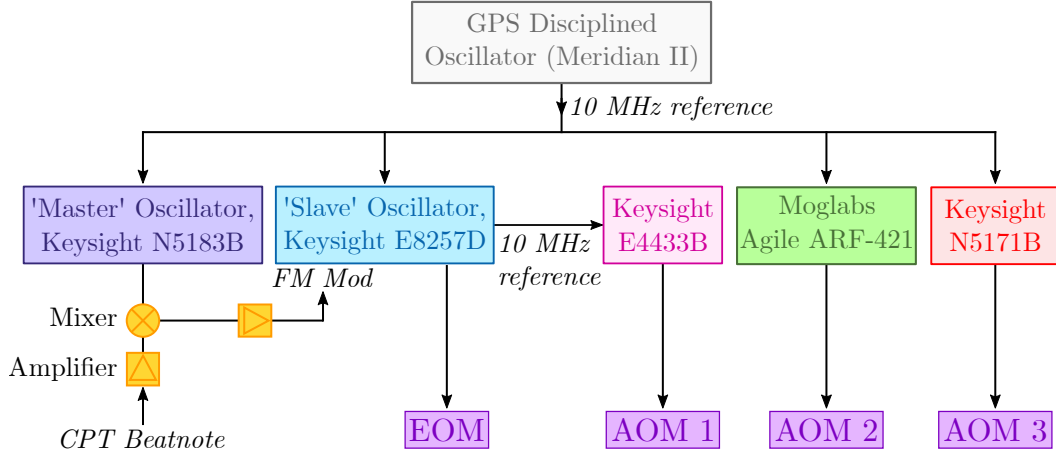


Figure 4.4: A block diagram of the frequency sources used in clock I.

onance. A future investigation into the light-shift contribution of these components will be important for atomic clock operations.

4.2.3 RF Electronics

This section summarises the RF electronics used in the synthesis of the CPT fields. The block diagram in Fig. 4.4 outlines the chain of RF sources that were referenced to a GPS disciplined oscillator (Meridian II by EndRun Technologies) via a 10 MHz signal. The disciplined oscillator is comprised of a GPS receiver that detects signals broadcast by GPS/GNSS satellites to provide stabilisation to a quartz crystal oscillator. The ‘Master’ and ‘Slave’ oscillators refer to two frequency sources in a phase-locked loop (PLL) that was used to suppress extra phase noise at the microwave frequency. The source of the extra noise was believed to be due to fluctuations in the separated paths described in Sec. 4.2.2, causing noise on the relative phase between the CPT frequency components. This sensitivity was a significant

limitation to the measured short-term frequency stability of the apparatus, and this will be discussed in Sec. 5.2. The phase of the CPT beatnote was compared to the phase of the Master oscillator (Keysight N5183B) operating at f_{HFS} , using an RF mixer. The output from the mixer was amplified and used to steer the frequency of the EOM driver, called the Slave oscillator in Fig. 4.4 (Keysight E8257D). An initial characterisation of the PLL was undertaken in reference [90], and will be investigated more thoroughly in the thesis of M. W. Wright. The implementation of the PLL had a direct effect on the detected clock signal and thus the short-term stability of the apparatus, as is shown in Sec. 5.2.

The operating frequencies and part numbers of the synthesisers used in the experiment are summarised in the table below:

Frequency Synthesiser	Operating Frequency	Modulator
Keysight E4433B	203 MHz	AOM ₁
Moglabs rf-421 (DDS)	200 MHz	AOM ₂
Keysight N5171B	206 MHz	AOM ₃
Keysight E8257D	6834 + AOM ₂ MHz	EOM

Table 4.1: A summary of the frequency sources used in the CPT part of the experiment.

The frequencies of AOM₂ and AOM₃ were set to cancel the initial offset on the laser lock from AOM₁ (double-pass) on certain frequency components of the total beam. This would bring two components onto resonance with the ‘CPT₁’ and ‘CPT₂’ transitions, but leave the other components off-resonant with the two-photon transitions.

4.2.4 Clock Sequence

The timing and control sequence for a single Ramsey-CPT experiment run is drawn out in Fig. 4.5. The MOT could be fully loaded in one stage of the sequence by loading for just under 1 s. However, in order to minimise sequence dead time and improve the short-term stability the loading time was reduced to 70 – 80 ms and a reset stage was included at the end of the sequence. This was implemented to re-capture atoms for each cycle of the experiment before the cloud ballistically expands out of the trapping volume [91,92]. If the atoms were still within the capture volume after the Ramsey probing sequence, then they would be re-collected back into the trap. The re-capture efficiency is characterised by balancing the trade-off between experiment cycle time and number of re-collected cold atoms [91,92] and was investigated in reference [90]. The re-capture sequence described in Fig. 4.5 allowed us to realise a total cycle time of $T_c \sim 100$ ms, assuming a dark time of $T = 10$ ms, whilst retaining 70-80 % of the total atom number per cycle [90].

As was discussed in Sec. 3.3.1, the molasses was split into three sections due to the nature of the control electronics. After an optical molasses stage of 6 ms, the trap and repump light is switched off and the trap detuning returns to the MOT detuning. The Ramsey-CPT sequence begins by switching the CPT light on using AOM₃ for 300 μs . This is long enough to ensure atoms are pumped into the dark state, and this was observed by measuring the transmission of this initial pulse.

After pulse 1, the atoms freely precess for a variable time T . During the free evolution, a phase difference is generated between the CPT fields and the atomic oscillation. A second pulse of CPT light acts as a probe for the phase difference

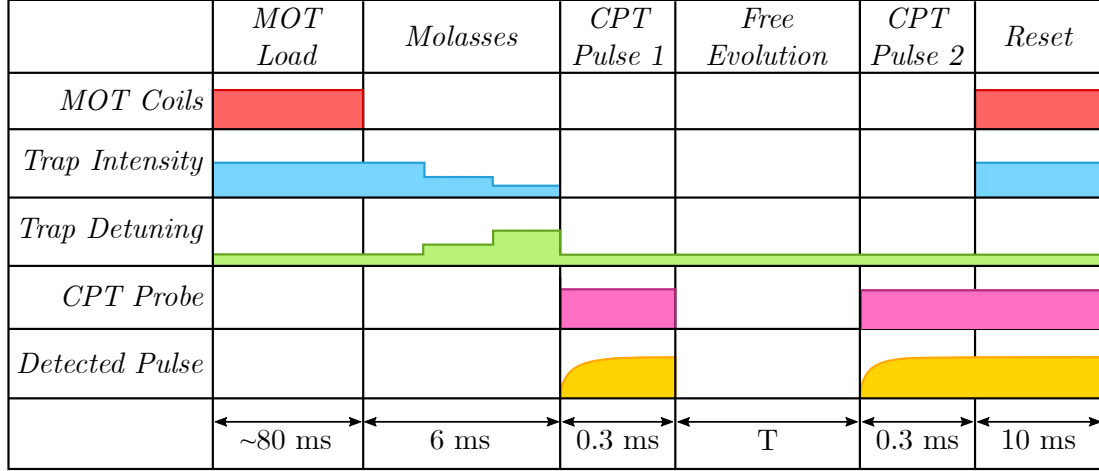


Figure 4.5: An example of the timing sequence for a single run of the Ramsey-CPT probing sequence.

and this is mapped into absorption when the transmission of the beam is detected. Modulated Ramsey-CPT fringes are observed in the laser transmission as the EOM frequency (δ_{2ph}) is varied within the width of the optical CPT feature. Single pulse CPT spectra and Ramsey-CPT fringes measured in the experiment are discussed in the next section.

4.2.5 Detection of CPT Transmission

This section describes the noise-cancellation techniques that were applied to the CPT data obtained from the photodiodes. The detection path is described by the diagram in Fig. 4.6, where the input beam is immediately after the CPT beam shaping optics in Fig. 4.2. The input beam is split using a 90/10 non-polarising beam splitting cube (reflected/transmitted) such that 90% of the optical power is picked off and sent to a ‘reference’ photodiode. The remaining 10% is used to probe

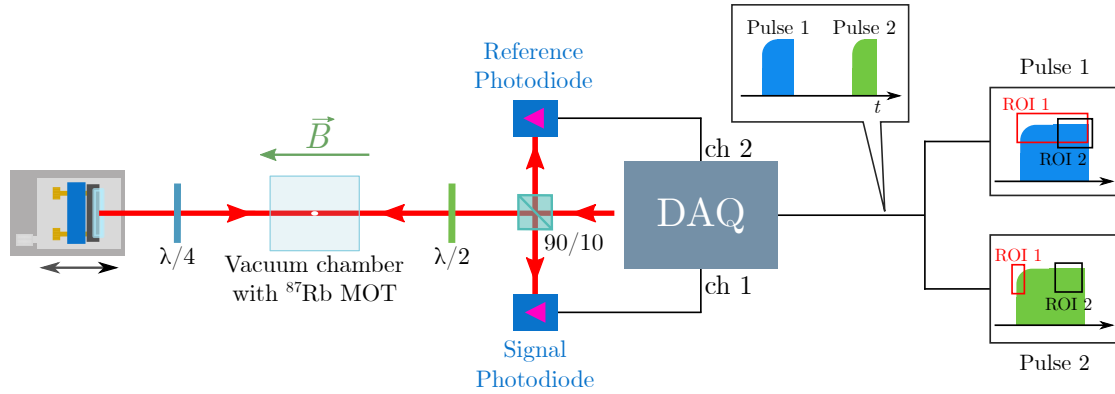


Figure 4.6: A schematic of the detection path. 90% of the input optical power is picked off using a 90/10 non-polarising beam splitter cube (reflected/transmitted) and is measured on a reference photodiode before the remaining 10% probes the atoms in a double-pass configuration. The probe is measured on a signal photodiode after being retro-reflected through the cloud. The photodiode signals are measured on a DAQ and the ratio, ch_1/ch_2 , is taken to cancel some of the common-mode intensity noise. The resulting signal is then split into pulses and regions of integration (ROI).

the cold rubidium atoms in a double-pass configuration [93]. The probe, with the signal, is sent back through the reflected port of the 90/10 cube and onto a ‘signal’ photodiode. A data-acquisition card (DAQ) on the laboratory computer records the photodiode signals on two separate channels as analog inputs. In an initial stage of common-mode intensity noise cancellation, the ratio of the recorded data from the signal photodiode (with atoms) and the recorded data from the reference photodiode (no atoms) is taken, $\approx I_{atoms}/I_{ref}$.

After this normalisation stage, the total data array is comprised of two detected transmission pulses, with respect to time. One for each pulse of the CPT light in the Ramsey-CPT sequence. The first pulse is the dark state pumping pulse, and the second is used as a probing pulse for the Ramsey interferometry sequence. As is

shown in Fig. 4.6, the data array is split into separate arrays for each pulse and then regions of integration (ROIs) are set for each detected transmission pulse. Detection and integration of the first pulse using ROI 2 allowed for the CPT spectrum to be obtained as the two-photon detuning was varied. Characterisation of this data is described in the next section. The second pulse, after the dark time, was used to obtain Ramsey-CPT fringes. As will be described in Sec. 4.3.3, the pulse was split into two ROIs. The Ramsey fringes were obtained by integrating the first ROI of the pulse and by varying the two-photon detuning per cycle of the experiment sequence. The second ROI was then used to cancel common-mode intensity noise on the fringes, as this was a steady state. The size of ROI 1 is characterised in Sec. 4.3.3 using the signal-noise ratio of the detected fringes. The ‘signal’ in this case was defined as the peak-peak height of the fringes, obtained by fitting a cosine function or by measuring the transmission at the top and bottom of the fringe and taking the difference. The noise on different regions of the fringe phase (top, bottom and side) was taken as the standard deviation of a ~ 100 data points at each region. In this case, one data point was one cycle of the experiment.

4.3 Results

In this section, the data obtained from the CPT experiment is sorted into three categories. In the first, absorption imaging was performed using the CPT probe and will be discussed in Sec. 4.3.1. This was found to be a useful diagnostic tool for observing the shape of the MOT, as well as its position relative to the probe beam. In addition, with this imaging technique we were able to measure distinct

CPT absorption features and Ramsey fringes by integrating regions of the obtained image. The latter categories refer to measuring the probe beam transmission on a photodiode, as was described in a previous section (Sec. 4.2.5). In Sec. 4.3.2 the CPT spectrum, measured by integrating the initial CPT pulse in the Ramsey sequence, is discussed. The last section (Sec. 4.3.3), Ramsey fringes are obtained by integrating the second pulse in the sequence.

4.3.1 CPT Absorption Imaging

Absorption imaging is a technique that is often used to measure atom number in different types of traps, or calculate the temperature of an expanding cloud of cold atoms. In this experiment, absorption imaging of the cloud was applied as a diagnostic tool of the cloud position on the probe beam axis, and also to demonstrate CPT and Ramsey-CPT using a different technique. Since the CPT beam was already in a good position for imaging and collimated to a diameter larger than the widest axis of the cloud, it was used for this experiment.

The transmission of the CPT beam will experience a dip as the atoms absorb the light, effectively creating a shadow of the cloud that can be imaged by focussing the beam onto a CCD camera. A diagram of the imaging set-up can be found in Fig. 4.7, where the focussing optics consisted of one lens with a focal length $f = 100$ mm that was placed between the atoms and the CCD in a $2f:2f$ scheme.

A Pixelfly CCD camera was used to take three images, as is also shown in Fig. 4.7; atoms and CPT beam (I_{atoms}), the raw CPT beam (I_{probe}), and a background image

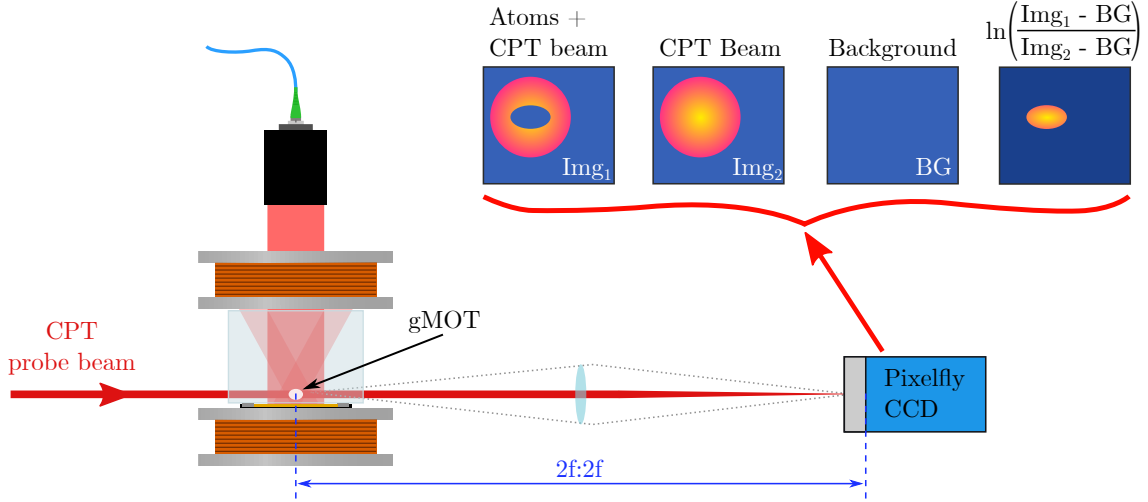


Figure 4.7: The diagram shows a simplified layout of a section of the CPT optical bench, and the set-up for the absorption imaging using the CPT probe beam.

(I_{BG}). The images can then be combined to calculate an optical depth (OD) using:

$$OD = -\ln\left(\frac{I_{\text{probe}} - I_{\text{BG}}}{I_{\text{atoms}} - I_{\text{BG}}}\right). \quad (4.1)$$

An example of the optical depth can be found in Fig. 4.8, where the CPT beam was on resonance ($\delta_{2ph} = 0$) and the atoms were imaged immediately after the molasses. The image in Fig. 4.8 is the average of ten images obtained from ten sequential absorption imaging sequences. The imaging technique is destructive, therefore each run of the sequence required a new MOT to be loaded.

The technique was useful as a diagnostic to check the overlap of the CPT beam with the MOT. As can be seen in Fig. 4.8, the shape of the MOT was elongated on one axis. In order to demonstrate CPT, the OD was summed inside of a spatial region of integration (ROI) that is highlighted by the red box in Fig. 4.8. The OD

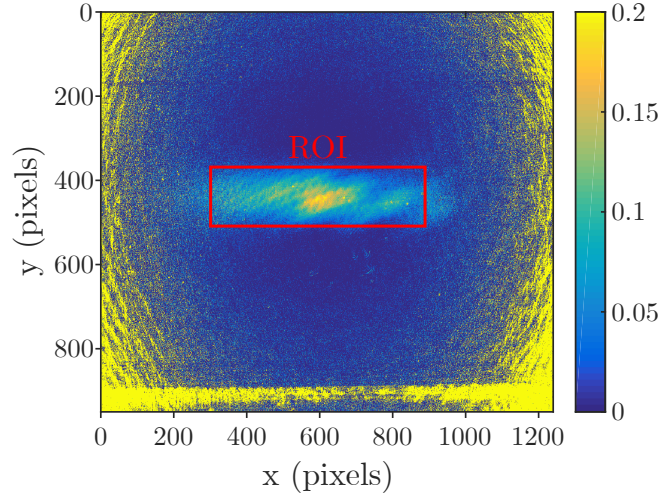


Figure 4.8: Optical depth of the CPT beam with the cloud of cooled rubidium atoms, taken just after the molasses segment of the timing sequence. The x and y axes correspond to the size (in pixels) of the CCD that was used to take the images. The red box highlights a region of integration (ROI) within the image and around the cloud. Summing over the OD values within the bounds of the ROI gave an integrated ROI that was used to observe CPT. The edge of the glass cell can also be observed at the bottom of the OD image.

per pixel with no atoms present was also subtracted from the OD with the atoms present in order to improve the signal, and the average OD per pixel in this region was approximately $0.1 - 0.2$.

By changing the two-photon detuning, it was possible to observe changes in the OD that corresponded to the CPT dark states. The CPT spectra can be observed in the integrated OD in Fig. 4.9 (a), where each data point corresponds to a new run of the absorption imaging sequence and thus there was a new gMOT for every run. The sequence was similar to that described in Sec. 4.2.4, but instead the CCD camera was triggered to take an image (I_{atoms}) during the first pulse of the CPT interrogation. The second and third images were taken after the atoms had left the

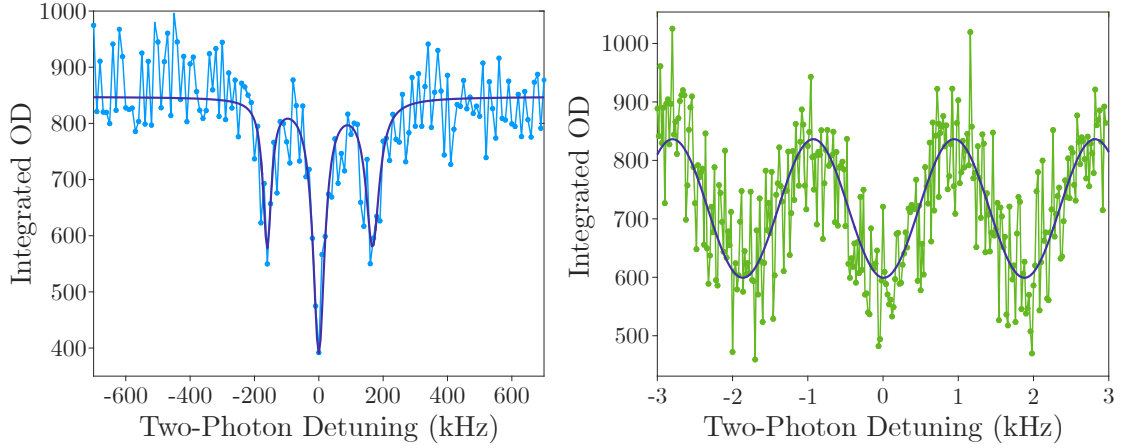


Figure 4.9: (a) Integrated OD inside the ROI as the two-photon detuning was varied, with a background OD/pixel subtracted in addition to the background image taken in the sequence. The dark blue line is a model comprised of three Lorentzians that was fit to the data, as a guide to the eye. (b) Integrated OD with the additional background subtraction that was taken during the probe (second) pulse of the Ramsey sequence. The free evolution was $T = 0.5$ ms, corresponding to a frequency of 2 kHz.

trapping region. A fit of three Lorentzians is applied to the data in Fig. 4.9 (a) to guide the eye.

In a similar measurement shown in Fig. 4.9 (b), we can use the absorption imaging to measure Ramsey fringes in the integrated OD. This time the CCD camera was triggered to take an image during the second pulse of the Ramsey sequence. The free evolution time was set to be relatively short ($T = 0.5$ ms) compared to the Ramsey sequence that was used for clock operation. As can be observed in the plot in Fig. 4.9 (b), the signal-noise ratio (SNR) of the integrated OD was low. This was the main reason for measuring the Ramsey fringes such a short time after the first pulse. The SNR of the acquired integrated OD for both the CPT spectra and the Ramsey fringes could have been improved by taking a number of averages of the

OD signal, such as was applied for the image in Fig. 4.8.

4.3.2 Single-Pulse CPT

The dark-state pumping rate is directly related to the pulse intensity applied to the atoms and thus an optical pumping transient can be observed at the beginning of the first pulse. In Fig. 4.6, it was shown that the first pulse was split into two possible ROIs. ROI 1 includes the whole transmitted pulse and ROI 2 is the last 100 μs . Since this pulse pumps atoms into the dark state, either ROI could be integrated to observe the CPT spectrum. However, it was found that the optimum ROI for measuring the CPT spectrum was the last 100 μs (ROI 2), as the optical pumping had reached an equilibrium point. Integrating the whole pulse (ROI 1) introduced an extra frequency dependence from the initial optical pumping transient.

As covered in Chapter 2, CPT interactions create ‘dark’ resonances, which appear as peaks in the laser transmission as the two-photon detuning is scanned. This is what is referred to as the CPT spectrum. Integrating the steady state transmission of the first pulse as the two-photon detuning is varied allowed the CPT spectrum for the ^{87}Rb D_1 line to be measured. Examples of the transmission are shown in Fig. 4.10. When measuring the optical CPT spectra, we are interested in the steady state of the detected pulse and thus we only apply one stage of common-mode intensity noise cancellation to the data. This was done, as previously described, using the recorded intensity from the reference photodiode before the signal was integrated. In Fig. 4.10 (a) we show the optical CPT signal, which was taken using the $F' = 2$ hyperfine excited level on the ^{87}Rb D_1 line. CPT appears as a strong

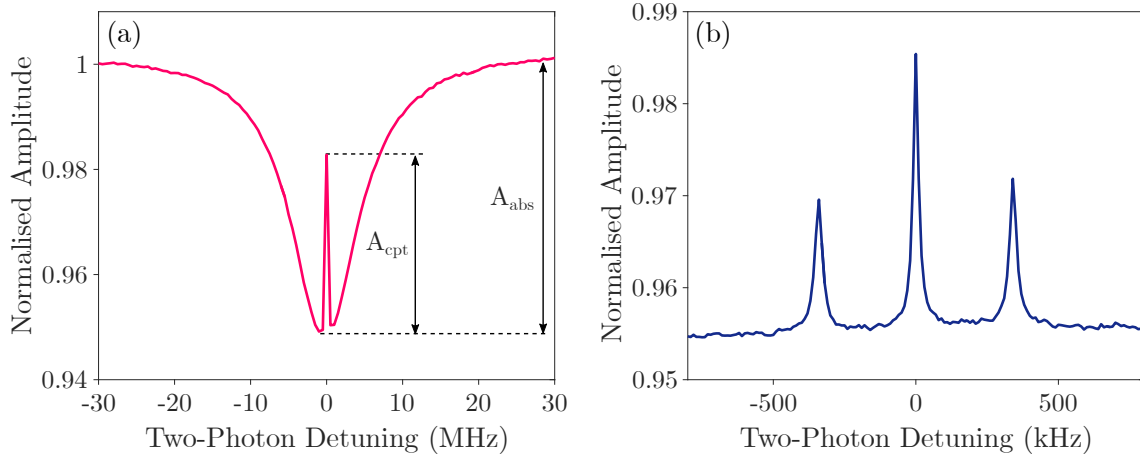


Figure 4.10: Measured CPT spectra taken in the retro-reflected configuration. The data corresponds to integrating the last 100 μs of the first CPT pulse, and is normalised to the off-resonance transmission. The two-photon detuning was varied between: (a) ± 30 MHz to observe the ‘optical CPT line’. The measured absorption and CPT contrast were approximately 5% and 70%. (b) ± 600 kHz, showing the three CPT resonances for the ^{87}Rb D_1 line at a bias magnetic field of ~ 280 mG.

transmission spike in the centre (two-photon detuning, $\delta_{2ph} = 0$) of the absorption dip.

The relative height of the transmission spike at $\delta_{2ph} = 0$ is an indication of how complete the dark state is [29, 45], and the width is related to the dark state lifetime. The amplitude of the transmission spike, A_{cpt} , compared to the full absorption height, A_{abs} , is taken as a measure of the dark state contrast: $C = A_{\text{cpt}}/A_{\text{abs}}$.

As shown in Fig. 4.10 (a), a maximum absorption (in a retro-reflected configuration) of about 5 %, and CPT contrasts of up to 70% with the $F' = 2$ excited state were observed. Each data point in the spectra corresponds to a single run of the experiment sequence (~ 100 ms) in Sec. 4.2.4, and the frequency of the EOM (which sets δ_{2ph}) was varied for each cycle. The other CPT field was kept at one-photon

resonance and not varied.

In Fig. 4.10 (b) all of the CPT resonances that exist within the central CPT transmission spike from Fig. 4.10 (a) are plotted. Increasing the applied magnetic field allows all three transmission features to be spectrally resolved. These are specific to the ^{87}Rb D_1 line, and correspond to the $m_F = 0-0$ CPT state (see Fig. 2.5 in Chapter 2) and the magnetically sensitive $\Delta m_F = \pm 1$ CPT states. The $m_F = 0-0$ is driven at two-photon resonance ($\delta_{2ph} = 0$) and is the central Lorentzian feature in the graph. From Eqn. 2.19, we know that the two-photon detuning required to drive the $\Delta m_F = \pm 1$ varies linearly with magnetic field. Therefore, the position at which the dark resonances are measured (with respect to the central peak) can be adjusted using the bias field, which lifts the degeneracy on the Zeeman sub-levels. The dark resonances occurring at a higher and lower two-photon detuning in Fig. 4.10 (b) correspond to the $\Delta m_F = +1$ and $\Delta m_F = -1$ CPT states, respectively.

The linear sensitivity of the magnetic resonances is a useful tool for estimating the local magnetic field at the position of the atoms. By scanning the two-photon detuning and measuring the steady state transmission of the first pulse, we obtained the CPT spectrum that is plotted in Fig. 4.11 (a) for varying magnetic bias field. The spectrum in Fig. 4.11 (a) show the three CPT resonances for three different bias field magnitudes; 175 mG, 215 mG and 255 mG. The resonance peaks for the $\Delta m_F = \pm 1$ are observed to experience a linear dependence on the bias field, and the two-photon detuning required to drive them is pushed further away from $\delta_{2ph} = 0$.

To vary the bias field, we changed the drive current of a shim coil that generated a homogenous magnetic field parallel to the CPT beam. The coil was part of a set of three Earth-field nulling shim coils that were used during laser cooling of the

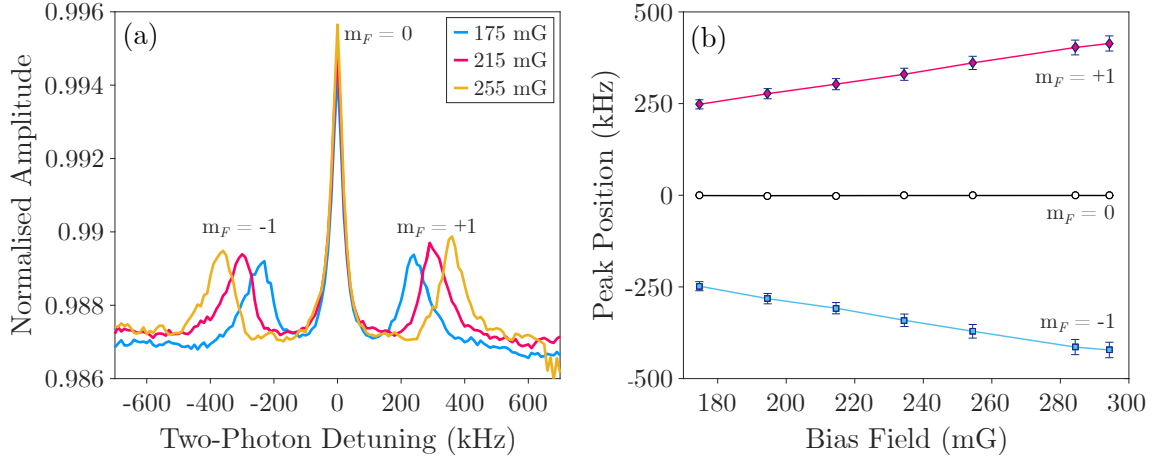


Figure 4.11: (a) Detected transmission of the CPT features as the detuning is scanned, for varying CPT bias field. The magnetic resonances ($\Delta m_F = \pm 1$) were used to measure the bias field at the location of the atoms. (b) Positions (in kHz) of each transmission peak as the bias field is varied, for the central CPT resonance, $m_F = 0-0$, and the magnetically sensitive CPT features, $\Delta m_F = \pm 1$

atoms. The CPT spectrum was obtained for each bias field increment, and was used to measure the linear dependence of the magnetically sensitive CPT states on \vec{B} , and thus estimate the ambient magnetic field at the location of the atoms. Figure 4.11 (b) shows a plot of the peak position, in two-photon detuning (kHz), of each CPT resonance as the bias field was increased from 175 to 295 mG. The peak position, δ_0 , was obtained from a fitting Lorentzian model to each resonance feature.

The plots in in Fig. 4.11 (b) clearly show the linear dependence of the $\Delta m_F = \pm 1$ magnetic resonances. The $m_F = 0 - 0$ does not exhibit a first order gradient as the magnetic field is varied. This is expected as the $m_F = 0$ Zeeman sub-levels should only have a second order dependence on magnetic field (see Sec. 2.4.2). However, in this measurement, the resolution of the central CPT feature is too low to actually measure the quadratic Zeeman shift.

The above calibration for the local magnetic field was used to measure the instability of the magnetic field, and estimate limitations using the second-order Zeeman shift in Sec. 5.2.1.

4.3.3 Ramsey-CPT

In Sec. 2.5.2, Ramsey's interferometry technique was discussed as a means of obtaining the CPT spectrum with high precision. The high precision is mainly due to splitting the interaction with the atomic levels into two pulses separated by a long dark time. The measurement linewidth of the signal is directly related to the time the atoms spend in the dark, $\propto 1/T$. The result is an interference fringe that depends on the phase difference between probe and atoms.

For Ramsey-CPT fringes, the top of the fringe will ideally correspond to maximum transmission, as the laser probe is in phase with the atoms. The bottom of the fringe then corresponds to a maximum in absorption, when the probe is completely out of phase with the atoms. An example fringe, for a free evolution time of $T = 10$ ms, is shown in Fig. 4.12. The graph shows fringe data with (green) and without (dark blue) the second stage of common mode noise cancellation, which will be discussed in the next section.

In this section, the Ramsey technique is physically applied to a $\text{Lin}\perp\text{Lin}$ CPT clock and the results are presented. In order to improve the detected SNR for the fringes, a second stage of common-mode noise cancellation was applied. The first is described at the beginning of this section (see 4.3.2) and makes use of an extra photodiode that only picks up the laser intensity without the atomic signal.

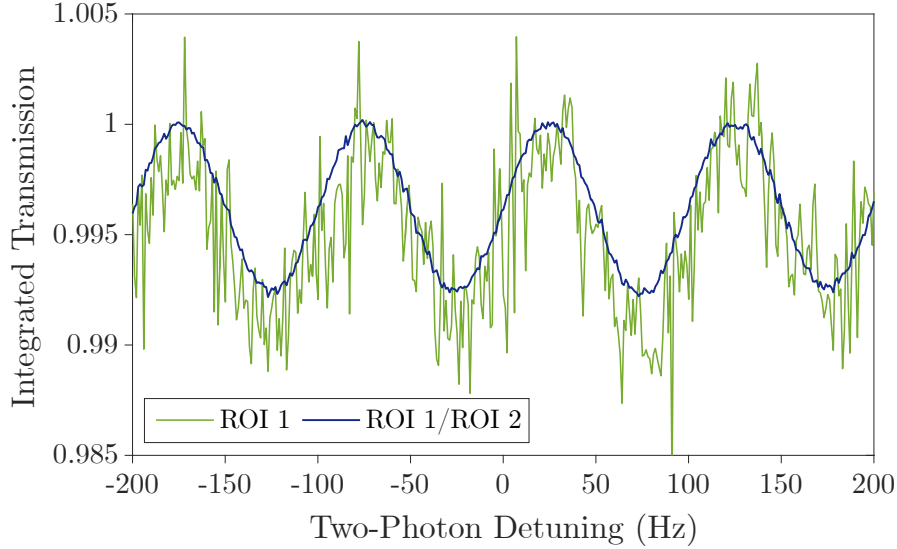


Figure 4.12: Two sets of Ramsey-CPT fringes that show the second stage of common mode noise cancellation, which uses two regions of integration. The ratio of analog input channels has already been taken. The detected second pulse is then split into two ROIs. The integrated transmission for ROI 1 is plotted in green as the two-photon detuning was varied, where each data point is one run of the experiment. The fringe that is plotted in blue is the same set of data, but with the ratio of ROI 1 and ROI 2. The SNR of the data increases from ~ 4 for the data-set without the second ratio, to approximately 50 for the data set with the double-ratio technique applied.

Pulse Dynamics

The nature of the detection pulse in the Ramsey sequence allows a second normalisation stage to be applied to the data. The normalisation had a direct effect on the SNR of the fringes and thus the frequency stability for a short averaging time was also affected. Similar to the first CPT pulse, the detected transmission of the second pulse is split into two regions, ROI 1 and ROI 2. Conversely to the first pulse, both ROIs are used in this noise-cancellation technique for the Ramsey fringes [29, 43, 45, 90].

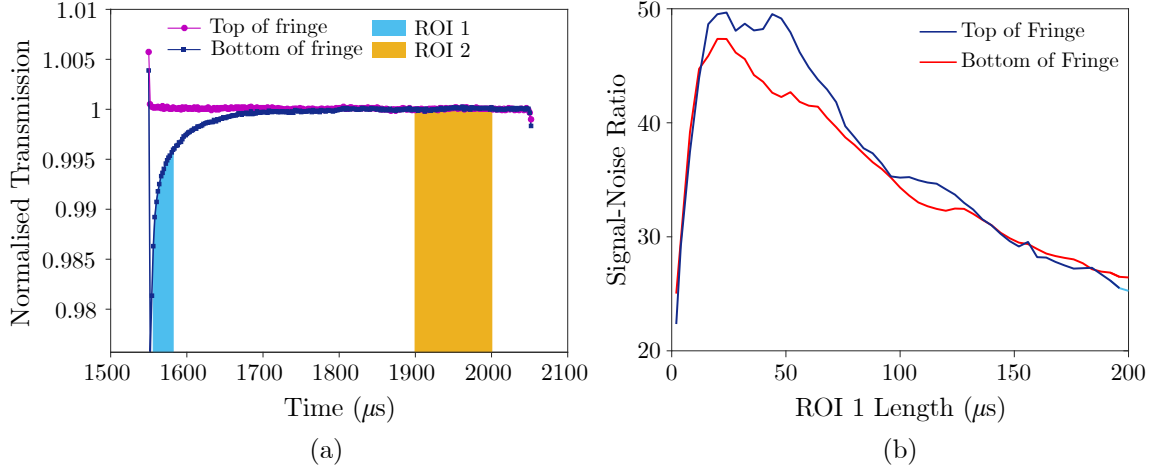


Figure 4.13: (a) Pulse traces of the second pulse taken at two different points in the fringe phase. The top of the fringe is plotted in purple and shows very little transient behaviour. The bottom of a fringe is plotted in blue, and shows an obvious optical pumping transient. The pulses are normalised to the average of the steady state (end region of pulse). The regions of integration (ROI) are highlighted by the coloured regions on the plot. (b): The SNR at the top (blue) and bottom (red) of a Ramsey fringe, as the length of the first region was varied. The total probe intensity for this data was approximately $15 \mu\text{W}$, with an optimal ROI length of $26 \mu\text{s}$.

In a Ramsey-CPT sequence, the interesting data resides in the initial part of the detected transmission of the second pulse. This means that the ‘steady state’ of the detected pulse can be used to normalise the signal without degrading the fringe amplitude. An example of two detected pulses for the top and bottom of the fringe are plotted in Fig. 4.13 (a). Example ROIs are highlighted on the plot using solid blue for ROI 1 and solid yellow for ROI 2. To further cancel common-mode intensity noise, the ratio of ROI 1/ROI 2 was taken [38], after the data had been integrated. The spike at the beginning of both pulses was due to the photodiode response.

A short investigation into the dependence of the fringe SNR on the length of the ROIs was carried out by post-processing the detected pulses in MATLAB. It was

initially found that the length of the second region had little effect on the overall SNR, as long as it was at least $100\ \mu\text{s}$ long. However, the SNR showed a strong dependence on the size of the first ROI. This is shown in Fig. 4.13 (b) for a single optical intensity and for the SNR of the top and bottom regions of the fringe. The length of ROI 2 was kept at $100\ \mu\text{s}$ for this measurement, as the length of ROI 1 was varied from $2 - 200\ \mu\text{s}$.

Since the dark state pumping rate depends on the optical intensity used, the optimal ROI also depends on this intensity. The length of the first region was optimised for best SNR where the signal amplitude was taken to be the peak-peak height of the fringe and the noise was the standard deviation of a large array (~ 100 data points) of a single position on the fringe. The positions we used for this investigation were top and bottom of the detected fringe.

The data shows that most of the important signal from the Ramsey sequence was found to be within the first $26\ \mu\text{s}$ of the detected transmission, for this specific optical pumping power. In our case, the starting point of the region was limited by the response of the photodiodes and low-pass filter that were used to detect the signal. In future, it will be important to extract the full dynamics of the optical pumping into the dark state.

Fringe Profiles

In the Ramsey-CPT scheme, the detection pulse is used to map accumulated phase between the CPT fields and the hyperfine resonance frequency of the atoms into an absorption signal. The detected signal is a modulation of the CPT resonance shown in Fig. 4.10 in Sec. 4.3.2, where the fringes directly depend on the free evolution

time, T .

The double-ratio technique [38] was effective at significantly improving the SNR of the detected fringes, and the effect on the CPT fringe envelope is summarised in Fig. 4.14. Figure 4.14 contains four plots which were created from the same set of data. The free evolution time was $T = 1$ ms and each data point corresponds to a single experimental run. In Fig. 4.14 (a), the raw integrated transmission (ROI 1 only) from the signal photodiode is plotted against two-photon detuning.

In Fig. 4.14 (b), the ratio of the recorded signals from the signal and reference photodiodes has been taken (I_{atoms}/I_{ref}), and then the transmission has been integrated over ROI 1. The plots in Fig. 4.14 (a) and Fig. 4.14 (b) show that some of the slowly varying intensity noise was cancelled by normalising the signal against a reference photodiode signal, and this is observed at the bottom of the fringe.

The corresponding integrated transmission of ROI 2 is then plotted in Fig. 4.14 (c). This exhibits a Lorentzian profile very similar to the steady state of the first CPT pulse and the fringes have (mostly) washed out. The small fringes observed at δ_{2ph} close to zero were used as an indication that the second region should be moved closer to the end of the pulse.

Finally, Fig. 4.14 (d) shows the result of the second stage of normalisation. This is the ratio of ROI 1 and ROI 2, and therefore is essentially also the ratio of the plots in (b) and (c). The Lorentzian profile from Fig. 4.14 (b) is applied to the data in Fig. 4.14 (a), resulting in the shape of the envelope in Fig. 4.14 (c).

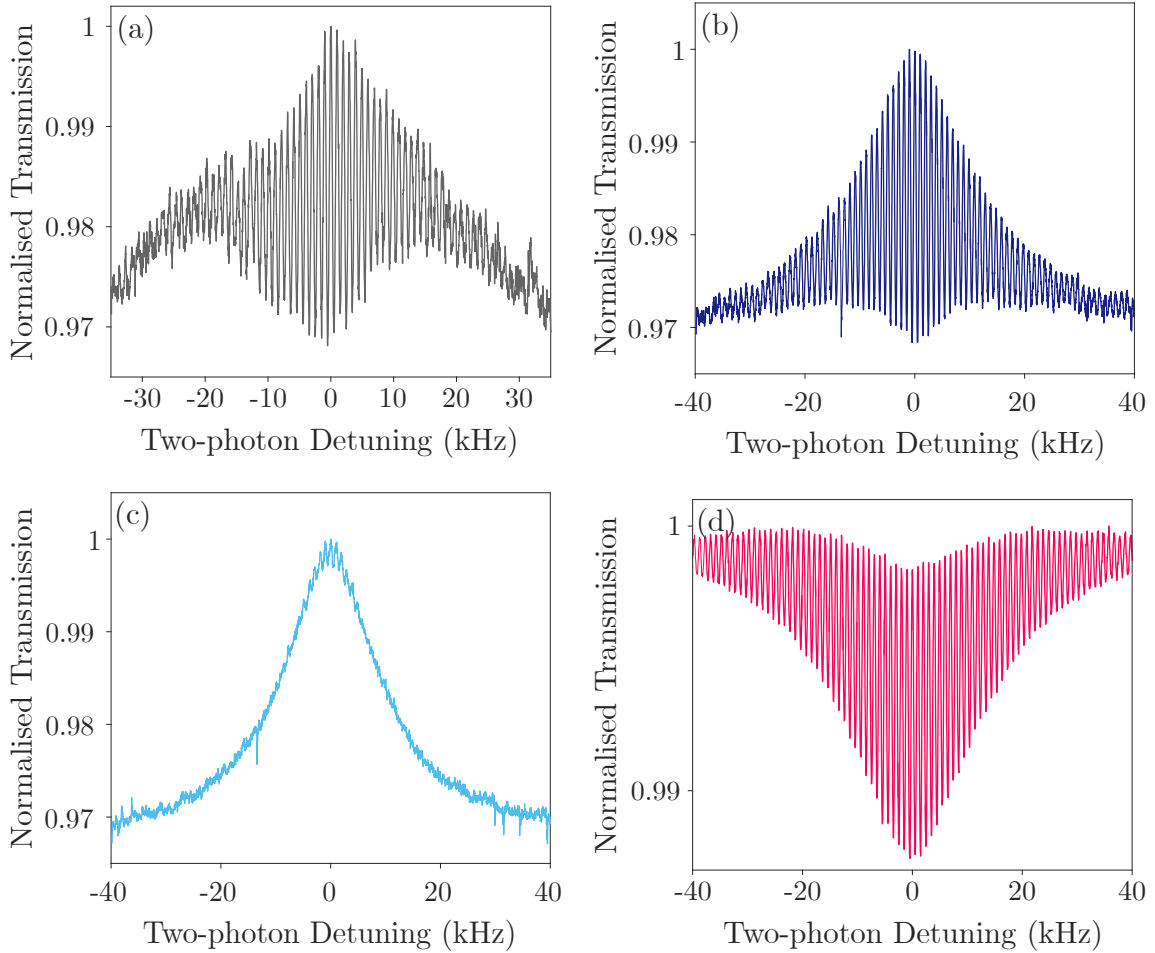


Figure 4.14: (a) Integrated transmission of the raw recorded signal photodiode as the two-photon detuning was varied. (b) Integrated transmission at the start of the probe pulse, ROI 1, after the ratio of the photodiode signals was taken. For this dataset, the optimised ROI 1 was $26 \mu s$ long. (c) Integrated transmission of the steady state of pulse 2, or ROI 2. The fringes observed at δ_{2ph} close to zero are an indication that ROI 2 should have been closer to the end of the pulse. (d) The Ramsey fringe pattern with both stages of normalisation applied. The first is the ratio of signal/reference photodiodes and the second is the ratio of the integrated regions, ROI 1/ROI 2.

Experiment: Dark State Interference

The main motivation behind adopting a high-contrast CPT method, such as Lin \perp Lin, is to exploit constructive interference between the multiple dark states that are generated when exciting a double- Λ structure. As was discussed in Chapter 2, it is possible to simultaneously drive three dark states on the D₁ line of ⁸⁷Rb using Lin \perp Lin CPT. The first is a common dark state, generated between the $|F = 1, m_F = 0\rangle$ and $|F = 2, m_F = 0\rangle$ states, referred to as the $m_F = 0-0$ dark state. Since this is formed between Zeeman sub-levels with $m_F = 0$, the magnetic sensitivity is of the second order (see Eqn. 2.31 in Sec. 2.4.2). The latter two dark states are not formed between common m_F levels, but are instead superpositions across $\Delta m_F = 2$. The dark resonances form between $|F = 1, m_F = \pm 1\rangle$ and $|F = 2, m_F = \mp 1\rangle$ states, as was discussed in Sec. 2.4 for Lin||Lin CPT. This means these resonances will exhibit a linear sensitivity to magnetic fields (see Sec. 2.4.2). The $\Delta m_F = 2$ resonances occur at the same two-photon detuning as the $m_F = 0-0$ resonance, but cannot be spectrally resolved using single-pulse CPT under a weak magnetic field.

This section describes an experiment that observes this dark state interference as a function of excited level and varying magnetic bias field. This bias field is used to set the quantisation axis for CPT. As was touched on briefly in Chapter 2, occurrence of all three dark resonances has a strong dependence on excited level [55]. The $m_F = 0-0$ resonance is present when driving Lin \perp Lin CPT via both the $F' = 1$ and $F' = 2$. However, the $\Delta m_F = 2$ resonances will be suppressed when driven via the $F' = 2$ due to the presence of the extra Zeeman sub-levels in this manifold. Interference of these multiple dark states manifests itself as a modulation of the

Ramsey fringe amplitude as the magnetic bias field is varied, such that one full cycle of the interference pattern corresponds to a change in magnetic field of $\Delta B = 1/TZ$ where T is the Ramsey dark time and Z is the residual linear Zeeman shift of the $\Delta m_F = 2$ resonances [43, 55, 94]. As the field increases, the patterns created by the $\Delta m_F = 2$ will move in opposite directions relative to the fringe pattern generated by the $m_F = 0 - 0$ resonance [55, 94]. Varying the field changes the overlap of the three fringe patterns generated by each dark state, causing destructive or constructive interference.

For this experiment, the Ramsey sequence outlined in Sec. 4.2.4 was performed

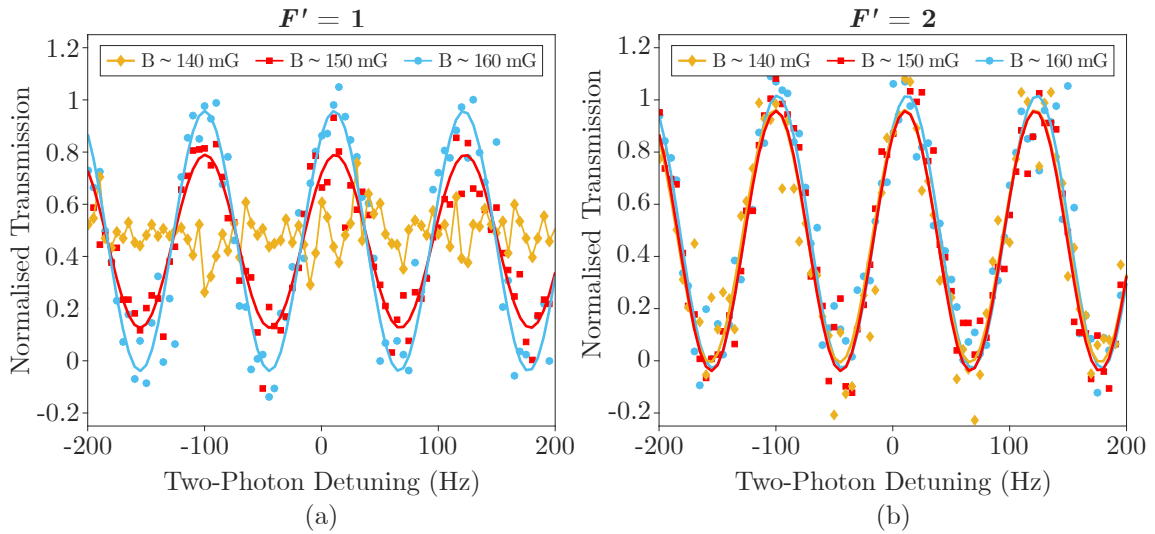


Figure 4.15: The dark state interference effect observed using Ramsey fringes at a free evolution time of $T = 9$ ms. Three sets of fringes are plotted in each figure, for magnetic bias fields at approximately 140 mG, 150 mG and 160 mG. The excited state was set to $F' = 1$ for (a) and $F' = 2$ for (b), allowing for a comparison between the two. The data points are supplemented with a sinusoidal fit (solid lines) to guide the eye, for all sets of data except for the 140 mG in (a), where the fringes have completely washed out. The fringe amplitude has been normalised to the average fringe amplitude obtained with $F' = 2$.

with a longer loading time, since this experiment was carried out before atom recapture was implemented. The free evolution time was set to be $T = 9$ ms. In Fig. 4.15, two sets of detected fringes are plotted for three different bias fields: ~ 140 mG, 150 mG and 160 mG. In Fig. 4.15 (a), the excited level is the $F' = 1$ and in Fig. 4.15 (b) the excited level is the $F' = 2$.

This dataset was also taken prior to the installation of the PLL, which accounts for the drop in detected signal-noise ratio compared to the previously shown fringes. For the $F' = 1$ data [Fig. 4.15 (a)] and for particular values of the magnetic field, the fringe amplitude reduces to the point where the sinusoidal pattern has disappeared below the noise floor. In the $F' = 2$ dataset, the fringe amplitude sees little to no effect when the ambient field is varied. The effect is observed in more detail by the plot in Fig. 4.16, where the variation in fringe amplitude is plotted over a wider range of bias fields for both the $F' = 1$ and $F' = 2$ excited states. In this figure, a full oscillation of the fringe amplitude for the $F' = 1$ is observed as the field varies by approximately 40 mG. This is attributed to the linearly sensitive $\Delta m_F = 2$ resonances interfering with the $m_F = 0-0$ resonance, and is in good agreement with $\Delta B = 1/TZ \approx 40$ mG for ^{87}Rb and $T = 9$ ms. Similarly, the fringe amplitude remains mostly constant for the data taken with $F' = 2$, leading us to believe that the $\Delta m_F = 2$ resonances are suppressed, leaving the $m_F = 0-0$.

With this set of data, it is also possible to speculate on the relative populations of each dark state. The fact that the fringe pattern is nearly extinguished infers that approximately half of the population could be in the $m_F = 0-0$ dark state. However, the signal-to-noise ratio (SNR) on the obtained fringes is low, leading to poor fitting of the fringe patterns with lower amplitude. This experiment would

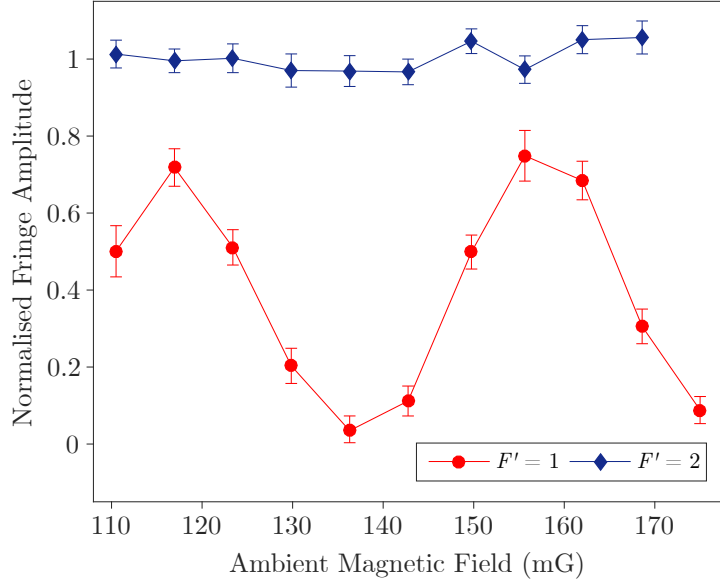


Figure 4.16: The measured peak-peak fringe amplitude of the $T = 9$ ms Ramsey fringes for the $F' = 1$ (red circles) and $F' = 2$ (blue diamonds) excited states, as a function of magnetic bias field. The amplitudes were obtained from a sinusoidal fit to the fringe data, and are normalised to the average fringe amplitude for the $F' = 2$. The magnetic bias field was calculated using the magnetic CPT resonances, similar to the experiment in Sec. 4.3.2.

benefit from being re-visited in the future, now that the fringe SNR has been vastly improved, as it is expected that there might be residual oscillations due to non-completete destruction of the $\Delta m_F = 2$ coherences [94]. The fringe amplitude was also observed to be slightly higher for the $F' = 2$, supporting the decision to utilise this excited state for $\text{Lin}\perp\text{Lin}$ CPT on the ^{87}Rb D_1 line.

4.4 Chapter 4 Summary

The intention of this chapter was to provide a technical description of the CPT apparatus and present some of the key characterisation data. Section 4.2 included details on spectroscopy of the D₁ line in ⁸⁷Rb, the optical bench and RF electronics required to generate the Lin \perp Lin CPT fields, the Ramsey-CPT control sequence and finally the detection method for the Ramsey fringes.

In addition, the main results for characterising the system were presented in three categories: absorption imaging with the CPT beam, single-pulse CPT (for obtaining the CPT spectrum) and Ramsey-CPT (for obtaining the clock signal). In each, the relevant data is shown and discussed. The absorption imaging, described in Sec. 4.3.1, was not only useful as a diagnostic tool, but was also used for detection of the CPT spectrum and Ramsey fringes. This is an exciting avenue that could be investigated in the future. Section 4.3.2 described detection of single-pulse CPT, where the CPT contrast was measured and the ambient magnetic field at the location of the atoms was calibrated using the magnetic CPT resonances. Finally, characteristic Ramsey fringe data is presented in Sec. 4.3.3 to show the improvement from cancelling common-mode intensity noise as well as investigate an interference effect between dark states.

Chapter 5

Frequency Stability

The stability of an oscillator is derived from the precision, or the repeatability of the frequency measurement. Stability is defined as how well the oscillator can keep to a certain frequency over a set amount of time. The Allan deviation, or two-sample deviation, is commonly used to measure the frequency stability of oscillators, frequency references and atomic clocks. The method was developed in the late 1960s and is a standard method of statistically analysing frequency fluctuations and drifts of an oscillator over time [95,96].

In this chapter, the Allan deviation is introduced as the method that was used to quantify the performance of the cold-atom CPT apparatus as an unlocked atomic clock. The method that was used to obtain the fractional frequency deviations of the CPT-Ramsey fringes is described, and the Allan deviation of the system is presented. As an initial measurement of potential limits to the frequency stability, the magnetic CPT resonances are used to estimate the limit caused by magnetic field fluctuations.

5.1 Introduction to Allan Deviation

The operation of an atomic clock requires a measurable response from the atoms, such that the frequency of the local oscillator can be synchronised with the atomic resonance frequency. Instability in the detected signal will be converted into instabilities on the measured frequency. A real signal, such as atomic absorption, will have a certain amount of noise imposed on it that can depend on several sources. For example, these could be electronic noise from the detection, thermal drifts or vibrations. Some sources of noise can be significantly reduced. However, some fundamental sources, such as shot noise, are more difficult to eliminate. Shot noise arises from the quantisation of energy into photons and the intrinsic fluctuations of the photons arriving at a detector.

The Allan deviation can be calculated with respect to a sample time, or averaging time, τ . The short-term stability ($\tau < 100$ s) of many atomic clocks is characterised by white frequency noise wherein the Allan deviation decreases as $\tau^{-1/2}$. This can be estimated using the following simplified relation:

$$\sigma_y(\tau) \sim \frac{\Delta\nu}{\nu_0} \sqrt{\frac{T_{cycle}}{\tau}} \frac{1}{SNR}, \quad (5.1)$$

where $\Delta\nu$ is the measurement linewidth of the central frequency ν_0 , τ is the averaging time and SNR is signal-noise ratio. T_{cycle} is the cycle time of the frequency measurement, where a single measurement compares the frequency of the the LO and the atoms. The cycle times arises from the mutiple measurements that are required for frequency syntonisation or to build up the statistics of the frequency

difference. This equation can also be used to estimate theoretical limits to the short-term stability. For example, at the quantum projection noise (QPN) limit of the CPT clock experiment described in this thesis, SNR becomes \sqrt{N} . With an average atom number of $N = 10^7$, cycle time of $T_{cycle} = 100$ ms and linewidth of $\Delta\nu = 50$ Hz (for $T = 10$ ms), the projected short-term stability ($\tau = 1$ s) would be on the order of $10^{-13}/\sqrt{\tau}$.

In practice, the Allan deviation is calculated from an array of fractional frequency fluctuations, such as those plotted in Fig. 5.1 (a), that are defined as:

$$y(t) = \frac{f_{atoms} - f_{LO}}{f_0} = \frac{\Delta f}{f_0}. \quad (5.2)$$

where f_{atoms} may be shifted from the resonance frequency, f_0 due to systematic effects. The fractional frequency is then the difference between the measured frequency, f_{atoms} , and the local oscillator frequency, f_{LO} , divided by the resonance frequency. Therefore, it is important in practice to use an LO that has better stability, such that the measurement is not limited by the LO. The stability is calculated by computing the Allan deviation as function of the averaging time τ . The data is split into segments of τ , the averaging window, which is then gradually increased. The Allan deviation is calculated for each non-overlapping segment using the following [2, 96]:

$$\sigma_y = \sqrt{\sum_{k=1}^i ((y_{k+1}(\tau) - y_k(\tau))^2)}. \quad (5.3)$$

Here, y_k refers to the segments of the data from Fig. 5.1. The Allan deviation, σ_y , is

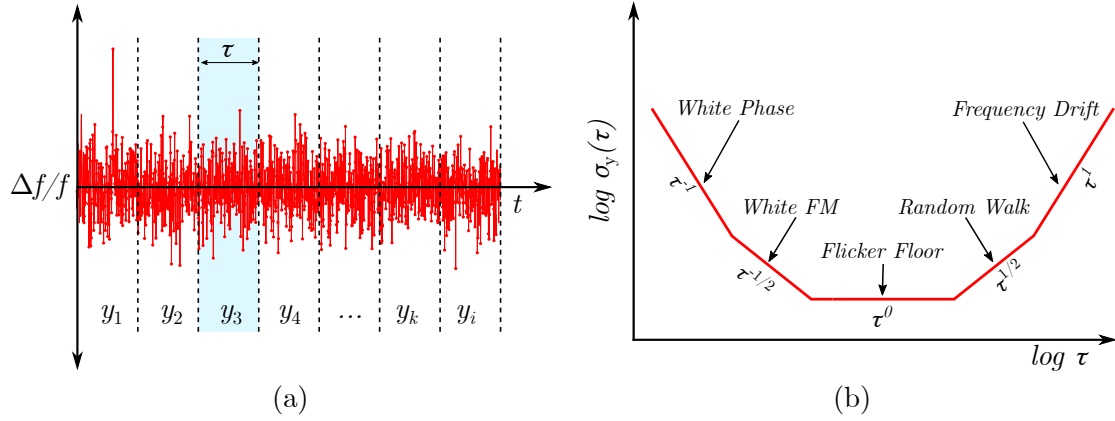


Figure 5.1: (a) Fractional frequency deviations over time, that are split into segments, $y_k(t)$, of time τ . (b) Noise behaviour of Allan deviation data as the averaging time, τ , increases. Different sources, and their respective apparent power laws, are drawn for the standard Allan deviation [95, 96].

plotted against the averaging time, τ , to obtain a plot that would be similar to the graph in Fig. 5.1 (b). Over time, certain types of noise will average out allowing for other noise sources to become apparent. The noise source can be determined from the apparent power law of σ_y versus τ , for the standard Allan deviation. Several different sources are highlighted in Fig. 5.1 (b), but it should be noted that not all of the processes in Fig. 5.1 (b) are present in, for example, a caesium fountain where most of the measured noise can be classified white FM noise.

5.2 Measuring Frequency Stability

In order to quantify the performance of the first generation CPT clock, an Allan deviation was used to compare the frequency of the local oscillator (see Fig. 4.4 in Sec. 4.2.3) with the atomic resonance frequency. Using quantum projection noise

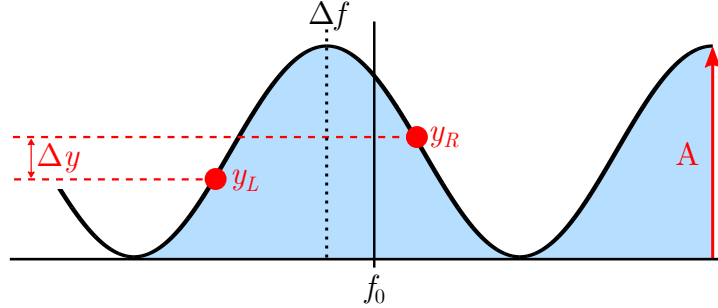


Figure 5.2: A diagram to illustrate the frequency at the centre of the fringe, which is calculated using the peak-peak amplitude (A) and the amplitude at the sides of the fringe where $f = \delta_{2ph}/4$, denoted by $y_{R,L}$.

(QPN) as a theoretical limit, the signal-noise ratio (SNR) in Eqn. 5.1 is replaced with \sqrt{N} (N = atom number) to indicate a short-term stability on the order of $10^{-13} / \sqrt{\tau}$. The fractional frequency stability was estimated using the measured Ramsey-CPT fringes and the double-ratio normalisation technique outlined in Sec. 4.3.3 was applied to the data. The data to measure the frequency stability was acquired using a Ramsey-CPT sequence, similar to that outlined in Sec. 4.2.4, with a free evolution time that was set to $T = 10$ ms.

The normalised transmission at the side of the Ramsey fringe was used to obtain the central position of the measured Ramsey fringe, as is shown in Fig. 5.2. The two-photon detuning was shifted by $\delta_{2ph}/4$ up and down sequentially in repeated runs of the experiment sequence, in order to obtain shot-shot changes in the signal amplitude that correspond to $\Delta y = y_R - y_L$. The amplitude, $y_{R,L}$, at $\pm\delta_{2ph}/4$ is related to the peak-peak amplitude of the fringe, A , the measured frequency

difference between the atoms and the LO, Δf , and the Ramsey time, T , by:

$$y_{R,L} \approx y_0 \pm \frac{A}{2} \sin(2\pi\Delta f T). \quad (5.4)$$

Assuming that $\Delta f \ll 1/T$, then Δy can be approximated to $\Delta y \approx 2\pi\Delta f AT$. The model in Eqn. 5.4 can be re-arranged to calculate the frequency deviations:

$$\Delta f = \frac{\Delta y}{2\pi AT}. \quad (5.5)$$

The calculated Δf are used to calculate the fractional frequency, $\Delta f/f_0$, where f_0 is the groundstate hyperfine splitting frequency in ^{87}Rb . The frequency stability is then measured by calculating the Allan deviation.

Using the sides of the Ramsey fringe allows us to obtain a direction as well as the magnitude of the deviations between the atoms and the LO. A comparison of the measured frequency stability of the cold-atom CPT apparatus is plotted in Fig.5.3 for three different configurations. For our measurements of the frequency stability, the frequency deviations were not used to stabilise the LO to the atoms. The first curve (pink squares) shows one of the initial measurements of the stability, before the phase-locked loop (PLL) described in Sec. 4.2.3 was installed. The second (red circles) was measured with the PLL engaged and showed a factor of two improvement on the stability [90]. In these two Allan deviation curves, the Ramsey-CPT was measured in a ‘single-pass’ configuration where the CPT is not retro-reflected through the cloud.

The last curve (blue diamonds) was taken most recently, with the experiment in

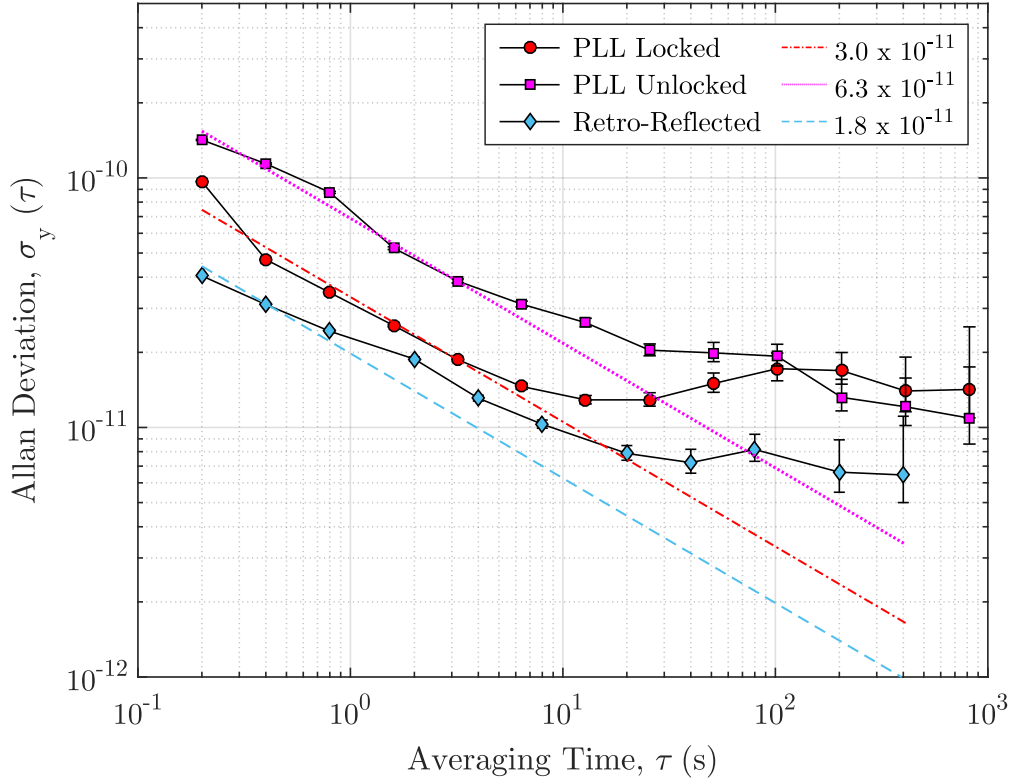


Figure 5.3: Allan deviation curves from the first generation clock experiment in three configurations. The $1/\sqrt{\tau}$ coefficients are labelled in the legend, corresponding to the dashed, dotted and dot-dashed lines.

a slightly different configuration. In this case, the Ramsey-CPT was measured with the probe beam in a double-pass configuration that was implemented to minimise probe-induced Doppler shifts. Retro-reflecting the beam increased the measured absorption by approximately a factor of two, and consequently the fringe amplitude and signal-noise ratio (SNR) were also improved, but not by the same factor. Furthermore, this data was taken using homebuilt photodiodes that reduced the detection noise floor. This floor was measured with the probe beam on, but with no

atoms present.

The short-term stability was measured using a linear $1/\sqrt{\tau}$ fit to the first six data points for the ‘PLL locked’ and ‘Unlocked’ data. These are also plotted beside the corresponding data in Fig. 5.3, showing the distinct improvement with the PLL engaged. For the ‘retro-reflected’ dataset, the fit was applied to the first three data points only, due to a poor fit which tells us that the noise limiting this measurement was not white FM noise.

Implementing the retro-reflected path and upgraded photodiodes improved the short-term stability of the CPT apparatus. The stability flattened out after ten seconds of averaging, highlighting a limit that is still under investigation. One of the suspected causes was magnetic noise, as the system was (at the time of writing) unshielded and the bias field that was applied to detect CPT was relatively high. The estimated contribution of magnetic noise to the frequency stability is investigated in the next section.

5.2.1 Magnetic Field Stability

This section describes an experiment where the contribution of magnetic field noise to the frequency stability was measured. The frequency stability was directly measured using the CPT features (see Sec. 4.3.2) which have a Lorentzian lineshape described by:

$$y(\delta) = \frac{A}{(\delta - \delta_0)^2 + \frac{\Gamma^2}{4}}, \quad (5.6)$$

where A is the amplitude, δ_0 is the frequency at which $y(\delta)$ is maximised and Γ is the full-width at half maximum (FWHM). A similar method to the previous section was applied in order to measure the stability using the CPT features, where the slope of the transmission peak was used to determine the fluctuations from the amplitude. The two-photon detuning was set to shift the frequency $\pm\Gamma/2$ away from the centre of the CPT resonance to obtain the amplitude fluctuations:

$$y_{R,L} = \frac{A}{(\delta \pm \Gamma/2)^2 + \frac{\Gamma^2}{4}}. \quad (5.7a)$$

Before the stability measurement was taken, the amplitude of the CPT resonances were obtained from a Lorentzian fit by scanning the local oscillator frequency over each resonance feature. The results from the fit were then used as a guide to set the local oscillator frequency to ‘hop’ on either side of the resonance feature. The fractional frequency stability of the CPT apparatus was then measured using each of the three CPT resonances for the D₁ line of ⁸⁷Rb. The measured Allan deviation curves for the three CPT resonances are shown in Fig.5.4 with corresponding $1/\sqrt{\tau}$ lines.

The magnetic resonances, $m_F = +1$ (red diamonds) and $m_F = -1$ (blue squares), exhibit a higher instability which is due to a few factors. The amplitude of the $m_F = \pm 1$ CPT features is lower because of the double- Λ scheme that was used, which means that most of the population was pumped into the $m_F = 0-0$ dark state. The magnetic CPT features also have a slightly large linewidth (FWHM) than the central CPT resonance, due to the linear sensitivity of the $m_F = \pm 1$ levels to magnetic field. The sensitivity is also observed on the Allan deviation curves

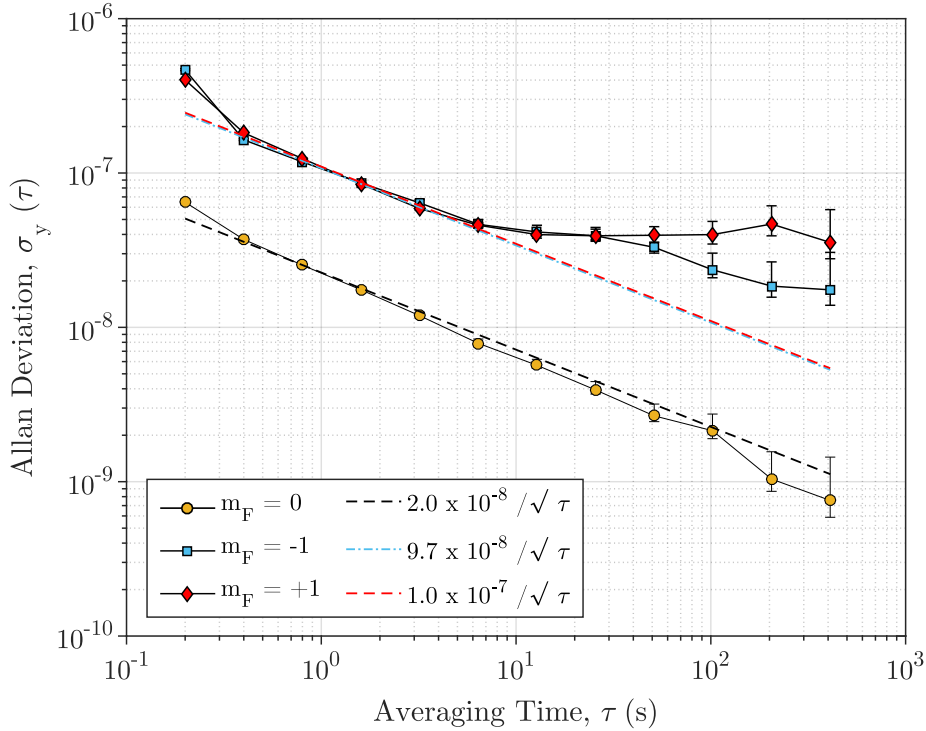


Figure 5.4: Measured Allan deviation curves for the three CPT resonances: the $m_F = 0$ in yellow circles, $m_F = +1$ in blue squares and $m_F = -1$ in red diamonds. The $m_F = 0$ corresponds to the resonance feature at zero two-photon detuning from Fig. 4.10 in Sec. 4.3.2 and the $m_F = \pm 1$ are the magnetic CPT resonances. This data was taken for a magnetic bias field of 280 mG.

after $\tau = 10$ s, where the stability appears to level out.

The main CPT feature, $m_F = 0$, is observed to have a stability which is a factor of 5 lower, and follows a $1/\sqrt{\tau}$ dependence strongly. It is estimated that the frequency stability of this feature would continue to average down as white noise until it reached the same stability limits measured using the $T = 10$ ms Ramsey-CPT fringes (5.3).

Estimating Second Order Limits

In this section, a possible limit to the measured frequency stability of the CPT apparatus is investigated. Using the calibration from Sec. 4.3.2, the ambient magnetic field at the position of the atoms, B , was calculated. The fluctuations of the magnetic field, ΔB , were calculated using the measured frequency deviations of one of the magnetic CPT features and the first-order Zeeman shift experienced by the ground-state sub-levels. For each sub-level this is 700 kHz/G, giving a total first order shift of 1.4 MHz/G [40].

Figure 5.5 shows Allan deviation curves measured at two different bias fields; $B \sim 280$ mG (purple diamonds) and $B \sim 130$ mG (blue circles). This data was taken using the Ramsey fringes with the experiment sequence operating with a free-evolution time of $T = 10$ ms. The quadratic Zeeman shift for the $m_F = 0$ sub-level is 575 Hz/G² [40]. This was used to re-scale the ΔB data from the magnetic CPT resonance, taking into account the ambient magnetic field.

The two additional plots that are shown in Fig. 5.5 show the estimated limits to the stability from the magnetic field. For these curves, the data from the magnetic CPT resonance, $m_F = +1$, was re-scaled using the first and second order Zeeman shift and ambient magnetic fields of $B \sim 280$ mG (red triangles) and $B \sim 130$ mG (black triangles).

From this graph, it is clear that another factor was limiting the stability as the estimated magnetic field instability for the lower magnetic field (black) exhibits a lower instability that is not matched by the data taken with the Ramsey-CPT sequence (blue circles).

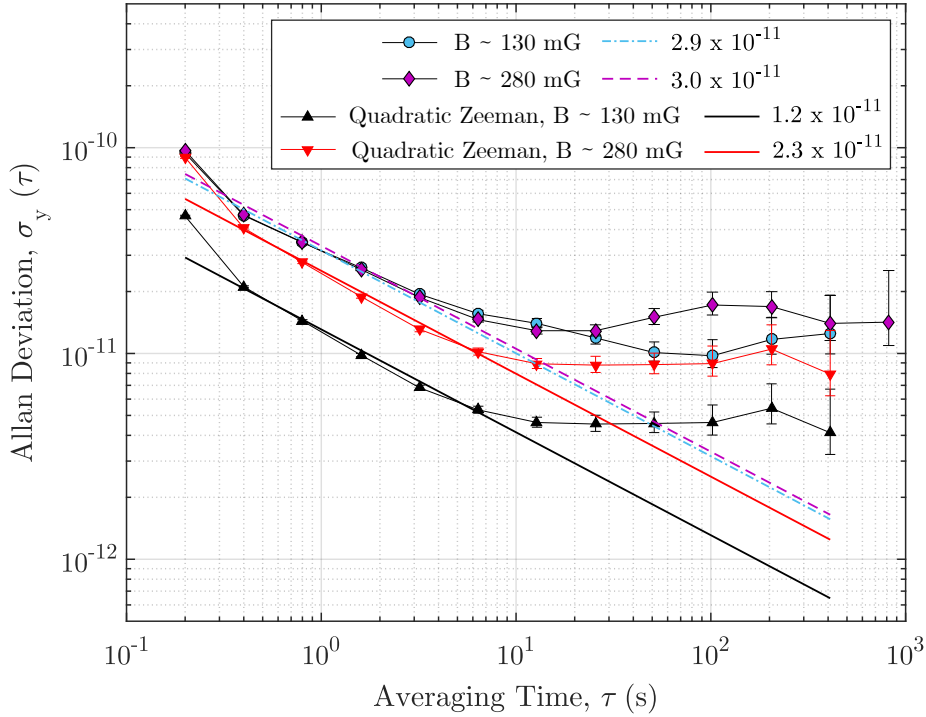


Figure 5.5: Allan deviation curves taken using the Ramsey-CPT sequence at two different magnetic bias fields; $B \sim 130$ mG (blue circles) and $B \sim 280$ mG (purple diamonds). The dashed lines are the $1/\sqrt{\tau}$ lines. Additional Allan deviation curves are plotted for the estimates of the quadratic Zeeman limit at the two magnetic bias fields, $B \sim 130$ mG (black) and $B \sim 280$ mG (red).

Although the magnetic field was not the limiting factor for this measurement, it is apparent that it is an approaching limit. Therefore, in the current experimental apparatus a magnetic shield has been implemented around the vacuum cell. The effects of which will be discussed in future theses. As for other possible causes for the stability floor, there are other avenues that could be investigated. This includes the RF electronics, or light shifts from the probe or trap light.

5.3 Chapter 5 Summary

In this chapter, the performance of the cold-atom Lin \perp Lin CPT clock was presented in a study of the frequency stability. The Allan deviation was introduced in Sec. 5.1 as the technique used to measure the frequency stability of the apparatus as an unlocked atomic clock. The performance itself is presented in Sec. 5.2, along with an investigation of the limitations to the stability caused by magnetic field fluctuations.

Chapter 6

Conclusions

6.1 Summary

6.1.1 Grating-chips for Laser-Cooling

The development of laser cooling was an important milestone for many quantum sensors. Reducing the complexity of laser-cooling apparatus allows more applications to benefit from cold atoms, and opens up exciting possibilities for the future of precision measurements.

The investigation that was undertaken for this thesis was the development of an atomic clock that was based on grating chip technology for laser cooling. The grating chips allow for the laser cooling apparatus to be reduced to a single input beam of cooling light coupled to a diffractive element, providing a compact source of cold-atoms with excellent optical access, and potential for further miniaturisation.

The main laser cooling apparatus that is described in this thesis was used as

the test bed for the atomic clock operation. This apparatus was already established before the work for this thesis began and is briefly described in Chapter 3. The apparatus provided a sample of rubidium atoms, cooled to sub-Doppler temperatures, and was the main workhorse for the CPT-clock experiment.

Based on the success of this experiment, a second apparatus (Sec. 3.4) was built that was intended to provide the same performance, but would also be portable. The system was built onto three breadboards, two of which were loaded into a 19" rack mount for operation outside of the laboratory. In addition, a magnetic shield was designed that could be secured around the vacuum chamber. In the laboratory, we obtained trapped atom numbers that were comparable with the first generation with this experiment. For unknown reasons, the molasses temperature of the cloud seemed to reach a limit at around $100 \mu\text{K}$, which ultimately stopped the experiment moving forward into development as an atomic clock. This limitation has now been overcome using a different laser and cooling optics, but it is not clear what steps contributed to reaching the low molasses temperatures. Research is still ongoing within the experimental quantum optics and photonics (EQOP) group at Strathclyde on the grating-MOTs. However, this grating-MOT system was successfully operated at several public outreach events as a portable cold-atom demonstrator. Following this success, the vacuum chamber from this apparatus, along with its magnetic shielding, was integrated into the first generation clock experiment.

6.1.2 Characterising the Clock

The main line of investigation of this thesis was further characterisation of the first-generation CPT clock experiment. Using the grating-MOT apparatus as a test bed, we focused our attention on developing the short-term stability of the cold-atom CPT experiment as an unlocked atomic clock. The ultracold atoms provided by the grating chips were probed using a Ramsey-like sequence with CPT in a high-contrast $\text{Lin}\perp\text{Lin}$ scheme. The $\text{Lin}\perp\text{Lin}$ CPT fields were realised from one laser that was combined with an electro-optical modulator that was driven at a frequency close to the ground state splitting frequency for ^{87}Rb . This provided the phase-coherence between the two fields required to perform CPT with high contrast.

In Chapter 4, the clock apparatus is described in detail. In the first instance, we focused our attention on the signal-noise ratio of the detected CPT features and Ramsey fringes. The maximum CPT contrast that we observed with the cold rubidium atoms and $\text{Lin}\perp\text{Lin}$ CPT was approximately 70%, using the $F' = 2$ as our common CPT excited state.

In order to significantly reduce probe-induced frequency shifts, the atoms were interrogated using a Ramsey-CPT sequence. A noise-cancellation technique that had two stages was applied to the detected Ramsey-CPT fringes. In the first, we used a reference photodiode that recorded the intensity of the CPT beam and a signal photodiode that detected the signal after the probe had interrogated the atoms. The ratio of the two photodiode signals was taken to cancel some of the common-mode intensity noise. The second pulse in the Ramsey sequence was split into two regions for the second stage of noise-cancellation. The first region contained

the phase information from the Ramsey interrogation, and the second region could be classed as the steady state with no (or very little) phase information. The ratio of the two integrated regions was then applied to provide the final signal. With this technique, the signal-noise ratio of the fringes was increased from $\sim 5 - 10$ to approximately $50 - 60$, when operating with a free evolution time of $T = 10$ ms.

The second line of investigation was measuring the short-term stability of the cold-atom CPT apparatus in an unlocked configuration. This meant that the local oscillator was not stabilised to the atoms during the measurement of the stability. The stability was measured using the Ramsey-CPT fringes with a dark time of 10 ms. With the first generation apparatus, the short-term performance was measured with an Allan deviation of $\sim 2 \times 10^{-11}/\sqrt{\tau}$. The stability seemingly reaches a limit of high 10^{-12} around the mid-term.

6.2 Future Work

In terms of future work, there are a few areas of interest that are open for further investigation. The measured short-term stability of the apparatus is approximately two orders of magnitude above the fundamental stability limit that is set by quantum projection noise. During the characterisation, the observed improvements to the signal-noise ratio and consequently the short-term frequency stability were encouraging. Therefore, pushing towards this limit by investigating other methods of detection, such as using the fluorescence of the atoms, is promising.

At the same time, tackling the measured limit to the mid-term stability is an important goal. Investigating this area would involve more extensive monitoring of

experiment parameters that are sensitive to slow variations in the laboratory environment. This allows us to build up a noise budget and compensate for such drifts. Improving the control over the drifts then grants better confidence of the clock stability at much longer averaging times. Similarly, the signal-noise and stability of the apparatus have reached a point where it is possible to start measuring fundamental shifts from the probe beam, such as Doppler or AC-stark shifts. This is an exciting prospect, and important for understanding the requirements for a compact version of the apparatus.

The long-term goal of the project was the development of a compact microwave clock that was based on cold-atoms. Using the main, larger apparatus as a test-bed to gain a better understanding has already proven to be useful and, as such, it is not unreasonable to imagine a portable system that can be operated outside of the laboratory.

Bibliography

- [1] F. Perosanz, *GNSS: A revolution for precise geopositioning*, Comptes Rendus Physique **20**, 171 (2019).
- [2] P. T. H. Fisk, *Trapped-ion and trapped-atom microwave frequency standards*, Reports on Progress in Physics **60**, 761 (1997).
- [3] H. Lyons, *The Atomic Clock*, Instruments **22**, 133 (1949).
- [4] R. Beehler, *A historical review of atomic frequency standards*, Proceedings of the IEEE **55**, 792 (1967).
- [5] N. F. Ramsey, *A Molecular Beam Resonance Method with Separated Oscillating Fields*, Physical Review **78**, 695 (1950).
- [6] L. Essen and J. V. L. Parry, *An Atomic Standard of Frequency and Time Interval: A Caesium Resonator*, Nature **176**, 280 (1955).
- [7] L. Essen and J. V. L. Parry, *The Caesium Resonator as a Standard of Frequency and Time*, Philosophical Transactions of the Royal Society A: Mathematical, Physical and Engineering Sciences **250**, 45 (1957).

-
- [8] S. Chu, L. Hollberg, J. E. Bjorkholm, A. Cable, and A. Ashkin, *Three-dimensional viscous confinement and cooling of atoms by resonance radiation pressure*, Physical Review Letters **55**, 48 (1985).
- [9] M. A. Kasevich, E. Riis, S. Chu, and R. G. DeVoe, *rf spectroscopy in an atomic fountain*, Physical Review Letters **63**, 612 (1989).
- [10] D. W. Sesko and C. E. Wieman, *Observation of the cesium clock transition in laser-cooled atoms*, Opt. Lett. **14**, 269 (1989).
- [11] J. Lodewyck, *On a definition of the SI second with a set of optical clock transitions*, Metrologia **56**, 055009 (2019).
- [12] G. Panfilo and F. Arias, *The Coordinated Universal Time (UTC)*, Metrologia **56**, 042001 (2019).
- [13] C. Grebing *et al.*, *Realization of a timescale with an accurate optical lattice clock*, Optica **3**, 563 (2016).
- [14] F. Riehle, P. Gill, F. Arias, and L. Robertsson, *The CIPM list of recommended frequency standard values: guidelines and procedures*, Metrologia **55**, 188 (2018).
- [15] J. Yao *et al.*, *Optical-Clock-Based Time Scale*, arXiv:1902.06858 [physics.app-ph] (2019).
- [16] M. Stock, R. Davis, E. de Mirandés, and M. J. T. Milton, *The revision of the SI—the result of three decades of progress in metrology*, Metrologia **56**, 022001 (2019).

-
- [17] S. Knappe *et al.*, *A Microfabricated Atomic Clock*, Applied Physics Letters **85**, 1460 (2004).
- [18] P. Cash *et al.*, *Microsemi Chip Scale Atomic Clock (CSAC) Technical Status, Applications, and Future Plans*, in *2018 European Frequency and Time Forum (EFTF)*, pp. 65–71, 2018.
- [19] Microsemi, *Chip-scale Atomic clock*, 2019.
- [20] D. Miletic *et al.*, *AC Stark-shift in CPT-based Cs miniature atomic clocks*, Applied Physics B **109**, 89 (2012).
- [21] P. Yun *et al.*, *High-Performance Coherent Population Trapping Clock with Polarization Modulation*, Physical Review Applied **7**, 014018 (2017).
- [22] M. Abdel Hafiz *et al.*, *A High-Performance Raman-Ramsey Cs Vapor Cell Atomic Clock*, Journal of Applied Physics **121**, 104903 (2017).
- [23] B. Pelle, B. Desruelle, R. Szmuk, and D. Holleville, *Cold-Atom-Based Commercial Microwave Clock at the 10^{-15} Level*, in *2017 Joint Conference of the European Frequency and Time Forum and IEEE International Frequency Control Symposium (EFTF/IFCS)*, pp. 479–480, 2017.
- [24] R. J. Hendricks *et al.*, *Cs Fountain Clocks for Commercial Realisations - an Improved and Robust Design*, in *IEEE Transactions on Ultrasonics, Ferroelectrics, and Frequency Control*, pp. 1–1, 2018.

-
- [25] F. G. Ascarrunz *et al.*, *A Portable Cold ^{87}Rb Atomic Clock with Frequency Instability at One Day in the 10^{-15} Range*, in *2018 IEEE International Frequency Control Symposium (IFCS)*, pp. 1–3, 2018.
- [26] F. G. Ascarrunz, Y. O. Dudin, M. C. Delgado Aramburo, J. Savory, and S. R. Jefferts, *Long-Term Frequency Instability of a Portable Cold ^{87}Rb Atomic Clock*, in *Proceedings of the 49th Annual Precise Time and Time Interval Systems and Applications Meeting*, pp. 107–110, 2018.
- [27] Spectradynamics, *cRb-Clock*, 2019.
- [28] MuQuans, *MuClock*, 2019.
- [29] X. Liu, E. Ivanov, V. I. Yudin, J. Kitching, and E. A. Donley, *Low-Drift Coherent Population Trapping Clock Based on Laser-Cooled Atoms and High-Coherence Excitation Fields*, *Physical Review Applied* **8**, 054001 (2017).
- [30] J. W. Pollock *et al.*, *AC-Stark Shifts of Dark Resonances Probed with Ramsey Spectroscopy*, *Physical Review A* **98**, 053424 (2018).
- [31] E. Arimondo, *Coherent Population Trapping in Laser Spectroscopy*, volume 35 of *Progress in Optics*, pp. 257 – 354, Elsevier, 1996.
- [32] G. Alzetta, A. Gozzini, L. Moi, and G. Orriols, *An experimental method for the observation of r.f. transitions and laser beat resonances in oriented Na vapour*, *Il Nuovo Cimento B Series 11* **36**, 5 (1976).
- [33] G. Orriols, *Non-absorption resonances by nonlinear coherent effects in a three-level system*, *Il Nuovo Cimento B Series 11* **53**, 1 (1979).

-
- [34] R. Lutwak *et al.*, *The Miniature Atomic Clock - Pre-Production Results*, in *2007 IEEE International Frequency Control Symposium Joint with the 21st European Frequency and Time Forum*, pp. 1327–1333, 2007.
- [35] S. Knappe, *3.18 - MEMS Atomic Clocks*, in *Comprehensive Microsystems*, edited by Y. B. Gianchandani, O. Tabata, and H. Zappe, pp. 571 – 612, Elsevier, Oxford, 2008.
- [36] T. Lindvall, *Alkali-metal Atoms in Laser Fields: Optical Pumping, Coherent Population Trapping and Laser Cooling*, PhD thesis, Aalto University, 2010.
- [37] M. Vangeleyn, *Atom trapping in non-trivial geometries for micro-fabrication applications*, PhD thesis, University of Strathclyde, 2011.
- [38] E. Blanshan, *Development of a Compact Cold-Atom Atomic Clock Based on Coherent Population Trapping*, PhD thesis, University of Colorado, 2014.
- [39] R. Wynands and A. Nagel, *Precision spectroscopy with coherent dark states*, *Applied Physics B: Lasers and Optics* **68**, 1 (1999).
- [40] D. A. Steck, *Alkali D Line Data*, 2015.
- [41] Z. Warren, M. S. Shahriar, R. Tripathi, and G. S. Pati, *Experimental and Theoretical Comparison of Different Optical Excitation Schemes for a Compact Coherent Population Trapping Rb Vapor Clock*, *Metrologia* **54**, 418 (2017).
- [42] J. Vanier, *Atomic Clocks Based on Coherent Population Trapping: A Review*, *Applied Physics B* **81**, 421 (2005).

-
- [43] F.-X. Esnault *et al.*, *Cold-atom Double- Λ Coherent Population Trapping Clock*, Physical Review A **88**, 042120 (2013).
- [44] T. Zanon *et al.*, *High Contrast Ramsey Fringes with Coherent-Population-Trapping Pulses in a Double Lambda Atomic System*, Physical Review Letters **94**, 193002 (2005).
- [45] X. Liu, V. I. Yudin, A. V. Taichenachev, J. Kitching, and E. A. Donley, *High Contrast Dark Resonances in a Cold-Atom Clock Probed with Counter-Propagating Circularly Polarized Beams*, Applied Physics Letters **111** (2017).
- [46] J. D. Elgin *et al.*, *A cold-atom beam clock based on coherent population trapping*, Applied Physics Letters **115**, 033503 (2019).
- [47] A. V. Taichenachev, V. I. Yudin, V. L. Velichansky, and S. A. Zibrov, *On the unique possibility of significantly increasing the contrast of dark resonances on the D_1 line of ^{87}Rb* , Journal of Experimental and Theoretical Physics Letters **82**, 398 (2005).
- [48] K.-I. Watabe *et al.*, *High-contrast dark resonances with linearly polarized light on the D_1 line of alkali atoms with large nuclear spin*, Applied Optics **48**, 1098 (2009).
- [49] S. A. Zibrov *et al.*, *Coherent-population-trapping resonances with linearly polarized light for all-optical miniature atomic clocks*, Physical Review A **81** (2010).

-
- [50] E. E. Mikhailov, T. Horrom, N. Belcher, and I. Novikova, *Performance of a prototype atomic clock based on $\text{lin}\perp\text{lin}$ coherent population trapping resonances in Rb atomic vapor*, Journal of the Optical Society of America B **27**, 417 (2010).
- [51] E. Blanshan, S. M. Rochester, E. A. Donley, and J. Kitching, *Light Shifts in a Pulsed Cold-Atom Coherent-Population-Trapping Clock*, Physical Review A **91**, 041401 (2015).
- [52] X. Liu *et al.*, *Coherent-population-trapping resonances in buffer-gas-filled Cs-vapor cells with push-pull optical pumping*, Phys. Rev. A **87**, 013416 (2013).
- [53] J. P. McGilligan, *Micro-fabricated Diffractive Optics for Quantum Sensors and Atomic Clocks*, PhD thesis, University of Strathclyde, 2017.
- [54] C. Xi, Y. Guo-Qing, W. Jin, and Z. Ming-Sheng, *Coherent Population Trapping-Ramsey Interference in Cold Atoms*, Chinese Physics Letters **27**, 113201 (2010).
- [55] R. Elvin *et al.*, *Raman-Ramsey CPT with a Grating Magneto-Optical Trap*, in *2018 European Frequency and Time Forum (EFTF)*, pp. 61–64, 2018.
- [56] N. F. Ramsey, *Experiments with separated oscillatory fields and hydrogen masers*, Reviews of Modern Physics **62**, 541 (1989).
- [57] C. Foot, *Atomic physics* (Oxford Univ. Press, 2011).
- [58] J. E. Thomas *et al.*, *Observation of Ramsey Fringes Using a Stimulated, Resonance Raman Transition in a Sodium Atomic Beam*, Physical Review Letters **48**, 867 (1982).

-
- [59] P. R. Hemmer, C. C. Leiby, and S. Ezekiel, *Stabilization of a microwave oscillator using a resonance Raman transition in a sodium beam*, Optics Letters **8**, 440 (1983).
- [60] P. R. Hemmer, G. P. Ontai, and S. Ezekiel, *Precision studies of stimulated-resonance Raman interactions in an atomic beam*, Journal of the Optical Society of America B **3**, 219 (1986).
- [61] P. R. Hemmer, M. S. Shahriar, V. D. Natoli, and S. Ezekiel, *Ac Stark shifts in a two-zone Raman interaction*, Journal of the Optical Society of America B **6**, 1519 (1989).
- [62] D. S. Weiss, E. Riis, Y. Shevy, P. J. Ungar, and S. Chu, *Optical molasses and multilevel atoms: experiment*, Journal of the Optical Society of America B **6**, 2072 (1989).
- [63] J. Dalibard and C. Cohen-Tannoudji, *Laser cooling below the Doppler limit by polarization gradients: simple theoretical models*, Journal of the Optical Society of America B **6**, 2023 (1989).
- [64] C. Adams and E. Riis, *Laser cooling and trapping of neutral atoms*, Progress in Quantum Electronics **21**, 1 (1997).
- [65] H. J. Metcalf and P. Van der Straten, *Laser cooling and trapping* (Springer, 2002).
- [66] T. H. Maiman, *Stimulated Optical Radiation in Ruby*, Nature **187**, 493 (1960).

-
- [67] C. N. Cohen-Tannoudji, *Nobel Lecture: Manipulating atoms with photons*, Reviews of Modern Physics **70**, 707 (1998).
- [68] S. Chu, *Nobel Lecture: The manipulation of neutral particles*, Reviews of Modern Physics **70**, 685 (1998).
- [69] W. D. Phillips, *Nobel Lecture: Laser cooling and trapping of neutral atoms*, Reviews of Modern Physics **70**, 721 (1998).
- [70] A. Ashkin, *Acceleration and Trapping of Particles by Radiation Pressure*, Physical Review Letters **24**, 156 (1970).
- [71] T. Hänsch and A. Schawlow, *Cooling of gases by laser radiation*, Optics Communications **13**, 68 (1975).
- [72] D. Wineland and H. Dehmelt, *Proposed 10^{14} $\Delta\nu/\nu$ laser fluorescence spectroscopy on Tl^+ mono-ion oscillator III (side band cooling)*, Bull. Am. Phys. Soc. **20**, 637 (1975).
- [73] A. Ashkin, *Trapping of Atoms by Resonance Radiation Pressure*, Physical Review Letters **40**, 729 (1978).
- [74] D. J. Wineland, R. E. Drullinger, and F. L. Walls, *Radiation-Pressure Cooling of Bound Resonant Absorbers*, Physical Review Letters **40**, 1639 (1978).
- [75] W. D. Phillips and H. Metcalf, *Laser Deceleration of an Atomic Beam*, Physical Review Letters **48**, 596 (1982).

-
- [76] J. Prodan *et al.*, *Stopping Atoms with Laser Light*, Physical Review Letters **54**, 992 (1985).
- [77] E. L. Raab, M. Prentiss, A. Cable, S. Chu, and D. E. Pritchard, *Trapping of Neutral Sodium Atoms with Radiation Pressure*, Physical Review Letters **59**, 2631 (1987).
- [78] P. D. Lett *et al.*, *Observation of Atoms Laser Cooled below the Doppler Limit*, Physical Review Letters **61**, 169 (1988).
- [79] K. I. Lee, J. A. Kim, H. R. Noh, and W. Jhe, *Single-beam atom trap in a pyramidal and conical hollow mirror*, Optics Letters **21**, 1177 (1996).
- [80] M. Vangeleyn, P. F. Griffin, E. Riis, and A. S. Arnold, *Single-laser, one beam, tetrahedral magneto-optical trap*, Optics Express **17**, 13601 (2009).
- [81] M. Vangeleyn, P. F. Griffin, E. Riis, and A. S. Arnold, *Laser cooling with a single laser beam and a planar diffractor*, Optics Letters **35**, 3453 (2010).
- [82] C. C. Nshii *et al.*, *A surface-patterned chip as a strong source of ultracold atoms for quantum technologies*, Nature Nanotechnology **8**, 321 (2013).
- [83] J. P. McGilligan, P. F. Griffin, E. Riis, and A. S. Arnold, *Phase-space properties of magneto-optical traps utilising micro-fabricated gratings*, Optics Express **23**, 8948 (2015).
- [84] J. P. McGilligan, P. F. Griffin, E. Riis, and A. S. Arnold, *Diffraction-grating characterization for cold-atom experiments*, Journal of the Optical Society of America B **33**, 1271 (2016).

-
- [85] E. Imhof *et al.*, *Two-dimensional grating magneto-optical trap*, Phys. Rev. A **96**, 033636 (2017).
- [86] J. P. McGilligan *et al.*, *Grating chips for quantum technologies*, Scientific Reports **7** (2017).
- [87] A. S. Arnold, J. S. Wilson, and M. G. Boshier, *A simple extended-cavity diode laser*, Review of Scientific Instruments **69**, 1236 (1998).
- [88] G. W. Hoth *et al.*, *Impact of Laser Frequency Noise in Coherent Population Trapping with Cold Atoms*, in *2019 Joint Conference of the European Frequency and Time Forum and IEEE International Frequency Control Symposium (EFTF/IFCS)*, 2019.
- [89] R. Elvin *et al.*, *Cold-atom clock based on a diffractive optic*, Opt. Express **27**, 38359 (2019).
- [90] G. W. Hoth *et al.*, *Towards a compact atomic clock based on coherent population trapping and the grating magneto-optical trap*, in *Optical, Opto-Atomic, and Entanglement-Enhanced Precision Metrology*, 2019.
- [91] A. V. Rakholia, H. J. McGuinness, and G. W. Biedermann, *Dual-Axis High-Data-Rate Atom Interferometer via Cold Ensemble Exchange*, Phys. Rev. Applied **2**, 054012 (2014).
- [92] H. J. McGuinness, A. V. Rakholia, and G. W. Biedermann, *High data-rate atom interferometer for measuring acceleration*, Applied Physics Letters **100**, 011106 (2012).

-
- [93] E. A. Donley, F. . Esnault, E. Blanshan, and J. Kitching, *Cancellation of Doppler shifts in a cold-atom CPT clock*, in *2013 Joint European Frequency and Time Forum International Frequency Control Symposium (EFTF/IFC)*, pp. 445–447, 2013.
- [94] R. Boudot, S. Guerandel, E. d. Clercq, N. Dimarcq, and A. Clairon, *Current Status of a Pulsed CPT Cs Cell Clock*, in *2009 IEEE Transactions on Instrumentation and Measurement*, volume 58, pp. 1217–1222, 2009.
- [95] D. Allan, *Time and Frequency (Time-Domain) Characterization, Estimation, and Prediction of Precision Clocks and Oscillators*, in *IEEE Transactions on Ultrasonics, Ferroelectrics and Frequency Control*, volume 34, pp. 647–654, 1987.
- [96] D. W. Allan, N. Ashby, and C. C. Hodge, *The science of timekeeping* (Hewlett-Packard, 1997).